Three-dimensional Flow-induced Dynamics of the Endothelial Surface Glycocalyx Layer

by

Yu Yao

M.S. Mechanical Engineering (2005)

Massachusetts Institute of Technology

Submitted to the Department of Mechanical Engineering in Fulfillment of the Requirements for the Degree of PhD in Mechanical Engineering at the Massachusetts Institute of Technology

[September 2007]
August 2007

Signature of Author _____
Department of Mechanical Engineering
August 22, 2007

Certified by _____
C. Forbes Dewey, Jr.
Professor of Mechanical Engineering
Thesis Supervisor

Accepted by _____
Lallit Anand
Chairman, Department Committee on Graduate Students

Three-dimensional Flow-induced Dynamics of the Endothelial Surface Glycocalyx Layer

by
Yu Yao

Submitted to the Department of Mechanical Engineering
on August 22, 2007 in fulfillment of the
requirements for the Degree of PhD in
Mechanical Engineering

Abstract

Endothelial cells play a central role in maintaining vascular integrity. Lesions in the endothelial layer may allow the invasion of leukocytes into the artery wall and promote inflammatory responses that could possibly lead to atherosclerosis. Over the past decade, a series of studies have demonstrated the presence of a delicate surface layer, named the glycocalyx, decorating the endothelial membrane and associated with a number of physiological implications in the vasculature. This thesis studies the flow-induced dynamics of the endothelial glycocalyx layer and reports the first direct measurement of the *in vitro* mechanical properties as well as the thickness of the glycocalyx through a novel optical imaging approach.

Here, we have developed an optical imaging system that tracks the position of single particles in three-dimensional (3D) space with high precision, typically 1 ~ 4 nm in the XY plane and 15 ~ 40nm in the Z-direction along the optical axis of the microscope. With the use of quantum dots (QDs), semiconducting nanoparticles of superior optical characteristics, this method provides the opportunity to investigate biological subjects in living cells that can be neither spatially resolved nor continuously traced over minutes by conventional optical microscopy techniques. Therefore, by 3D mapping of both the glycocalyx layer and the membrane using quantum dots of different colors, the *in vitro* thickness of the endothelial glycocalyx layer is found to be ~ 350nm.

With QDs attached to the glycocalyx layer, we track the flow-induced motion of this thin structure at multiple levels of oscillating shear stresses from 5 to 20 dynes/cm^2. The displacement of each QD ranges from 80 ~ 400 nm and varies from cell to cell and point to point on a single cell. The estimated Young's modulus is thus ~6.7Pa, for a 3D matrix with a measured thickness of ~ 350nm. The QD motion, staying in phase with the applied shear stress up to the 1Hz limit of the present study, confirms the highly elastic gel nature for the glycocalyx layer in which major deformations occur at physiological level of fluid shear stress.

Thesis supervisor: C. Forbes Dewey, Jr.
Title: Professor of Mechanical and Biological Engineering

Acknowledgements

I sincerely thank Prof. C. Forbes Dewey, the best advisor and teacher I could ever wish for. Without his wisdom, support, enthusiasm and inspiration, I would have never made even a small step of progress in my thesis. It has been a great journey to work with him all these years, where I learned so much about science and life. And most importantly, I am grateful to an invaluable friendship that will continue for the rest of my life.

I wish to thank my committee members, Prof. Roger Kamm, Prof. Peter So, and Prof. Ram Sasisekharan, for providing continuous guidance and sharing with me their insightful knowledge throughout the course of the project.

I am extremely fortunate to have worked with two best collaborators I could ever imagine, Maxine Jonas and Hao Huang. This thesis could not have been completed without their numerous efforts devoted into the collaboration. I am thankful to Alex Rabodzy, who prepared me for the first *in vitro* experiments in my life, and David Berry, Eric Osborn, Maryelise Cieslewicz and many people who have helped me through the completion of this thesis.

My special thanks to Donna Wilker, Leslie Regan, and my collegues in the Hatsopolous Microfluids Lab who have made all these years such an enjoyable experience.

I am forever indebted to my parents for their love, understanding and endless patience and encouragement ever since they gave birth to a little baby girl, 26 years ago.

Finally, I thank my husband, Jian, for the love and support that have been around me all along. Always a true believer in me, enduring my late hours, my spoiled weekends, my bad temper, and even my computer bugs. To him, I dedicate this thesis.

Table of Contents

Chapter 1. The Endothelial Glycocalyx

1.1. The Endothelium

The luminal surface of human arteries is lined with a continuous layer of vascular endothelium, which in fact, plays a central role in maintaining vascular integrity. Lesions in endothelial layer may allow the invasion of leukocytes into subendothelial space and promote inflammatory responses that could possibly lead to atherosclerosis. Endothelial cells, as a unique cell type in human body, are constantly situated in a hemodynamic environment and experiencing mechanical forces exerted by the blood flow. As our understanding of vascular disease formation in large part relies on the knowledge of fundamentals of endothelial function, known to be influenced by the local mechanical environment, we have chosen endothelial cells as the subject of our study will utilize several engineering methods available to probe the biomechanical properties of the endothelial cells. This chapter serves as a background introduction to our study.

1.1.1. Atherosclerosis and Endothelial Cells

Despite the advances in medical diagnostic technologies and the use of new pharmaceutical approaches, cardiovascular disease continued to be the leading cause of death in the United States and Europe(19, 20). Atherosclerosis, as one major disease in the category, is a chronic inflammatory disease in the artery wall, in large part due to the deposition of lipids(118). Numerous pathophyiologic obersvations have led to the well-accepted hypothesis that the early stage of atherosclerosis started out in endothelial dysfunction. Princple risk factors of endothelial dysfunctions may include high-level of

cholesterol intake, cigarette smoking, hypertension, genetic alteration as well as bacterial infections(122).

In a number of review articles by Ross (118-122), the "response-to-injurey" hypothesis of the pathogenisis of atherosclerosis is summarized in the following stages as shown in Fig 1-1. Initially, different forms of injury in the endothelial monolayer increase its adhesiveness with respect to leukocytes and/or platelets. As the leukocytes migrate into the artery wall, enhanced endothelial permeability to lipoproteins and other plasma proteins occurs. If the inflammatory response fails to neutralize the offending agents and continues along, the production of procoagulant substances by the endothelium will stimulate the migration and proliferation of smooth-muscle cells that soon merge into the area of inflammation to form an intermediate lesion. Subsequently, increased number of macrophages and lymphocytes enter from the blood and multiply within the lesion that eventually lead to the formation of necrotic core region underneath the artery wall, recruiting a mixture of leukocytes, lipids, debris and fibrous tissues. When the inflammatory site progresses to a point where the thin cover can no longer bear the continuing influx and activation of macrophages, the fibrous cap of the region ruptures and can rapidly lead to thrombosis and occlusion of the artery. When this happens in the heart, it could be a heart attack; and when it happens in the brain, it could result in a stroke.

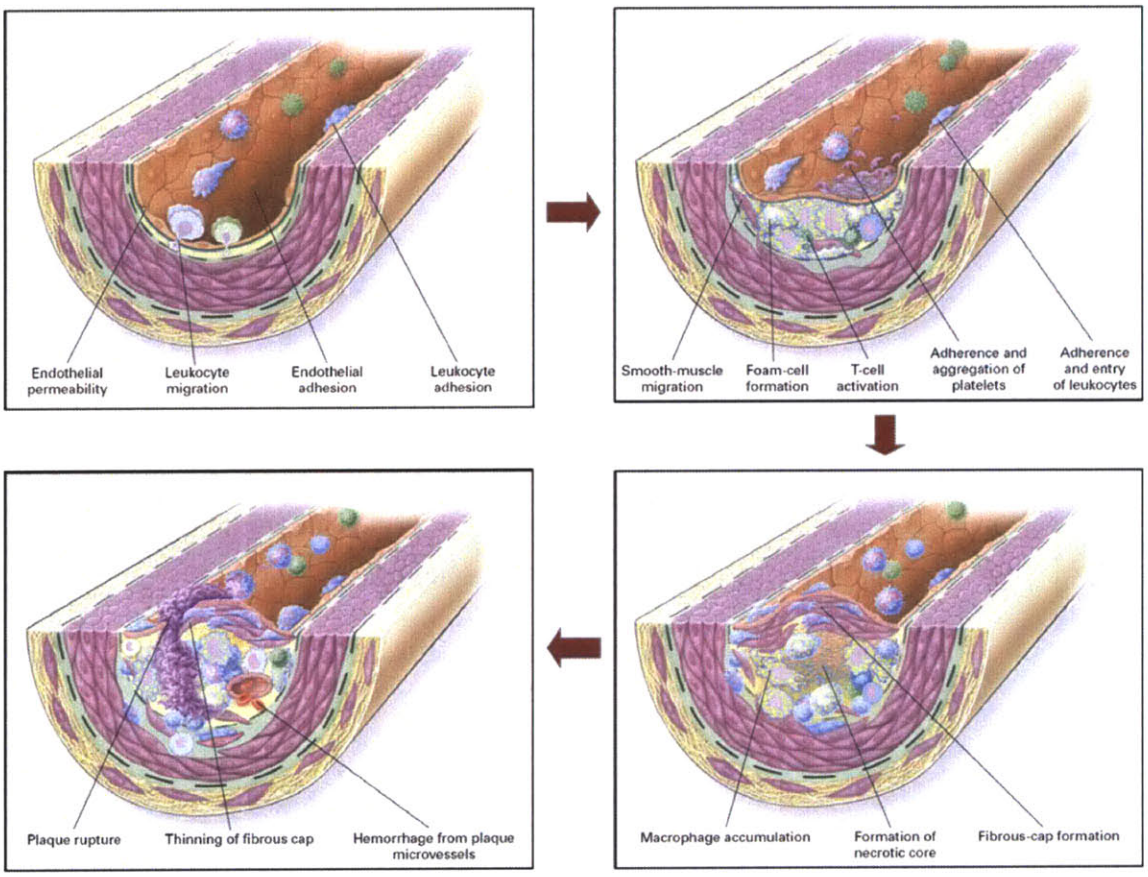

Figure 1-1 Pathological progression of atherosclerosis as described in Ross (119). Endothelial dysfunction in the early stage may lead to severe inflammatory response that result in lipid deposition and macrophage accumulation in the lesion sites and eventually result in thrombosis and occlusion of the artery. Figure reproduced from Ross (119).

As endothelial dysfunction appears to be the first step in this chain reaction, enormous amount of effort and energy has be spent over the years in the area of studying endothelial function in a physiological context. The endothelial cells act not only as a liner for the blood vessels, but they also respond to various stimuli originating from the blood and thus actively participate in the physiological adaptation or phythogenisis of a give region of the vasculature(60). These fuctional roles include(120):

1. provision of a nonadherent surface layer for leukocytes and platelets in the plasma;
2. regulation of the exchange of fluid and nutrients between the plasma and the artery wall;
3. secretion of a series of groth-regulatory moelues, vasodilatory molecules and vasoconstrictive molecules;
4. provision of anticoagulant and procoagulant activities;
5. mainteinance of connective tissue matrix that the basal membrane lies upon; and
6. modification of substance from the plasma such as oxidizing lipoproteins during transportation into the vascular wall.

Alterations in one or more of these functions can result in the early phases of atherosclerosis.

1.1.2. Hemodynamic Impact on Endothelial Functions

Vascular endothelium is constantly exposed to a spectrum of hemodynamic forces generated by the blood flow, including hydrostatic pressures, cyclic strains and wall shear

stresses. There exists an immense body of evidence suggesting these mechanical stimuli can directly influence endothelial structure and function, both acutely and chronically. Atherosclerotic lesions in endothelium preferably develop in certain specific arterial sites, such as branches, bifurcations and curvatures, where decreased shear stress and increased turbulence are found (24). In those regions, endothelium produces specific molecules that are responsible for the adherence, migration and accumulation of monocytes and T cells (120). The nature of the flow --- whether it is laminar, disturbed, or turbulent --- appears to be the determinant factor of which arterial sites are prone to have lesions (34, 61, 63). Therefore, the area of studying flow-induced endothelial response has be a center arena during the past 40 years with a goal to better understand the mechanism behind those effects.

One prominent indicator of endothelial dysfunction in vivo is the disruption of cell shape. Atheroprotective regions are characterized by ellipsoidal cell shapes and coaxial alignment in the flow direction; while a more random and polygonal cell pattern is observed in the disturbed flow region (98). Since these morphology characteristics were first reproduced *in vitro* in the early 80s by subjecting cultured endothelial cells to controlled fluid shear stress with the use of a cone-plate flow system (49), a number of discoveries in the field have provided strong link between mechanical stimulus and biological response in endothelial cells.

Endothelial cell respond to fluid flow through a complex process that involves multiple signaling pathways and leads to various morphological, mechanical and biochemical

events. One commonly studied phenomenon is the upsurge of calcium ion concentration upon flow onset (134). Calcium elevation may either result from influx through calcium ion channels or from the release of intracellular storages, and the latter can be initiated by G protein activation (84). As a series of second and third messengers proprogate down the signaling pathways, cytoskeletal reorganization and structure changes start to occur by both calcium-dependent and calcium independent process (88, 145). The endothelial monolayer becomes smoother in the first hour of flow, and microvilli present on the apical surface under static conditions disappear, leaving a smooth and glassy contour (125). Basally-located dense peripheral bundles of F-actn stress fibers dissolve shortly after shear stress exposure, and reform hours later under the apical membrane, aligned with the long axis of the cells (12, 124). Despite the observed motility drop of endothelial cells by 40% during the initial hours of flow, actin filament turnover rate increases and meanwhile the amount of polymerized actin decreases, suggesting accelerated actin filament remodeling events in individual cells in a confluent endothelial monolayer (102).

In vitro studies have demonstrated that the application of physiological levels of laminar shear stress can regulate the expression of a variety of physiologically relevant genes, including growth factors, fibrinolytic factors, and adhesion molecules (42, 60, 115). In the studies on the transcriptional regulation of certain shear-sensitive genes, interestingly, people have identified some positive and negative "shear-response elements" in the promoter region(4, 60, 75, 116, 135). In 1999, an RT-PCR based approach was adopted to map systematically the differential patterns of endothelial gene regulation by

biomechanical stimuli(60), which may provide further insights to explain the link between heomodynamic environment and pathological and physiological signaling events. As the flow nature clearly correlates with the atherogenic risks of vascular sites, the effect of turbulence on cell function has also been studied in *in vitro* systems. Early research has demonstrated that the response of endothelial cells to turbulent flow differs significantly from response to laminar shear stress (44, 46). Turbulence stimulated substantial endothelial DNA synthesis in the absence of cell alignment, discernible cell retraction, or cell loss(45). Sustained calcium response was observed in endothelial patch under turbulent flow, whereas steady shear typically produces single pulse of calcium peak. The differences in shear-induced response may be due to the temporal variation in the mechanical stimulus or the turbulence-generated high shear gradients at cell-cell attachment sites (47).

Despite the evident impact of hemodynamic force exerted on endothelial cells, the detailed mechanism still remains unclear. In various theoretic models to describe the mechanism of mechanotransduction, the transformation of mechanical clues to biochemical signals, endothelial cell mechanosensors previously proposed include integrins, G proteins, intercellular junction proteins, and ion channels (54). Recent investigation of the glycocalyx has lead us into a new perspective that this "bush-like" structure (162) on the apical membrane may play an important role in mechanotransduction (41, 55, 64, 131, 146, 147, 149, 157). One of my research projects, as summarized in Chapter 2, is therefore to study the role of the glycocalyx in flow-reduced endothelial response.

1.2. The Glycocalyx

The glycoclayx is a complex surface layer of various transmembrane macromolecules and glycosaminoglycans chains located on the apical membrane of endothelial cells. The *in vivo* evidence of glycoclayx (29, 30, 38, 85), particularly the intravital microscopic observations in the mid 90's (157), has presented the discovery of an extensive layer on the endothelial surface and stimulated a number of theories about its composition and properties (39, 41, 72, 143, 149, 162, 168). The following paragraphs will provide a brief summary of glycocalyx related studies up to date.

1.2.1.Observation of the Glycocalyx

At the time the glycocalyx was first observed by electron microscopy more than 50 years ago(26), it was characterized as a thin layer of molecules with a thickness of only about 20 nm. However, this did not present the full scope of the structure as the preparation procedure and possibly the dye itself may have caused substantial and irreversible damages to the fragile glycocalyx structure with high water content. Subsequent improvement in the staining technique in electron microscopy revealed a much thicker endothelial surface layer, on the order of 100nm (30, 85). Recent studies by van den Berg *et al* (154) adopted a new dye, Alcian blue 8GX, to stabilize the anionic carbonhydrate structures in rat myocardial capillaries, and thus revealed a dense carbonhydrate layer of 0.2- to 0.5-μm thick covering the endothelium. Hyaluronidase enzyme degradation confirmed a high hyaluronic content of the stained glycocalyx structure.

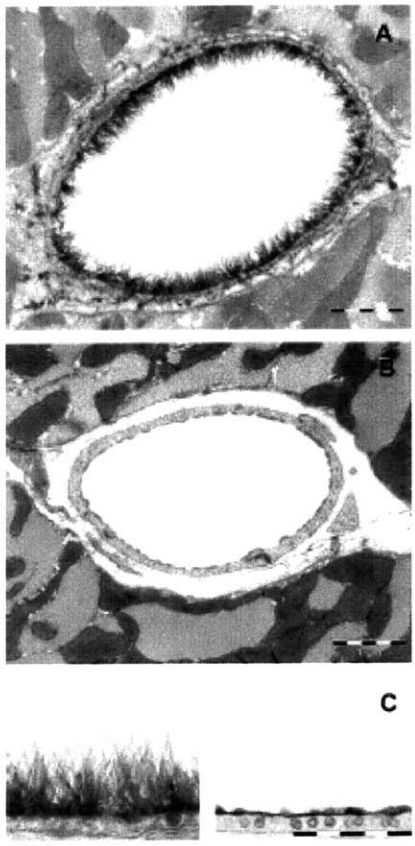

Figure 1-2 Electron microscopy of an Alcian blue 8GX–stained rat left ventricular myocardial capillary (A) showing a glycocalyx layer with a thickness of about 0.5μm covering endothelium in comparison with a smooth endothelium after enzyme degradation (B). Bars in (A) and (B) = 0.5 μm. A detailed view of the dense glycolcayx layer before (left) and after (right) enzyme treatment is illustrated in (C). Bar = 1 μm. Figure excerpted from van den Berg *et al* (154)

In parallel with electron microscopy approaches, quantitative intravital studies of the microcirculation since the late 1970s have also indicated the existence of a glycoalyx layer as an interface between luman and vascular wall. When studying red cell volume fraction (tube haematocrit) in capillaries of hamster cremaster muscle, Klitzman et al. (77) obtained unexpected low values of tube haematocrit compared with theortical prediction from a glass tube model. This discrepancy however, could be explained by assuming "a slow-moving plasma layer on the order of 1 μm thick" responsible for excluding red blood cell from the layer (77). Subsequet studies by Pries et al (110, 111) also reported that the dependence of flow resistance on vessel diameter measured in capillaried did not agree with glass tube observations. The inconsistency again, led to a hypothesized stationary plama layer on the endothelial surface, with a thickness of about 1.1 μm.

For direct visualization of the layer using intravital microscopy, Vink and Duling(157) adopted an alternative approach to label the flowing plasma instead of staining glycocalyx layer and thus measured plasma exclusion in the blood vessel. When compared to the anatomical diameter of the capillary, the fluorescent plasma volume was constantly smaller due to dye exclusion by the endothelial surface layer. In addition, as white blood cells fully occupied the anatomic capillary cross section, red blood cells were continually excluded from the near wall region and occupied a significantly smaller volum in the blood vessel (~1.2 μm lesser in diameter). This study provided the first visual demonstration of a countinous glycoalyx layer with a thickness about 0.4 to 0.5 μm decorating on the endothelial surface.

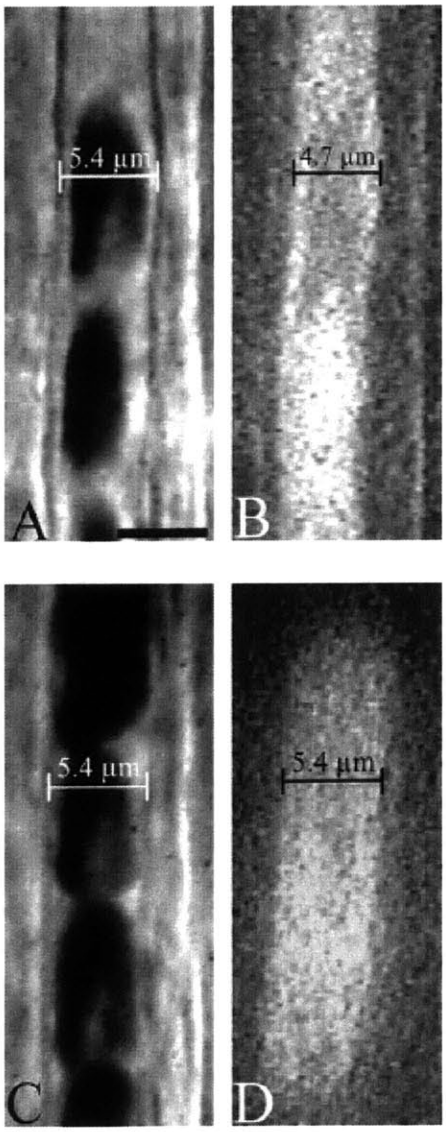

Figure 1-3 Intravital microscopic images before (A and B) and after (C and D) five minutes of continous epi-illumination. Before epi-illumination treatment, red blood cell width (A) and FITC-dextran (B) occupied volume were significantly smaller than the anatomic diameter of the capillary. After the treatment to degrade glycocalyx layer, red blood cell (C) and FITC-dextran (D) both fully occupied the capillary lumen. Bar in (A) = 5 μm. The results suggested an endothelial surface layer with a thickness of about 0.4 ~ 0.5 μm existing on the luman side of the endothelium and excluding macromolecules from entering into the endothelium. Source: Vink *et al.* (157)

1.2.2. Composition of the Glycocalyx

The endothelial surface is covered by an extracellular domain containing a variety of membrane-bound molecules, including proteins, glycolipids, glycoproteins, and proteoglycans, many of which involve charged groups (109). Contantly in a dynamic equilibrium with the flowing plasma, the composition and the physical properties of the layer, as well as the effective thickness, are possibly influenced by the adsorption of plasma proteins. The hypothetical model proposed by Pries *et al.*(109) (Fig 1-4) gives a description of the layer structure and composition. A relatively thin (50~100 nm) region near the endothelial surface is dominated by membrane-bound macromolecules, including glycoproteins and proteoglycans. On top of the directly membrane-associated layer is a much thicker (~500 nm) three-dimensional matrix of soluble plasma components possibly consisting of a variety of glycosaminoglycans and plasma proteins. The entire layer, named the endothelial surface layer, is in a dynamic equilibrium with the flowing blood. Therefore, the effective thickness and composition of the layer is dependent of the local plasma condition as well as haemodynamic environment.

One major group of proteins of particular interest to us is the syndecan family proteoglycans. Illustrated in Fig 1-5, along the protein backbone, proteoglycans are usually modified by long glycosaminoglycan side chains, the length of which is typically on the order of 80nm (approximately 200 sugar residues). Among various core proteins, syndecan-1 and syndecan-4 are especially important because their cytoplasmic tails are known to interact with F-actin, thus providing a possible signaling pathway that can transduce the mechanical signal to the intracellular cytoskeleton (14).

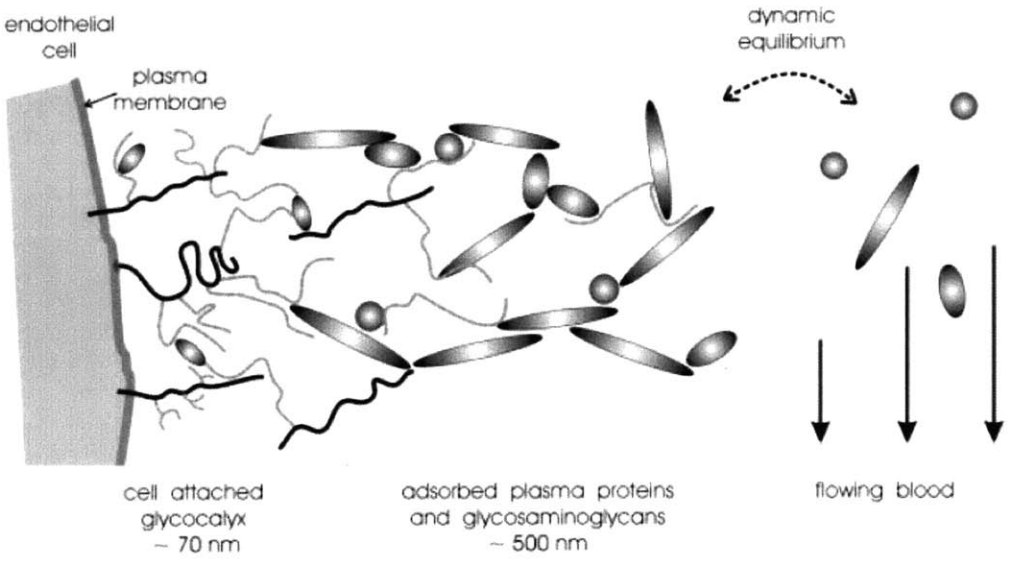

Figure 1-4 Hypothetical composition of glycocalyx proposed by Pries *et al.*(109) A half-micron thick layer of glycosaminoglycans and associated plasma proteins interacts with membrane-bound macromolecules, which together construct the integral endothelial surface layer.

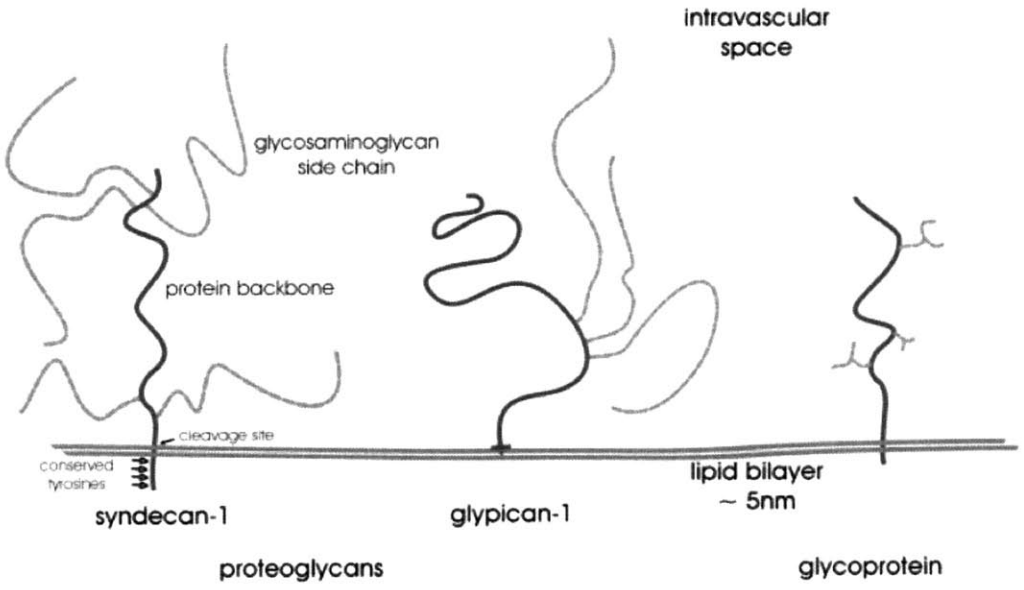

Figure 1-5 Representative proteoglycans and glycoproteins associated with the endothelial membrane. Core proteins of proteoglycans, including syndecan-1, provide several attachment sites for glycosaminoglycans along its protein backbone. (109, 161)

Syndecan-4, for instance, acts as an organizing center for transmembrane receptors and its cytoplasmic tail links to actin cytoskeleton through several signaling molecules (Fig 1-6). Among various glycosaminoglycans modifying the syndecans, heparan sulfate GAGs and chondroitin sulfate GAGs are the two dominant GAG groups on endothelial cells(51). Therefore, we choose heparan sulfate GAGs as our primary targets in the glycocalyx matrix to probe various aspect of glycocalyx properties.

In a modified sketch of the structural model previously proposed by Squire *et al.* (142), Weinbaum and his collegues presented the "bush-like" glycocalyx structure in the context of an integral endothelial cell (Fig 1-7). Through the core protein anchors across the membrane, the 150 ~ 400nm thick matrix connects to the intracellular cytoskeletal structure. Transcellular stress fibers further pass down the link to the focal adhesion proteins (e.g. integrins) on the basal membrane, as well as proteins in the junctional complexes. The 20nm periodic spacing between molecues in the glycocalyx matrix was based on earlier electron microscopic observation in the capillary(142) .

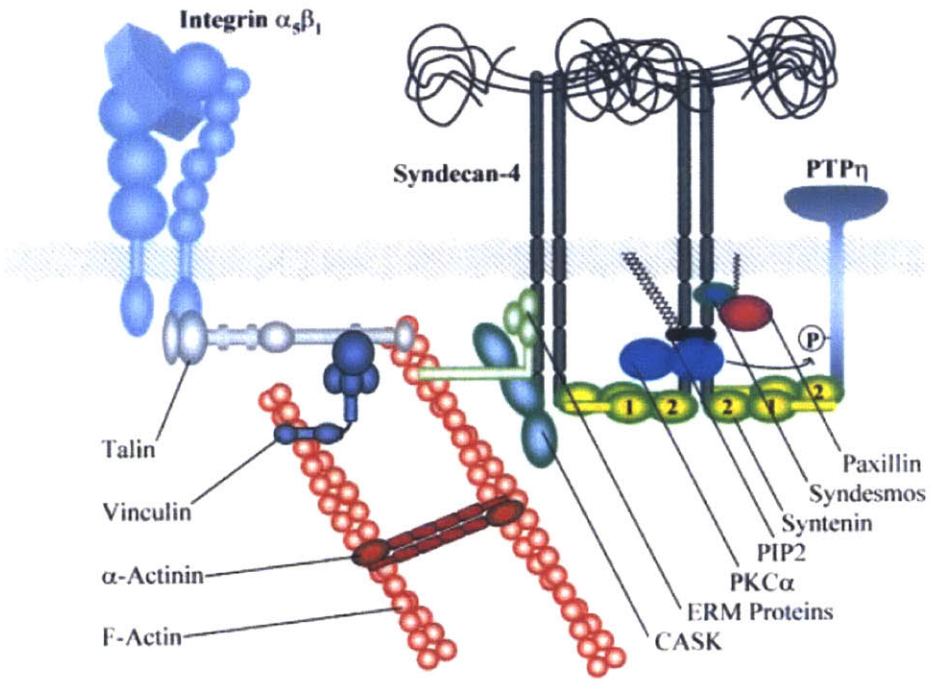

Figure 1-6 Cartoon by Bass *et al.* (14) illustrating sydecan-4 as an organizing center for transmembrane receptors and connecting to actin cytoskeleton.

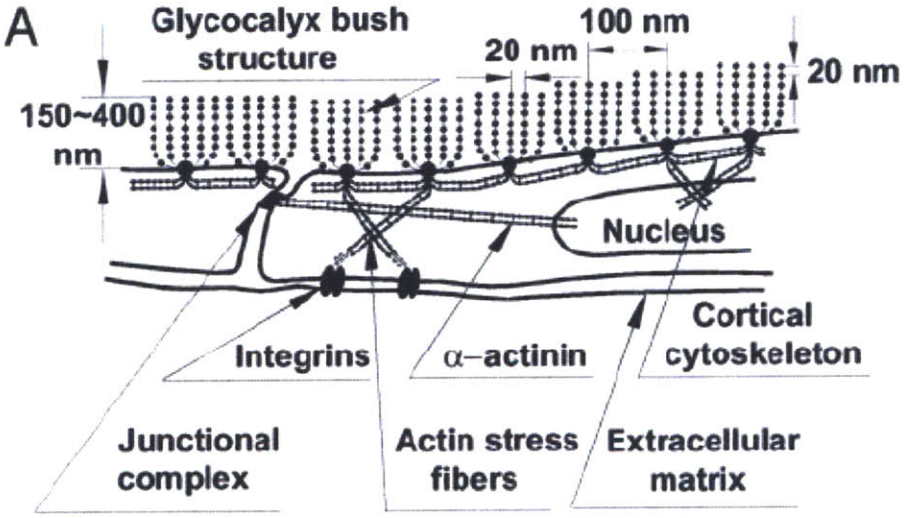

Figure 1-7 Theoretic sketch of the glycocalyx matrix interacting with the rest part of endothelium, by Weinbaum *et al.*(162)Physical Implications of the Glycocalyx

1.2.3. Mechanical and Electrochemical Properties of the Glycocalyx

1.2.3.1. Elastic properties of the glycoclayx

So far, there are no direct elasticity measurements to the core structure of the glycocalyx (e.g. proteoglycans) similar to those performed on other cellular components, such as actin filaments and microtubules (62, 76). The sub-micron dimension and the fragile polysaccharide nature of the glycocalyx layer have created great challenges for the application of conventional mechanical probing techniques. Weinbaum et al (162) instead, developed an indirect approach to estimate the flexural rigidity, *EI*, of the layer based on the experimental observation of the time-dependent restoration of the glyclcayx after the passage of a white blood cell, as previous reported by Vink *et al*(158).

The model by Weinbaum et al (162) treats the core proteins as elastic fibers and uses small deflection theory to predict the long-time final decay of the fiber's elastic recoil (161). This lineraized model therefore predicts the *EI* of the glycocalyx to be 700 $pN{\cdot}nm^2$, about 1/20 of the measured value of an F-actin filament (53). Furethemore, it suggests that the tip delfection of a single fiber under a fluid sh(156)ear stress of 10 dynes/cm2 at the edge of the glycocalyx layer is only 17.9nm (162). More recently, Han et *al.*(67) developed a more sophisticated large deformation model for elastica that predicts the *EI* is 490 $pN{\cdot}nm^2$.

1.2.3.2. Electrochemical properties of the glycocalyx

Since the glycocalyx is known to be composed of highly negative-charged GAGs, the electrochemical environment can greatly influence the molecular transport of cationic and anionic constituents in the plasma across the layer. Vink *et al*(156) reported that the endothelial suface layer selectively allows permeation of neutral or anionic tracers of small sizes (0.4~40 kDa) at different rates while prohibiting the entrance of either neutral or anionic tracers >= 70 kDa. Motivated by this experimental observation, Stace *et al*.(143) developed an electrochemical model to study the transport of charged molecules through this glycocalyx matrix with fixed negative charges.

Under the assumption of global charge neutrality, the interaction of the fixed negative charges with cations and anions in the blood leads to local charge gradients that form a double layer at the glycocalyx-plasma interface. The model(143) shows that anionic plasma tracers would be partially exluded by the glycocalyx layer in equilibrium, and the degree of this exclusion would be a function of the tracer valuence, glycocalyx fixed-charge density as well as the ionic strength of the flowing plasma. In comparison with experimental data by Vink *et al*(156), the fixed-charge density of the glycocalyx is estimated to be 0.7 ~ 1.3 mEq/l, which is about 1% of the ionic concentration of the plasma (143). This model was later extended to investigate the effect of the glycocalyx charge density on mechanical recovery of the layer after compression by a passing leukocyte in a capillary(41).

1.2.4.Theoretic Models of the Glycocalyx

1.2.4.1. Hemodynamic model for flow in the glycocalyx

Several recent studies focusing on the role of the glycoclayx in mechanotransduction, in WBC rolling and RBC passaging in capillary all adopted the assumption that the fluid shear stress at the edge of the glycocalyx is greatly reduced as it propagates through the fiber matrix and the resulting shear stress at the endothelial membrane is effectively zero (67, 149, 162, 168).

The hemodynamic model for the flow in the glycocalyx begins with applying the Brinkman equation to a poroelastic layer with small solid volume fraction, stated as

$$\begin{aligned} -\mu\nabla\times\nabla\times v \; - Kv \; &= \nabla p \\ \nabla\cdot v \; &= 0, \end{aligned}$$

where v is the fluid velocity in the layer, p is the pressure field, μ is the fluid dynamic viscosity and K is the hydraulic resitivity(40). The viscous drag can be characterized by a dimensionless variable $\delta^2 = \mu/(h^2K)$, where h is the effective thickness of the layer. δ^2 represents the ratio of the viscous drag forces caused by fluid-velocity gradients in the glycocalyx layer to the permeation-induced viscous drage due to the fluid motion relative to the solid constitute of the matrix. Estimates of K ~ 10^{10}-10^{11}dyn·s/cm^4(41, 162), μ ~0.01 dyn·s/cm^4 (equal to blood plasma)(161) and h ~0.5μm give rise to δ^2, in the range of 10^{-4}~10^{-3}. Therefore, for such small values of δ^2 (<<1), a Darcy flow dominates away from outer edge of the glycocalyx layer, and the fluid shear stress on the membrane is attenuated to almost zero.

1.2.4.2. Models for restoring mechanism

Among limited experimental data on the mechanical properties of the glycocalyx layer, one pioneer study by Vink *et al* (67, 158)shows that the glycoclayx *in vivo* can be crushed to as much as 20% of its undeformed thickness by the passage of a leukocyte through a capillary, and the layer gradually recovers with a time constant of ~0.4s. Therefore, three models have been developed to explain the restoration mechanism behind this experimental observation and they are summarized in a recent review by Weinbaum *et al* (161).

a. Oncotic model

Pries and Secomb (112, 132) developed an oncotic model that states even a small difference between the protein concentration in the glycocalyx and the plasma concentration in blood would be capable of generating sufficient osmotic pressure to exclude red blood cells from the glycoclayx layer under physiological flow conditions in capillaries. The source of the restoration force of a compressed glycocalyx layer, anayzed by this model, is chemical in nature instead of mechanical.

This model suggests that when in equilibrium, the excessive oncotic pressure within the layer would be balanced by tension in the layer. Compression of the layer by mechanical load (e.g. during red blood cell passaging) would result in a further enhanced pressure difference and a reduced tension that together could balance the external force. During the recovery phase once the load is lifted, tension within the layer would then be reestablished to restore the condition in equilibrium. Their analysis shows that an oncotic

pressure of only 20 dynes/cm^2 in equilibrium could be large enough to exlude red blood cell from the glycocalyx layer (132, 161).

b. Elastohydrodynamic model

Elastohydrodynamic model, first introduced by Weinbaum *et al.* (162), considers the core protein fibers having a finite flexural rigidity, *EI*, that could withstand fluid shear stress exerted at the outer edge of the fibers in the physiological range. Based on the observation of the glycocalyx compression by the passage of a WBC(158), this model predicts the flexural rigidity of the layer, *EI*, to be 700 pN·nm^2.

Later, Han *et al.* (67) developed a more sophisticated nonlinear elastohydronyncamic model that predicted a two-phase recovering mechanism to explain the time-dependent restoration of the glycocalyx after the passage of the WBC. As shown in Fig 1-8(a), during intitial phase for large compression, the glycocalyx is less than 36% of its uncompressed thickness, and the ends of fibers appear parallel to the endothelial membrane. Once entering phase two, the fibers recover bending similarly to the shape of elastic bars. According to their analysis, shown in Fig 1-8(b), the model shows a good agreement with experimental data regarding the transients of glycocalyx recovery.

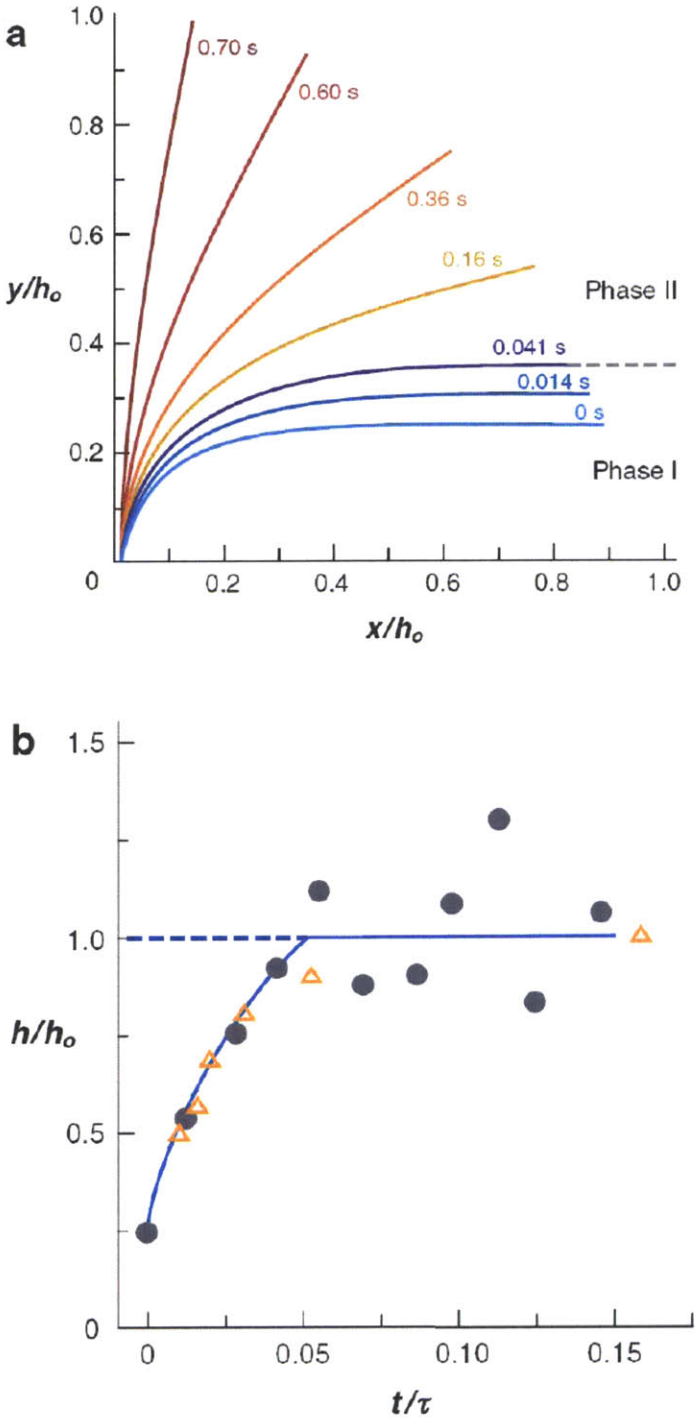

Figure 1-8 (a) Time-dependent glycocalyx layer restoration after compression by a WBC experiencing two phase transition, predicted by Han et al.(67). (b) Comparison of model prediction by Han (*solid line*) and prediction by Damiano & Stace (41)(*open triangle*), with experimental results (67, 158), describing time constants of glycocalyx recovery (161).

c. Mechano-electrochemical model

In this model, Damiano & Stace described that the structural integrity and restoration mechanism of the glycocalyx originate from its electrochemical nature of higly-charged macromolecules in a mixture hydrated in an electrolytic fluid (41). In the absence of axial flow in the vessel, they considered one-dimensional finite deformation of the layer, modeled as an isotropic quaternary mixture. Based on the assumption that the volume fractions of the solid and ionic constituents and the viscosity of the fluid constituents are all negligible, they applied the constitutive law using Nernst-Planck equation to describe the solid and ionic flux. Consequently, the model predicts that the glycocalyx recovers after deformation as a result of a combination of electrostatic and chemical potential gradients. The interaction of the fixed-bound charges in the matrix with the free ions in the solution generates the electrostatic potential gradient across the matrix, whereas a higher concentration of bound GAGs, glycoproteins, and proteoglycans compared to the corresponding consitituents in the blood is the main reason of the chemical potential gradient. Their prediction of the recovery process (also shown in Fig 1-8(a)), compared with observation of ~1s recovery time (158), gives rise to an estimated fixed-charge density of the glycocalyx layer of ~1mEq/l (41).

1.2.5.Physiological Implication of the Glycocalyx

As an interface between the vascular endothelium and the flow plasma, the glycocalyx layer is likely to have a strong influence on many physiological processes in the vascular system. Below is a summay of several aspects where the glycocalyx may play a critical role, based on several excellent review papers recently (109, 146, 147, 161) .

1.2.5.1 Shear stress effect on endothelial cells

As previously suggested, the fluid shear stress acting on the endothelial membrane is vanishingly small due to the presence of the glycocalyx layer(147, 149, 162). Therefore, endothelial membrane or membrane-bound proteins alone is not sufficient to transform the mechanical stimuli into intracellular biochemical responses. The glycocalyx instead, as an interface between the blood flow and the endothelial cells, provides a structure that could sense the fluid shear stress exerted by the extracellular flow and transmits it to the intracellular structure. Recently, there is a growing body of interest in studying the role of glycocalyx in mechanotransduction.

One common approach adopted by various study groups is to examine whether partial degradation of the layer would affect endothelial characteristic responses to flow. For instance, Florian et al (55) reported that removal of heparan sulfate GAGs can completely stop nitric oxide (NO) production in cultured endothelial cells in response to shear. Mochizuki et al(93) also reported that removal of hyaluronic acid GAGs can inhibit 80% of NO production in response to shear. In addition, Ainslie et al (1) have shown that removal of chondroitin sulfate GAGs in the glycocalyx greatly affects the contraction

response to increase in shear in smooth muscle cells. Combined together, these evidence lead to the idea that maintaining the stability of the integral structure of the glycocalyx is important in mechanotransduction (147). Studies by Thi *et al.* further reported that the disruption of the glycocalyx can affect the actin cytoskeleton reorganization and focal adhesion localization after cells were exposed to 5 hr of laminar shear, and proposed a bumper-car model for the role of the glycocalyx (149). Meanwhile, Moon *et al.* examined the role of cell surface heparan sulfate proteoglycans in endothelial cell migration and proposed that heparan sulfate proteoglycans may be involved in sensing the direction of the flow (95).

1.2.5.2. Barrier function

Extracellular membrane-bound macromolecules have long been considered as critically involved in the selective transport of materials across the endothelium. Fluorescent intravital microscopy studies have shown that albumin has access to the endothelial surface while dextran molecule (~ 70 kDa) has not (65, 69). The half time for permeation of neutral tracers (molecular weight from 0.4 to 40 kDa) into the glycocalyx layer is typically about 1min, whereas the permeation of anionic tracers of molecular weight in the same range is significantly slowered, with half-times between 11 and 60 min (69). Cleavage of the hyaluronan components in the layer results in an enhanced access of dextran into the layer, which suggests that hyaluronan plays an important role in determining the macromolecular permeability of the glycocalyx (69). In addition to those experimental studies, Weinbaum et al.(161, 162, 167) proposed several theoretical models appling revised Starling principle to describe the the layer permeability.

1.2.5.3. Coagulation

The endothelial glycocalyx layer, heparan sulfates in particular, plays a major role in regulation of coagulation (15, 83). Heparan sulfates bind to antithrombin III in the plasma and promote anticoagulatory process in the endothelium (89, 91). In general, antithrombin forms complexes with all serine proteases of the coagulation pathway and thus interacts with the coagulation cascade at various levels. The binding of antithrombin to specific carbohydrate ligands in the heparn sulfate (as well as heparin) dramatically accelerates this complex formation and greatly increases the biological activity of antithrombin (117).

1.2.5.4. Blood cell interaction

The interaction of white blood cells with the endothelial surface layer is critical for their adhesion and intrusion into the inflammatory sites (82, 118). A wide range of receptors and ligands both on the leucocyte and endothelial surface (including L-, E-, and P-selctin, integrins, ICAM-1, ICAM-2 and VCAM-1) are involved in this process (82). Several recent studies suggest that the interaction of certain adhesion molecules are mediated by the heparan sulfate component in the glycocalyx (138). On the other hand, activated immune cells can release enzymes that degrade the glycocalyx layer. For instance, heparinase is produced by activated immune cells to cleave heparan sulfate glycosaminoglycan side chain from the glycocalyx matrix (13, 80, 90).

Previous understanding of neutrophil-endothelial interaction is based on the assumption of a clear endothelial membrane decorated with protein receptors no more than tens of

nanometer thick (141). The presence of a half-micron thick glycocalyx layer on the endothelial membrane would thus very likely create a far distance (>100nm) between the ligands on the leukocyte microvilli and the endothelial receptor. Theoretic predictions by Zhao *et al.* (168) suggests that even the longest leukocyte microville will be unable to penetrate the glycocalyx layer and initiate cell rolling, unless it passes through regions of low shear or flow reversal (vascular sites known to be more prone to inflammatory response). This seems consistent with the idea that an intact glycocalyx layer may serve as a mechano-chemical barrier against leukocyte recruitment in uninflammed tissue (161).

In a nutshell, there has been an increasing body of evidence suggesting the important phiological functions of the glycocalyx since the first clear demonstration of layer existence. This layer, as an interface between the blood and the endothelium, is likely to be involved in a number of biological events in the vascular system, including inflammation, mechanotransduction, vascular resistance and atherosclerosis. This paper thus, summarizes our intention to investigate the biomechanical aspects of the glycocalyx and the experimental outcome.

Chapter 2. Glycocalyx Modulates the Motilitly and Proliferative Response of Vascular Endothelium to Fluid Shear Stress

2.1. Introduction

The endothelium plays a number of important roles in the vascular system including mediation of leukocyte adhesion and inflammatory responses, the regulation of vascular permeability, and would healing. Dysfunction of endothelial cells may lead to various pathological conditions, e.g. the early development of atherosclerosis (122). Endothelial cells are constantly exposed to hemodynamic forces, which in turn have a profound impact on cell morphological and functional responses (35, 48, 74). Mechanotransduction, the transformation of mechanical forces into a biochemical response, has been studied over the previous years. Endothelial cell mechanosensors that were previously proposed include integrins, G proteins, intercellular junction proteins, and ion channels (54). Recent investigation of the glycocalyx has lead us into a new perspective that this "bush-like" structure (162) on the apical membrane may play an important role in mechanotransduction (41, 55, 64, 131, 146, 147, 149, 157).

The glycocalyx is composed of various proteoglycans, glycosaminoglycans (GAGs), glycoproteins and associated plasma proteins (109). It serves as an interface between the blood flow and the endothelial cells, thus providing a structure that senses the fluid shear stress exerted by the extracellular flow and transmits it to the intracellular structure. Florian et al (55) reported that removal of heparan sulfate GAGs can completely stop nitric oxide (NO) production in cultured endothelial cells in response to shear. Mochizuki

et al(93) also reported that removal of hyaluronic acid GAGs can inhibit 80% of NO production in response to shear. In addition, Ainslie et al (1) have shown that removal of chondroitin sulfate GAGs in the glycocalyx greatly affects the contraction response to increase in shear in smooth muscle cells. Combined together, these evidence lead to the idea that maintaining the stability of the integral structure of the glycocalyx is important in mechanotransduction (147). Thi *et al.* reported that the disruption of the glycocalyx can affect the actin cytoskeleton reorganization and focal adhesion localization after cells were exposed to 5 hr of laminar shear, and proposed a bumper-car model for the role of the glycocalyx (149). More recently, Moon *et al.* examined the role of cell surface heparan sulfate proteoglycans in endothelial cell migration and proposed that heparan sulfate proteoglycans may be involved in sensing the direction of the flow (95). Recent *in vivo* work has revealed a correlation between the glycocalyx dimension and atherosclerosis development, where after 6 weeks of atherogenic diet, glycocalyx size was significantly decreased in the mice carotid artery; at the same time, evidence of enhanced atherosclerotic deposits was observed in these mice (153) .

Here, we investigated the role of the glycocalyx in both endothelial cell's short term and long term responses by using heparinase III to cleave heparan sulfate GAGs on the cell surface. It is well recognized that cultured endothelial cells align in the direction of flow after exposed to 24~48 hr of laminar flow (48, 114), and the endothelial proliferation is highly suppressed during flow application (81). As observed in our experiments, heparinase treated cells did not align in the flow direction, and they proliferated as if there were no flow present. On the other hand, control endothelial cells quickly response

to the onset of laminar flow by decreasing their migration speed by 40% in the first hour (102) and increasing the amount of VE-cadherin in cell-cell junctions (113), yet these two phenomena were not found in our Heparinase degraded cells. Our results suggest that heparan sulfate proteoglycans, or the glycocalyx in general, plays an important role in mechanotransduction.

2.2. Materials and Methods

2.2.1. Cell Culture and Heparinase Treatment

Primary bovine aortic endothelial cells (BAEC-77, passage 5-15) and human umbilical vein endothelial cells (HUVEC, passage 1-3) were a gift of Guillermo Garcia-Cardena (Department of Pathology, Brigham and Women's Hospital, Boston). All cell culture reagents were purchased from Sigma unless otherwise specified. BAECs were cultured in DMEM supplemented with 10% fetal calf serum, 1% L-glutamine, and 1% penicillin-streptomycin. HUVECs were cultured in M199 supplemented with 20% fetal calf serum, 1% L-glutamine, 1% penicillin-streptomycin and 100μg/ml ECGS Endothelial Mitogen (Biomedical Technologies, Stoughton, MA). Before seeding, cell culture flasks and glass slides were coated with 0.2% Gelatin. Cell cultures were kept in a humidified incubator maintained at 37^0C, supplied with 5% CO2 and 95% air.

Heparainase III used to cleave heparan sulfate GAGs in glycocalyx was a gift from David Berry (Department of Bioengineering, Massachusetts Institute of Technology). To degrade the cell surface glycocalyx, cells were washed twice in serum free medium and incubated in a 60mU/mL heparinase III solution for 30min.

2.2.2. Immunofluorescence and Microscopy

Heparan Sulfate antibody FITC (US biological, Swampscott, MA) was used to assess heparan sulfate removal by heparinase III, following the staining procedure described by Thi *et al.* (149). Both control and shear-exposed cells were labeled by CellTrace red-orange AM (Invitrogen) to detect cell nucleus or VE-cadherin antibody (BD Transductions Laboratories) to detect cell-cell junctions. Briefly, cells were incubated with CellTrace for 30min, then chilled on ice and blocked with 2% goat serum and 2% horse serum for 30 min, followed by rinsing three times in ice cold PBS. Then cells were treated with heparan sulfate antibody (FITC conjugated) for 1hr on ice. After that, cells were washed in PBS and fixed in 4% paraformaldehyde for 20min at room temperature, and mounted on microscope slides for imaging. For VE-cadherin staining, human cells were treated with mouse anti-Cadherin-5 MAb primary antibody for 1 hr, and washed three times and treated with Cy-3-conjuated goat anti-mouse IgG secondary antibody for another 30min. Images were acquired using a cooled CCD camera (Apogee Instruments Inc.) on a Nikon Eclipse TE2000 microscope with a 63X water immersion objective and MaxIm DL software (Apogee Instruments Inc).

2.2.3. Shear Aparatus

A parallel-plate flow chamber was used to expose cultured endothelial cell monolayer to laminar fluid shear stress. The chamber is composed of two acrylic plates (developed in our laboratory) separated by a piece of silicon gasket (Allied Biomedical Inc.), and the flow channel is created by removal of a 10mm X 150mm rectangular section from the

gasket. A cover slip with a confluent EC monolayer is placed in a rectangular recess on the bottom plate, and the central region of the monolayer is exposed to flow. The flow chamber is maintained in a customized hood set up on the microscope stage to maintain 37°C and 5% CO_2. Laminar flow is generated by a peristaltic pump (Barnant Inc.) that is connected to a damper to eliminate pulsations. At a flow rate of 80ml/s, cells are subject to a shear stress of 15dynes/cm^2.

2.2.4. Cell-migration Speed and Alignment Measurement

Cell speeds were determined by time-lapse video microscopy. Bright field images of a confluent EC monolayer were taken every 5 min. About 35 cells were randomly chosen in each experiment, and their nucleus positions in each image were tracked over time using Image J software. The crawling speed of each cell was thus calculated based on their nucleus trajectories, and the mean speed was calculated based on the statistics of 35 cells. Each experiment was conducted at least three times.

Cell alignment was quantified by measuring the angle of the longest cell body direction with respect to flow direction. The axis of the cell elongation was manually identified using Image J (National Institute of Health) for 100 cells in each experiment, and its relative angle to flow direction was then calculated and grouped into the corresponding category ranging from 0 to 90 degrees for each 10 degree increment.

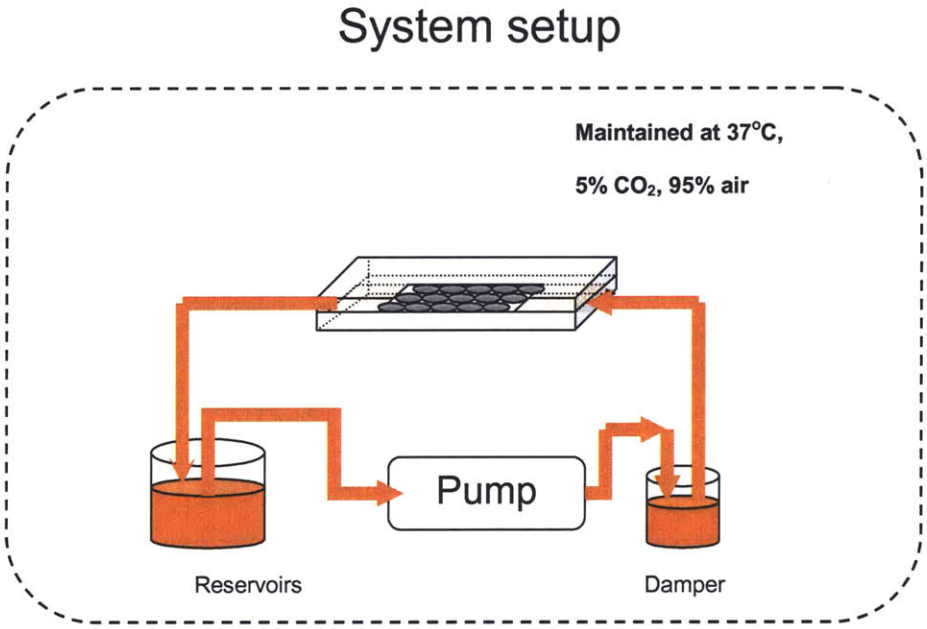

Figure 2-1 A customized microfluidic system to apply fluid shear stress to cultured endothelia cells placed in the flow chamber. The system is maintained at 37^0C, with 5% CO_2 and 95% of air.

2.3. Results

2.3.1. Heparan Slfate GAG Rmoval by Heparinase III.

To evaluate the effectiveness of heparan sulfate GAGs removal by heprainase III, we compared the fluorescent intensity of cell suface HSGAGs between control BAECs and enzyme degraded BAECs. As shown in Fig 2-1, heparainase treatment caused a 60.1± 5.4% decrease in the intensity of heparan sulfate antibody stained on the cell surface. This distinct immunofluorescent result confirmed the effectiveness of the enzyme treatment since a much lower level of heparan sulfate GAGs were observed after degradation. We strictly followed the immunostaining protocol provided by Thi *et al.* where 3D reconstruction of confocal fluorescent images has shown HSPG staining specifically on cell apical surface (149). All results are reported here as the mean ± standard deviation, N=3, unless otherwise noted.

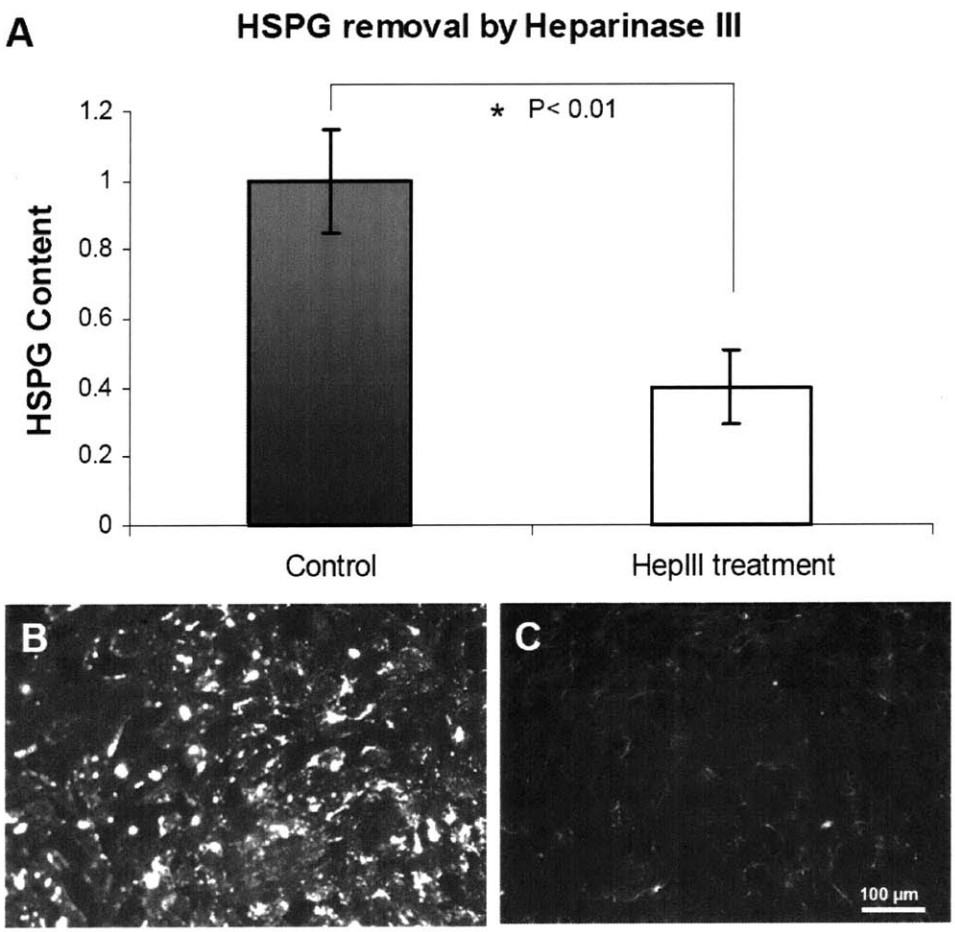

Figure 2-2 A) HeparinaseIII treatment (60mU/ml for 30min) removes cell surface HSPG by 60.1± 5.4% (n=3). Representative immunostaining of HSPG on confluent monolayers of control BAEC (B) and Heparinase degraded BAEC (C).

2.3.2. Long Term Flow Response of EC

Long term laminar flow application affects endothelial cell morphology in various ways. Control endothelial cells in a monolayer under static condition display a polygonal shape with no preferred orientation. Previous results have shown that when endothelial cells were exposed to laminar shear stress for 24~48 hours, cells elongate and align in the direction of the flow (49, 114). We subjected both untreated BAEC and heparinase treated BAEC to a shear stress of 15 dynes/cm^2. The untreated BAEC elongated and aligned in the direction of the flow as expected; however, heparinase treated BAEC did not align under flow (Fig 2-2A). Cell alignment was quantified by measuring the angle of the major axis of cell elongation with respect to the flow direction. Under static culture condition, cell elongation in both control and treated BAEC monolayers distributed randomly in all possible angles from 0 to 90 degrees (Fig 2-2C), while long term flow exposure caused the untreated cells to align in the direction of flow (with most of the cells elongating in the axis less than 20 degrees with respect to flow). HepIII treatment blocked the alignment of HUVECs in response to shear (data not shown). Another key flow response of EC is that shear stress causes a dose-related reduction of EC proliferation rate (81). We found that glycocalyx degraded EC's proliferation was not suppressed by flow, and those cells tended to proliferate at the same rate as they would under static conditions. Fig 2-2B compares the BAEC proliferation rate under the following four conditions: 1) control BAEC no flow; 2) control BEAC with flow; 3) degraded BAEC no flow and 4) degraded BAEC with flow. The results corroborated that heparinase treatment alone did not significantly affect EC proliferation under static conditions; when subjected to flow, the degraded cells proliferated at the same rate as if

there were no flow present. Considering the fact that two distinct features of control EC flow response were not observed on degraded cells, these results suggest that the glycocalyx plays a pivotal role in mechanotransduction of applied shear.

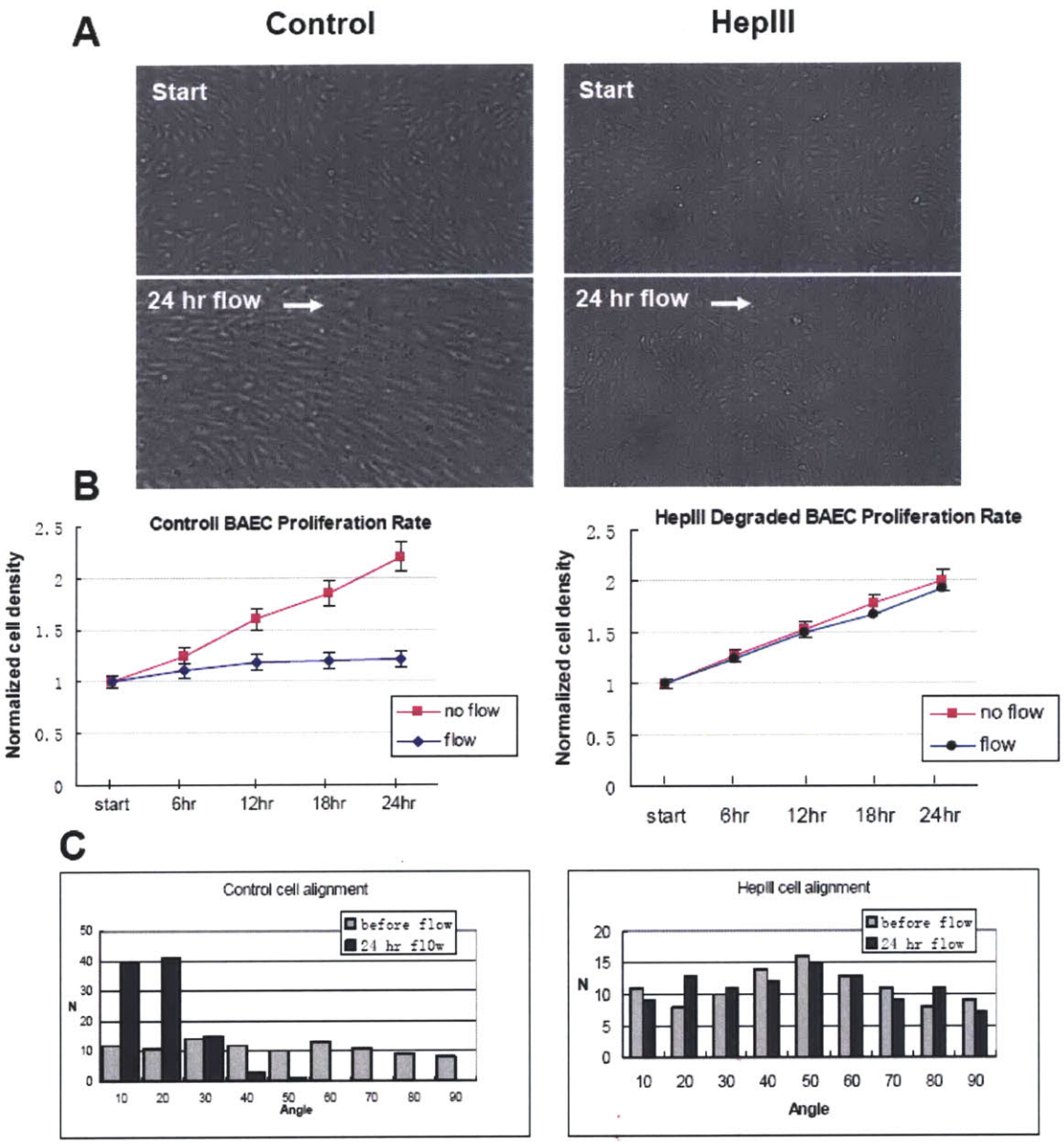

Figure 2-3 After 24hr of shear stress application at 15dynes/cm2, (flow from left to right) A) Control BAEC monolayer aligns in the direction of the flow, while degraded BAEC monolayer do not exhibit alignment. B) Comparison of BAEC proliferation under i) control cell no flow condition, ii) control cell flow condition, iii) HepIII degraded cell no flow condition and iv) HepIII degraded cell flow condition. HepIII treatment itself does not affect cell proliferation at static however, under flow application only untreated cell proliferation is suppressed by shear. C) cell alignment characterized by measuring the angles of the axis of each cell's longest body length with respect to the direction of the flow.

2.3.3. Rapid Flow Response of EC

Endothelial cells quickly respond to shear stress as soon as the flow starts. Within a few seconds of flow application, intracellular free calcium concentration increases significantly (133). The motility of BAEC in a confluent monolayer slows down by 40% during the first couple of hours of flow application; while at the same time, the actin filament turnover rate increases and the amount of polymerized actin decreases, resulting in the acceleration of actin filament remodeling in individual cells (102). The accelerated actin filament remodeling should have enabled the cells migrate faster, and the suppression of cell movement may be attributed to the strengthening of cell-cell junctional forces (113). We measured the migration speed of endothelial cells in a confluent monolayer, and found that the normal cells respond to flow with a 40% drop in the first couple of hours as previously reported, while the migration speed of glycocalyx-degraded cells after flow onset maintained the same level as static condition (Fig 2-3A). Cell migration speed curves as long as 24 hours for both cases are shown in Fig 2-3B, indicating the initial motility drop for control cells does not extend over hours in the later time course under flow. In addition, HUVECs in a confluent monolayer exhibit a similar response: control cells experience motility drop under shear initiation, while heparinase degraded cell motility is unaffected by the flow initiation (data not shown). Pretreatment of heparinase III on a confluent EC monolayer however, slightly reduces the motility of EC in static cultures by ~20%. Degraded cell crawling speeds gradually recover over a period of around 6 hours (Fig. 2-3B), which is of the same time scale required for the glycocalyx layer to be regrown (personal communication with Dr. Sasisakharan at MIT). As cell migration is a complex process including both mechanical driving forces and

biochemical reactions, it is plausible (though not fully understood) that the role of glycocalyx as a transport facility for biochemical molecules such as growth factors (5, 16) can explain this slight motility change of the degraded cells at static condition.

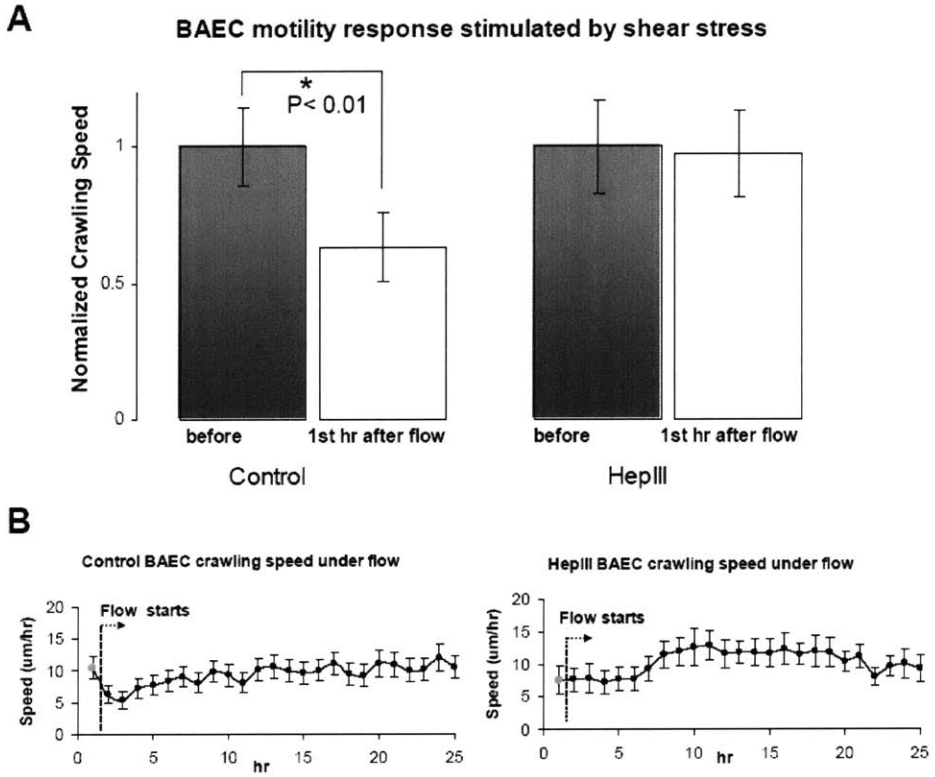

Figure 2-4 BAEC motility response under flow application. A) control BAECs decrease their crawling speeds by ~40% after first hour of flow, while HepIII degraded BAECs maintain the same motility level under flow. Bars indicate ± SD for three independent experiments in each case. B) Representative crawling speed curves for control and HepIII BAECs during 24 hr of flow application. Bars indicated ± SD for 35 cells in a single experiment.

2.3.4. Redistribution of Heparan Sulfate Proteoglycan on Cell Surface after Flow Application.

After 24 hr of laminar flow application, we examined the heparan sulfate proteoglycan distribution to check whether the state of cell surface glycocalyx itself may be altered by flow. As shown in Fig 2-4, endothelial cells without flow application exhibit a uniform distribution of glycocalyx across the cell surface. After 24 hr of flow application, a distinct peripheral staining pattern was observed. A double staining of cell tracker in red and glycocalyx antibody in green on BAEC after flow reveals that the glycocalyx is most prominent in the junctional regions away from the nucleus. This was further confirmed by observing the co-localization of the junctional protein VE-cadherin (red) and glycocalyx (green) in HUVEC as shown in the bottom panel (HUVEC was used in this case due to the availability of the VE-cadherin antibody).

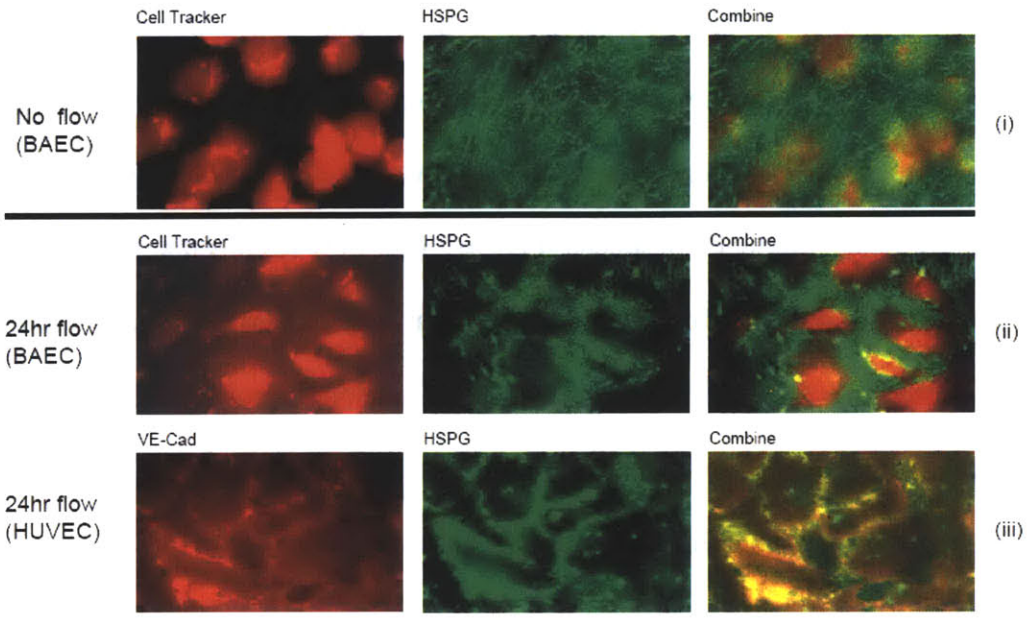

Figure 2-5 HSPG redistribution under flow application. (i) BAEC No flow, with Cell Tracker in red and HSPG in green. (ii) BAEC and (iii) HUVEC after 24hr laminar flow application, peripheral staining pattern of the glycocalyx. HSPG in green, with either cell tracker in red (ii) or VE-cad in red (iii). Note : HUVEC is used in (iii) as VE-cad antibody works against HUVEC.

Based on these results, we conclude that long-term flow application can lead to the redistribution of glycocalyx into the junction regions. We propose that the redistribution of glycocalyx may be a cell adaptive mechanism to reduce the shear gradient experienced by the cell apical surface. The hypothesized model of glycocalyx is illustrated in Fig 2-5. As reported previously (43), endothelial cells in a disturbed flow region with a high shear gradient do not align under flow, and most of them tend to escape from that region. Even in the laminar region, the waviness of the monolayer surface due to the heterogeneity of endothelial cell morphology still results in shear stress gradients on a subcellular scale (10). AFM measurement has shown that cell height modulation under flow was around 1.8 ±0.5 micron (10), which is of the same order as the *in-vivo* glycocalyx thickness (153, 157); at the same time, mathematical modeling has predicted the maximum subcellular shear gradient close to 10^4 dyne/cm^3 (124), even higher than the shear gradients in a disturbed flow region(10, 47). Hence, the mechanical stiffness of this glycocalyx structure may function to smooth the surface of cell monolayer under flow, thus reducing the shear gradients to which the cell body is exposed. Up to now, limited data exist for *in-vitro* glycocalyx thickness and previously reported electron microscopy results suggest the level of glycocalyx expression on cultured endothelial cells may not be as abundant as *in-vivo* and may also be regulated by the duration and strength of flow exposure (152); therefore, a careful *in vitro* study of glycocalyx thickness would be extremely useful.

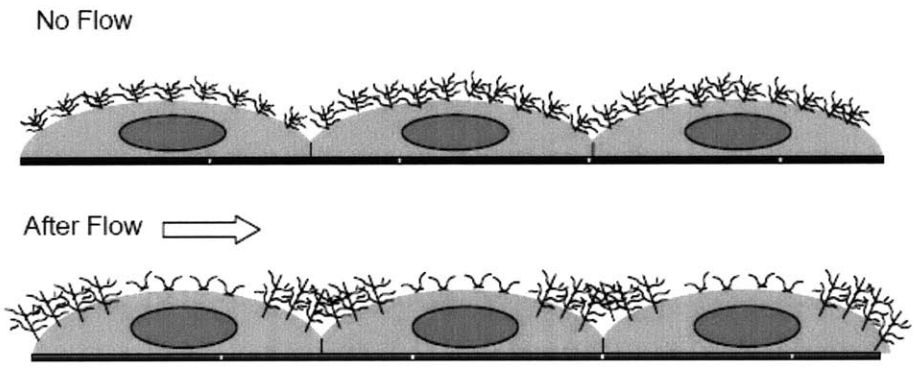

Figure 2-6 Hypothesized model of glycocalyx redistribution under flow. At static condition, cells express a relatively uniform glycocalyx layer on apical surface. During flow application, the glycocalyx components relocate from the central region to cell-cell junctions resulting in a distinct peripheral pattern, which may help reduce the shear gradient cells experience under flow.

2.4. Conclusion and Discussion

In this chapter, we have examined the role of the glycocalyx in mechanotransduction by studying the well-characterized responses of endothelial cells to fluid shear stress. The responses of the glycocalyx degraded cells differ significantly from control cells in several ways 1) 24~48 hr of laminar flow application is not sufficient to induce degraded cell's alignment and proliferation suppression as compared to normal cells; 2) Flow onset does not cause degraded cells to migrate significantly slower than static condition, as opposed to untreated cells which rapidly decrease their motility by 40% during the first few hours of flow application. In concert with several other recent studies of the endothelial glycocalyx (55, 146, 147, 149), we conclude that the glycocalyx plays an important role in mechanotransduction, and further that the removal of the glycocalyx appears to turn off the EC response to shear stress. The evidence of reorganization of glycocalyx under flow also leads us to speculate that not only does the glycocalyx transform mechanical force into biochemical signals inside the cells, but it also has an adaptive mechanism to reorganize itself so as to reduce the shear gradient to which individual endothelial cells are exposed under flow. This may also be of interest to studies such as the effect of tissue loading in the cleft region(167). Other researchers have reported that fluid shear stress could stimulate the incorporation of hyaluronan into the glycocalyx matrix(64), and increased synthesis of sulfated GAGs was also observed under high shear stress (40 dyn/cm^2) condition (6). Fluid shear may as well promote HSPG synthesis, but our data at the moment are insufficient to resolve this question.

Moon et al. (95) found that disruption of heparan sulfate proteoglycans increased isolated endothelial cell migration speed. This may seem contradictory to our observation that heparinase III treatment itself slightly decreased cell migration speed by around 20% in a monolayer. However, we should notice that in Moon's paper, cells were detached and resuspended in heparinase solution to remove glycocalyx, before they were seeded on fibronectin coated surfaces for experiments. Therefore, the disruption of heparan sulfate proteoglycans not only occurred on cell apical surface, but in the basal membrane as well. Since heparan sulfate proteoglycans are also actively involved in cell adhesion formation, the reported increase in migration speed may be attributed to the weakening of cell adhesion, which is in concert with the data shown later in their paper that decreasing cell adhesion by lowering fibronectin density enhanced endothelial cell migration. In our study, intact cell monolayers were treated with heparinase for 30min to remove the apical surface glycocalyx, without significantly affecting the existing focal adhesions; therefore, our approach differs from Moon *et al.*'s and leads to different observations. As we know, the glycocalyx serves various important functions that maintain the health of endothelium, such as providing a selective permeability barrier for macromolecules (52, 153, 154, 156), forming a lubrication layer to assist red blood cell passing through capillaries (39, 132), and interacting with fibroblast growth factor (FGF) in regulating proliferation (17, 18). The mechanism behind this motility change by glycocalyx degradation is still under study.

Several theoretical models of the glycocalyx are formed based on the prediction that the Brinkman layer of flow interior to the glycoclayx is very small (39, 109, 147). Therefore, the fluid shear stress is exerted on the top surface of the glycocalyx, and the plasma

membrane itself bears little shear stress (146, 147, 149, 162). One possible mechanism of mechanotransduction through glycocalyx is that the fluid shear is sensed by the core proteins in the glycocalyx structure and transmitted to the actin cytosckeleton via the transmembrane domain. Heparin sulfate GAGs are known as the most abundant glycosaminoglycans on the endothelial suface, comprising 50~90% of the total GAG amount (56). Syndecan-1, -2 and -4, all expressed on ECs, have sufficient GAG attachment sites in the extracellular domain as well as a cytoplasmic tail linked with actin cytosckeleton (14, 91, 136, 151). Therefore, the syndecans are the most likely candidates for transmitting the fluid shear stress. Their cytoplasmic domains bind to several intracellular proteins including ezurin, tubulin, Src kinase, cortactin, dynamin and α-actinin (146, 151, 166), and signaling through syndecans can regulate cytoskeleton organization through their clustering, association with actin cytoskeleton, binding to cytoplasmic binding proteins, and intracellular phosphorylation (166). As a result, fluid shear stress transmitted through syndecans may be able to induce the displacement of actin filaments and start the intracellular signaling cascades (149, 162).

Thi et al (149) describe a "bumper-car" model which proposes that the shear force exerted on the glycocalyx may be sufficient to overcome a threshold of mechanical force that may lead to the adherins junction rupture and the formation of new stress fiber and focal adhesion. Considering the other possible biochemical pathways under flow, the role of glycocalyx under flow may well be a complicated coordination of both mechanical force and biochemical stimuli. The glycocalyx is acknowledged to be a permeability barrier for the endothelium (36, 156), and both theoretical and experimental studies have

shown the important sieving property for macromolecules as represented by the permeability of the glycocalyx (155, 162). Therefore, it is logical to assume that once the flow starts, the solute influx across the glycocalyx into the cell generated by the hemodynamic forces and the resulted intracellular signaling events may be affect by altering the state of the glycocalyx. Various biochemical molecules, such as growth factors, are involved in the control of endothelial activities such as proliferation and migration, and further studies are required to understand the role of the glycocalyx in modulating the transport of these molecules under flow. Because the glycocalyx is a complex matrix composed of a large amount of highly negatively-charged glycosaminoglycan strands, the flow modulated membrane diffusion and redistribution of some important signaling molecules such as adhesion or junctional proteins may also be affected by changing the state of the glycocalyx. *In vitro* or *in vivo* direct measurements of glycocalyx mechanical properties would be of great help in understanding the mechanism of red blood cell passing in small capillaries as well as white blood cell interaction with the endothelium. Combined with the recent discovery of apparent linkage between glycocalyx and atherosclerosis (153), it appears that the glycocalyx occupies a pivotal role in modulating vascular mechanotransduction and vascular disease.

Chapter 3. Nanometer-resolution Optical Imaging Method Using Quantum Dots as Biomarker

3.1. Introduction

As one of the major tasks of this thesis is to oberseve the dynamics of the endothelial glycocalyx under flow application, we need to determine the precise location of the structure during any given period under force impact with sub-second temporal resolution. And most importantly, this must be performed with living cells as the physiological conditions of the glycocalyx must be retained. Single particle tracking methods provide the possibility of tracking individual particles in living cells with an improved spatial resolution than microscope imaging. When using conventional fluorophores however, photobleaching under high magnification often causes substantial signal reduction that restrains the imaging time. Quantum dots therefore, known for their solid photostability and superior signal to noise ratio, are the ideal candidate as a fluorescent marker in our single particle tracer experiments.

The project in this chapter was completed as collaboration with Dr. Maxine Jonas, and the data shown below in large part were collected using the optical facility in Prof. Peter So's microscopy lab in the Department of Biological Engineering.

3.1.1.Quantum Dots

Quantum dots (QDs) are monodisperse inorganic nanoparticles made of semiconducting materials. When coated by a layer of biomolecules on the outside, QDs are typically 15~20nm in diameter, as shown in Fig 3-1. Quantum dots, known for their remarkable optical and photo-physical properties, have emerged as a superior biomarker, and successfully substituted traditional small molecule fluorophores in a number of bio-imaging applications.

3.1.1.1. Ultra-bright fluorescence provides superior signal level

QD semiconductor nanocrystals exibit much brighter signals than traditional fluorescent dyes. With an extremely high extinction coefficient (~10^5 $M^{-1}cm^{-1}$), much more of the excitation light is absorbed by QDs than with organic dyes, thus providing much brighter emission signals. The quantum yield of the nanocrystal core is relatively low (less than 10%)(3, 96), however a shell of high band-gap semiconductor material such ZnS is usually grown around the core to achieve the quantum yeld of up to 80%(70, 107). The extraordinary brightness of QDs also enables accurate quantitation of low-abundance biomolecules as well as locating the position of a single dot.

3.1.1.2. Unique optical spectrum enables multiplex imaging

Quantum dots exhibit high spectral specificity such that the size of the particle dictates its emission wavelength; therefore the colors of QDs can easily be customized by fine-tuning of the particle diameter (Fig 3-2). In addition, QDs have a broad excitation spectrum that widely differs from their emission spectrum. With FWHMs (full width at half maximum) of the emission spectrum typically < 30nm, QDs are particularly suitable

for multicolor fluorescence imaging, where biomarkers of a variety of colors can be excited by a single low-cost light source in conjunction with a set of filters.

3.1.1.3. Solid photostability yields long-term observation capability

QDs are very stable light emitters due to their inorganic composition, which makes them much less susceptible to photobleaching than to organic dyes (23). This has been shown in a number of biolabing experiments where the photostability of QDs was compared with widely used fluorophores, e.g. rhodamine, fluorescein, and Alexa-Fluor (23, 27, 50, 164). This extreme photostability is especially attractive for imaging tasks that require long period of observation window, including for instance, imaging of thick specimen that collects multiple cross-sectional data over time and following intracellular trafficking without interruption. In addition, relatively high laser intensity as well as long integration time can be used to improve sensitivity when detecting low-abundace targets. When used in confocal microscopy, unlike organic dyes, additional illumination by the laser source in different imaging planes does not photobleach the emission of QDs.

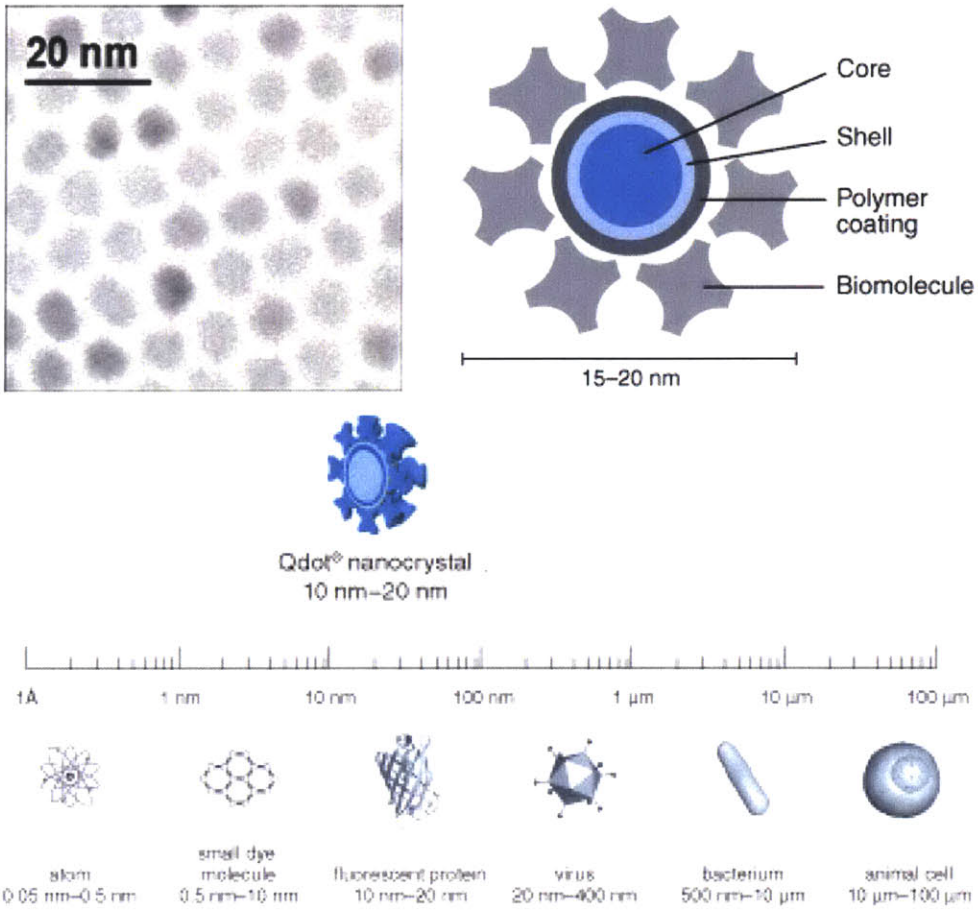

Figure 3-1 Typical size and structure of a single quantum dot. Upper left panel: electron microscopy image shows the diameter of a single CdSe dot within 10nm. Upper right panel: a functionalized quantum dot typically consists of a core-shell structure with additional polymer coating and an outside layer of biomolecules to enable its biocompatibility with targeted structures. Bottom: length scale of a nanocrostal compared to common biological substances.

[Source: www.invitrogen.com]

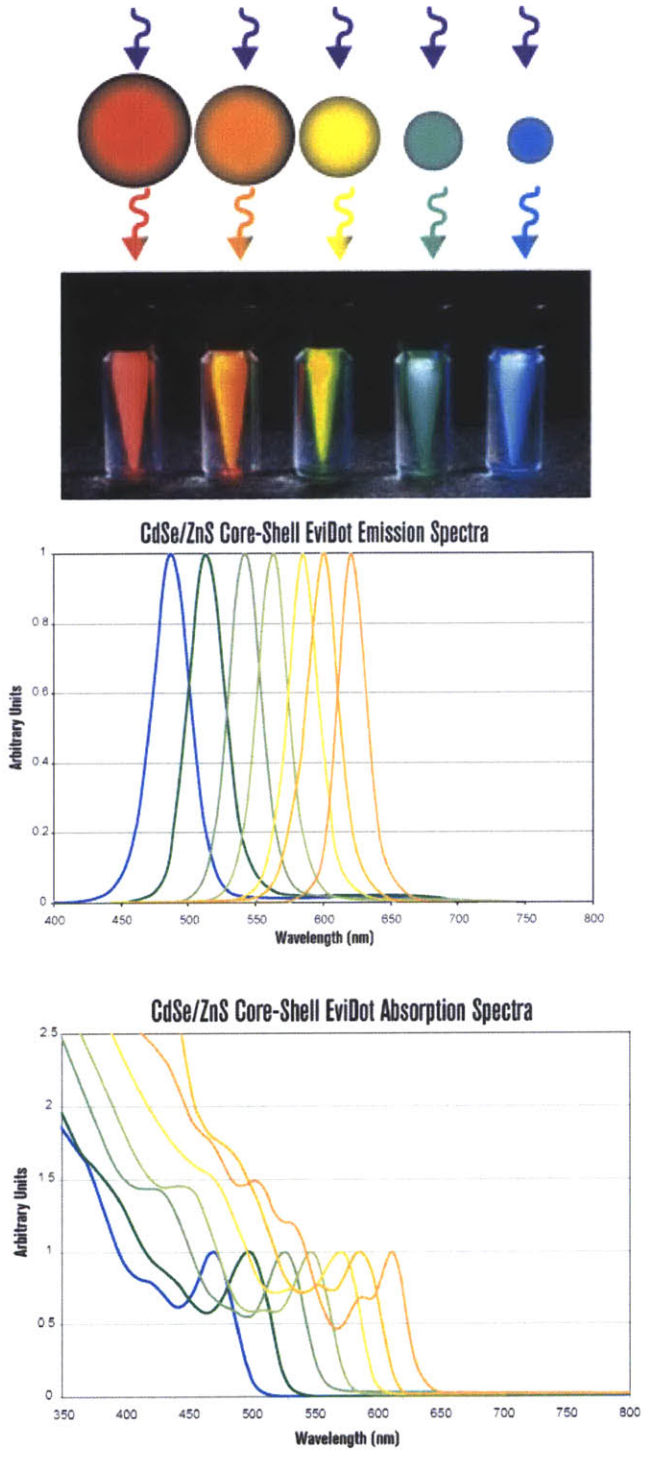

Figure 3-2 Excitation/emission properties of QDots. Top: five different quantum dot solutions are excited by the same UV source, and the emission color is dicated by the particle size. Below: quantum dots exhibit sharp emission spectrum when excited by a continuous band of light source.

[Source: www.evidenttech.com]

3.1.1.4. Advances in biocompatibility promises wide application in biological studies

The core and core-shell structured QDs alone are not water soluable due to their hydrophobic surface layer. Therefore, various techniques have been developed to stabilize core-shell nanocrystals in aqueous solutions. One of the existing methods is to exchange the hydrophobic surfactant molecules with bifunctional molecules that have hydrophic group on one side and hydrophobic group on the other. Quite often, thiols (-SH) are used to achor on the ZnS surface and carboxyl (-COOH) groups are adopted as the hydrophilic ends (3, 27, 144). Surface silanization is another method to solubilize the QDs by including a silica shell around the particle (23, 57). During silica shell growth, additional silanes can be added to produce different functional groups on the surface, for instance by using aminopropyl-silanes (APS), phosphor-silanes, or pholyethylene glycol (PEG)-silane (57, 104). Silanzied QDs are extremetly stable as a result of the highly cross-linked nature of silica shell, though the process of silanization is relatively more burdensome and the silica shell may be hydrolyzed in the end (92).

To investigate biological events using QDs as fluorescent probes, QDs can now be conjugated to a number of biomolecules without disturbing the biological functions of those targets. Common practice to link biological molecules to QDs include adsorption, electrostatic interaction, mercapto (-SH) exchange, and covalent linkage (3). One successful method is to coat the QD surface with functional groups such as –COOH, -SH or $-NH_2$, and add cross-linker molecules subsequently to link those nanocrystals to biomolecules that also have such reaction groups (23, 27, 28, 57, 106). Cross-linker 1-ethyl-3-(3-dimethylaminopropyl) carbodiimide (EDC) for example, is often used to link

-NH_2 and -COOH groups together (7). This technique can be applied in our study where EDC can catalyze the linkage between carboxyl-QDs and –NH_2 groups in the fibronectin solution, which may later be used as surface coating for cell culture device as well as a luminant indicator of substrate plane during optical imaging.

Numerous studies have reported successful conjugation of QDs to various biological molecules, including biotin(23); oligonucleotides (50, 79, 87); peptides (2, 108); and proteins, including avidin/streptavidin (164) and antibodies(27, 73, 164). For the purpose of double staining in our study, we use streptavidin-biotin pair to attach QD655 (QDs of emission wavelength at 655nm) to the cell surface heparan sulfate glycosaminoglycans to label glycocalyx layer; at the same time use IgG pair to locate QD605 (QDs of emission wavelength at 605nm) to endothelial membrane protein PECAM-1 as cell membrane indicator.

In summary, QDs are extremely bright biolabels, with much higher photostability and greater resistance to photodegradation compared with conventional fluorophores. The small size of the QDs makes them ideal for achieving single molecule detection sensitivity, at the same time, causing minimal disturbance to the physiological environment of the study.

3.1.1.5. Current limitation of quantum dots

Inspite of the superior qualities of QDs, there are some photophysical properties of QDs that can be disadvantageous in some cases. One of them is QDs' characteristic blinking, which means the nanoparticle randomly switch between an emitting state and a non-emitting state. This can cause confusions in experiments such as single molecule tracking, because it would be difficult to determine during no-signal period whether the dot has moved out of the detection range or it merely has swiched to an off-state. Fig 3-3 shows the random blinking of two single dots in the window during a five-minute recording. Up to date, there is limited evidence showing that QD blinking can be suppressed on some timescale by passivating the QD surface with thiol moieties (71). It has also been reported that QD fluorescence intensity increases upon excitation, refered to as photobrightening (57, 78). Both blinking and photobrightening are linked to mobile charges on the surfaces of the dots (3), and at present are still considered as limitations of QDs.

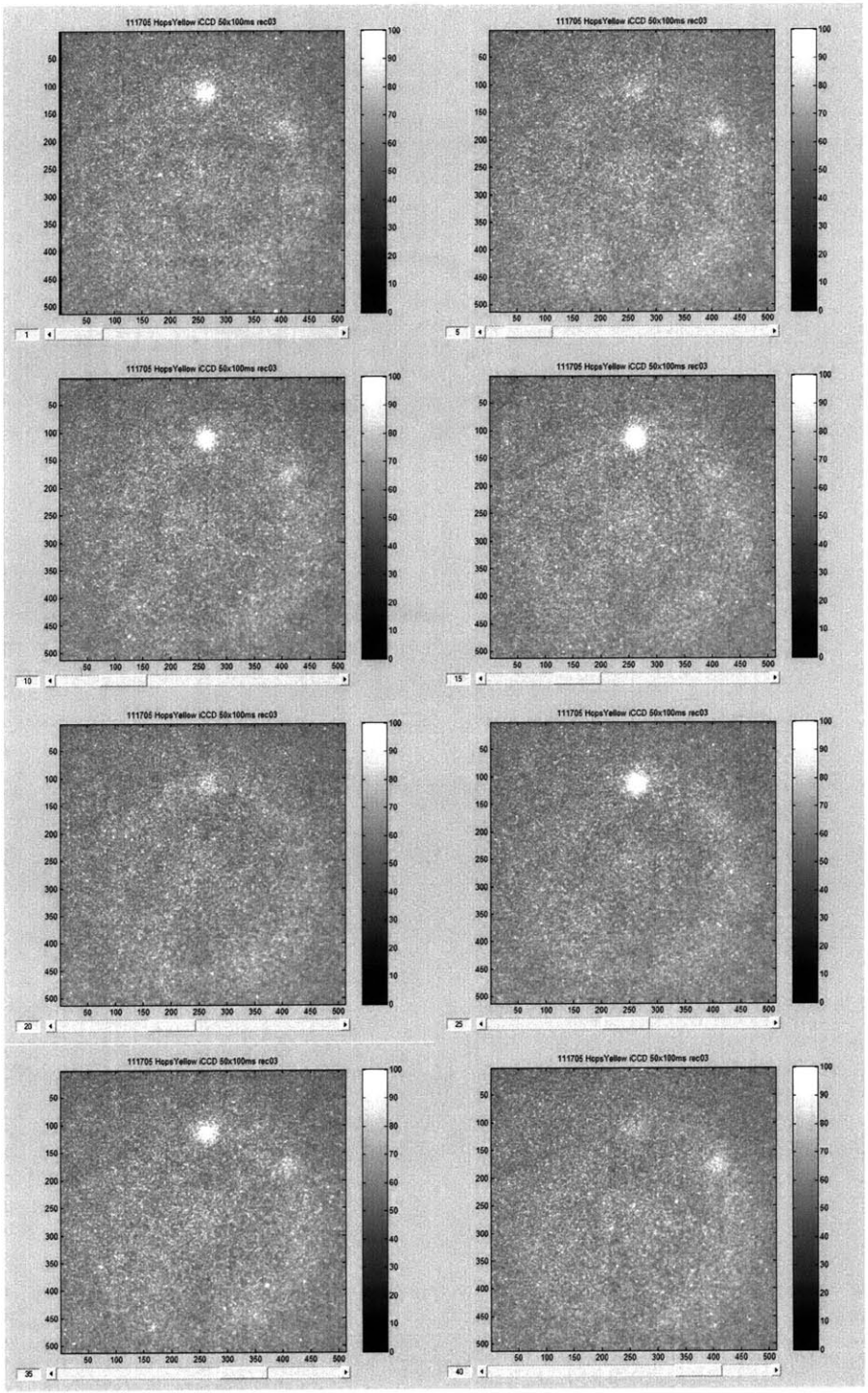

Figure 3-3 Successive images of two blinking QDs over time. Image integration per frame: 0.1s.

3.1.2. Existing high-resolution imaging techniques

Over the past decades, the field of biological experimentation has greatly extended into studying biological events on very a small length scale, sometimes even at molecular level. Therefore, ultra-resolution imaging techniques that can assist in investigating real-time signaling events and molecular-level structures are of great demand in the area. Conventional optical imaging have the advantage of easy operation on living cells; however, the diffraction of light in nature sets a limitation on the spatial resolution possibly achieved by such a method, which is on the order of ~250nm (half the wavelength of light). Electron microscopy on the other hand, can resolve structures that are sub-nanometer size; yet the harsh preparation process makes it impossible to observe on living objects (159). Moreover, sample fixation can greatly compromise the structure accuracy detected for certain tissues, and it may cause artifact that shields the original tissue structure. One example is the measurement of glyocalyx thickness. Electron microcopy data as early as in the 40s observed a very thin layer of proteins on the apical membrane of endothelium, which was the first evidence of this endothelial surface layer (25). Improvement in the staining technique over the years has shown the layer thicker than the original observation (31-33, 85), but the challenge to reveal the full extent of the glycocalyx layer remained as the structure is known to be fragile with high water content and it would have unquestionably be damaged to certain degree during the fixation. It was not until the mid 90's when Vink and Duling showed by intravital microscopy a continuous endothelial surface layer of about 0.4~0.5um thick did people start to appreciate the extensive coverage of this structure.

Single particle tracking (SPT) technique emerged in the recent years with broad application in microrheology, receptor diffusion, vesicle trafficking and so on (9, 97, 139, 150, 160). As commonly recognized, the resolution of a light microscope is limited to about $\lambda/2 \approx 250$nm, which means two objects closer than this distance is not resolvable. However, the center of the spot can be determined to a much greater precision (58, 129). By calculating the centroid of the images of individual fluorescent particles, we can locate the center of such a particle to a precision at least an order of manigtude greater than the microscope resolution. Thompson *et al* (150) examined the factors that limit the precision of this technique, and such as the number of photons in the spot as well as background noise. Having an optimized set of microscope parameters, the center of a fluorescent particle may be determined with nanometer precision.

With the introduction of quantum dots as biomarkers, single particle tracking techniques have gained increasing popularity in biological applications. Researchers have successfully observed the individual steps taken by motor proteins in living cells. For instance, microtubule motor proteins such as kinesin and dynein movements following 8nm steps in active transport were clearly visualized by tracking intracellular vesicles that contained quantum dots(97). The diffusion dynamics of membrane receptors, such as glycine receptors in the neuronal memberane, were revealed for periods ranging from milliseconds to minutes by single-quantum dot tracking (37).

Single particle tracking using quantum dots provides the opportunity of observing biological events with ultra-resolution in living cells. Our task in this chapter therefore, is

to establish an optical system that can trace tissue-imbedded single dots with nanometer precision and further apply the method to detect the dynamics of glycocalyx under flow.

3.2. Materials and Methods

3.2.1. Optical Setup

A laser beam (532nm from a Verdi ND:YVO_4, Coherent, Santa Clara, CA) is delivered with an optical fiber and collimated through a custom light path and a 100X NA1.30 oil objective (Olympus, Melville, NY) as shown in Fig.3-3. The light from the objective illuminates a 100 μm x 100 μm area of the sample that is placed on the stage of an Olympus IX71 inverted microscope and mounted on an *x-y* piezoelectric nanopositioning system (Queensgate, T-orquay, U.K.). The photons emitted by the QDs contained in the sample are filtered by a dichroic mirror and detected after beam expansion by a 12-bit intensified charge-coupled device (iCCD camera, Pentamax, Princeton Instrument, Trenton, NJ). To reduce mechanical and acoustic noise, all experiments are performed on a vibration-isolating floating optical table (TMC, Peabody, MA).

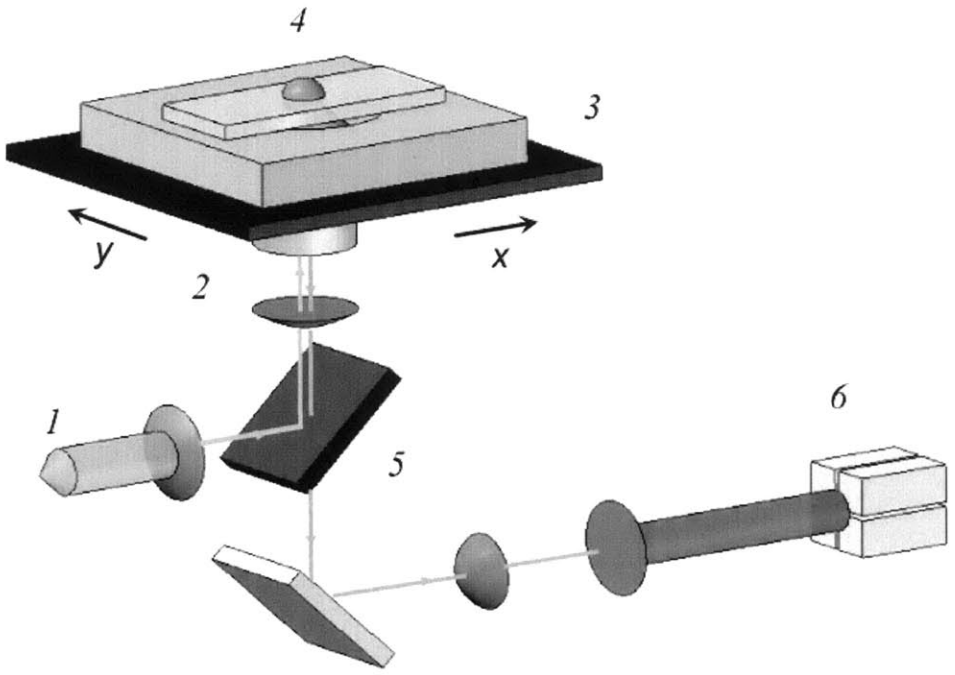

Figure 3-4 A schematic of optical setup for single quantum dot detection, which consists of: a laser source [1], a 100X NA 1.30 oil objective [2] (Olympus, Melville, NY), an excitation volume [4] placed on nanopositioning microscope stage [3], a dicroic mirror-barrier filter combition [5] (Q560LP and HQ585/40, Chroma Technbologies Corp., Rockingham, VT), and a 12-bit 512 pixels x 512 pixels intensified charge-coupled device [6] (iCCD camera, Pentamax, Princeton Instrument, Trenton, NJ).

3.2.2. Stage Oscillation Experiments

Streptavidin-conjugated Hops Yellow (CdSe/ZnS QDs of emission peak 560 nm) EviTag QDs (Antibodies Inc., Davis, CA) were immobilized onto a biotin-coated coverslip as follows. The No.1 ½ glass coverslip was treated with 1-μM bovine serum albumin (BSA)-biotin (Sigma, Saint Louis, MO) for 30 min and washed with water. Streptavidin-QDs (8 pM in water) were then added and the coated coverslip was sealed onto a microscope slide before imaging.

The coverslip was translated along one axis of the *xy* piezoelectric nanopositioner (Queensgate, 0.5-nm position accuracy in closed-loop mode) controlled by a custom program in LabVIEW (National Instruments, Austin, TX)/C++/Matlab (The MathWorks, Natick, MA).

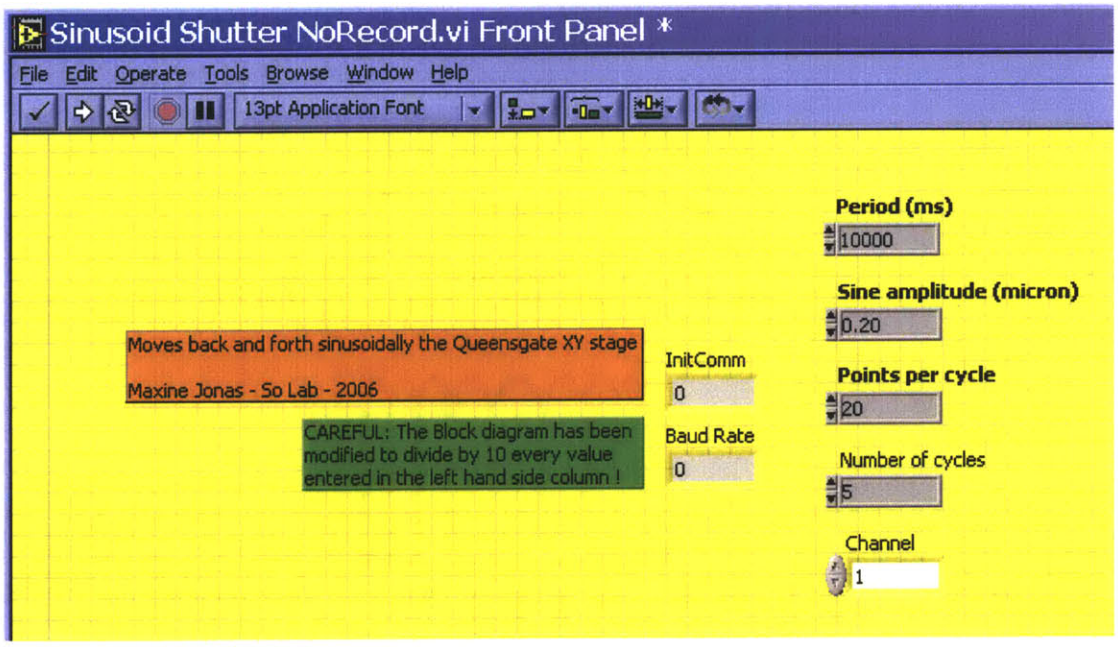

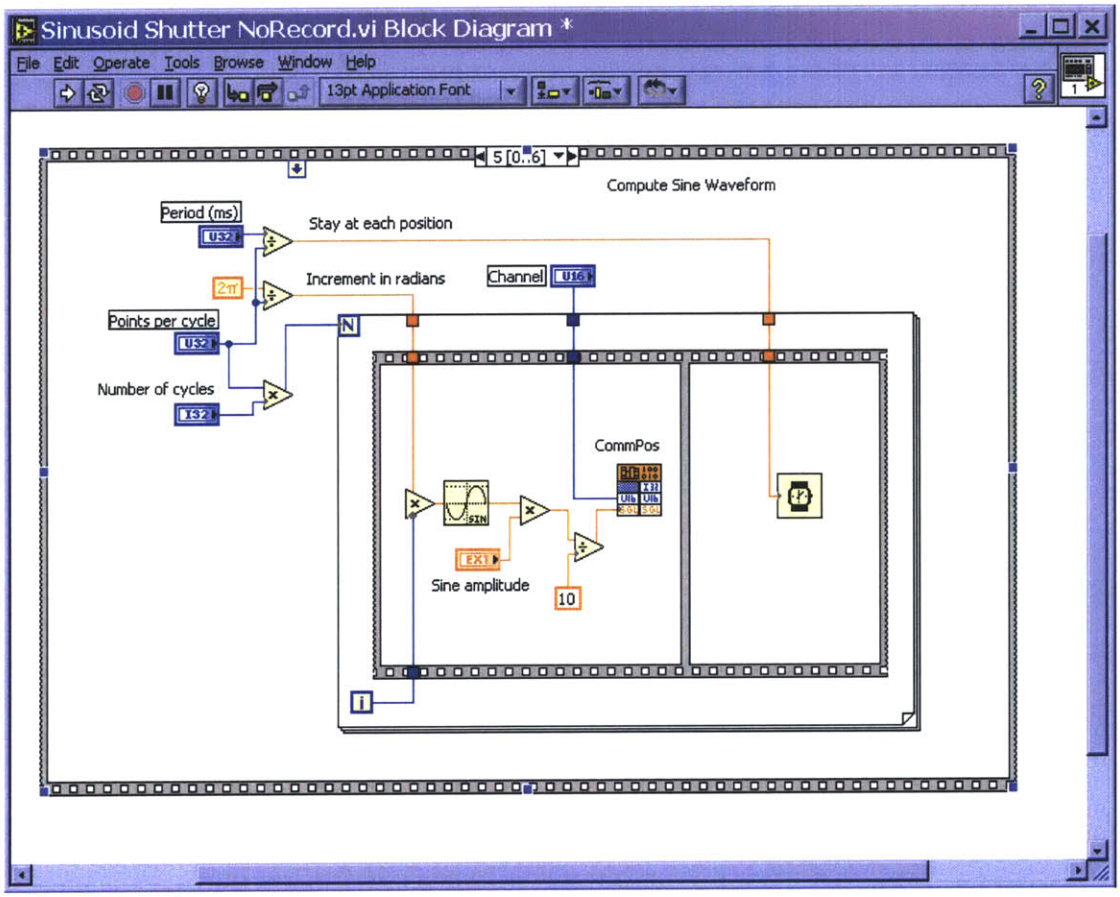

Figure 3-5 Illustration of Labview program to control the nanopositioner following sinusoidal command. ***[Courtsey of Maxine Jonas]***

3.2.3. Cell Sample Preparation

Primary bovine aortic endothelial cells (BAEC-77, passage 10-15) are cultured in DMEM supplemented with 10% fetal calf serum, 1% L-glutamine, and 1% penicillin-streptomycin. Before seeding, cell culture flasks and glass slides are coated with 0.2% gelatin at room temperature. Cell cultures are kept in a humidified incubator maintained at 37^0C, with 5% CO_2 and 95% air.

After cell monolayers reach confluence on glass slides, QDs are attached to the cell surface glycocalyx as follows. To reduce nonspecific background staining, cells chilled on ice are incubated with 2% goat serum and 2% BSA in phosphate buffer saline (PBS) for 20 min. After quick rinses with PBS, cells are incubated with 5 μg/mL heparan sulfate biotin antibody for 30 min and washed three times with PBS. Next, cells are incubated with 16 pmol/mL streptavidin-QDs for 20 min, and finally washed with PBS. Cell labeling procedure is completed on ice so as to limit QD endocytosis during the incubation procedure. Cell imaging on the microscope stage is performed right afterwards at room temperature.

3.2.4. Data Acquisition and Analysis

Images from the iCCD are captured using the WINview data acquisition software and saved as SPE files. A custom-written Matlab code is developed to fit one point spread function (PSF) in successive frames to a two-dimensional (2D) Gaussian function. The position of the QD's center is therefore determined by the Gaussian fitting and used to compute the particle trajectory over time.

3.2.5. Theoretical Principles

We determine the position of a QD's centroid by fitting the intensity profile (or PSF) of its diffraction-limited image to a 2D Gaussian function. This procedure returns the center of the light distribution and its uncertainty, described by the standard error of the mean, σ_μ, which is affected by the photon noise, the finite pixel size of the iCCD detector, and its background noise:

$$\sigma_\mu = \sqrt{\left(\frac{\sigma_0^2}{N} + \frac{a^2/12}{N} + \frac{8\pi\sigma_0^4 b^2}{a^2 N^2}\right)},$$

where N is the number of collected photons ($\sim 10^5$ per 0.5-s frame per 100 x 100 array of pixels on the iCCD chip, with a typical excitation power of 5 $\mu W/\mu m^2$ at the sample in our experiments), σ_0 is the width of the Gaussian distribution (~ 215 nm), a is the effective pixel size (a = 8.9 nm with 100X objective magnification and 16X further beam expansion), and b is the standard deviation of the background (due to background fluorescence and detector dark counts, typically b ~ $\sqrt{8}$ at the iCCD gain of operation). Thus, the theoretical value of σ_μ is 1.3nm, which predicts that ideally, our imaging technique can achieve nanometer spatial resolution.

3.3. Results

3.3.1. Photobleaching Effect of QDs

Quantum dots have been previously reported as extremely photostable, and they can remain the same emission level even after long period of high intensity excitation. For the purpose of single particle tracking in our experiement setup, we started with a high laser excitation power under 100 x magnification to obtain as many photons as possible from one single dot. In spite of the unquestionable photostability presented by the nature of the nanoparticles, moderate photobleaching effects were observed under our high level of laser input (~40 $\mu W/\mu m^2$).

Figure 3-6 shows a concentrated solution of quantum dots gradually bleached out after 30s of continuous illumination. In the case of OD0.0 where no neutral density filter was added, 40 $\mu W/\mu m^2$ of excitation power at the sample resulted in a significant reduction of the signal level during a half-minuite period. The addition of a neutral density filter of optical density (OD) 0.5 decreased the excitation power to $40 \times 10^{-0.5} = 12.5$ $\mu W/\mu m^2$ at the sample, but was not enough to prevent fast photobleaching of the QDs from occurring. Futher decrease in the excitation power by means of OD1.0 (excitation power = 4 $\mu W/\mu m^2$) or OD1.5 (excitation power = 1.25 $\mu W/\mu m^2$) greatly helped maintain the emission intensity up to minutes, thus provided the opportunity of un-interrupted long-time observation for our experiments. The decaying trend of quantum dot sample image intensity over time was approximated by an exponential decay in Fig 3-7, showing OD1.5 greatly improved intensity stability with an exponential decay time constant of 259s.

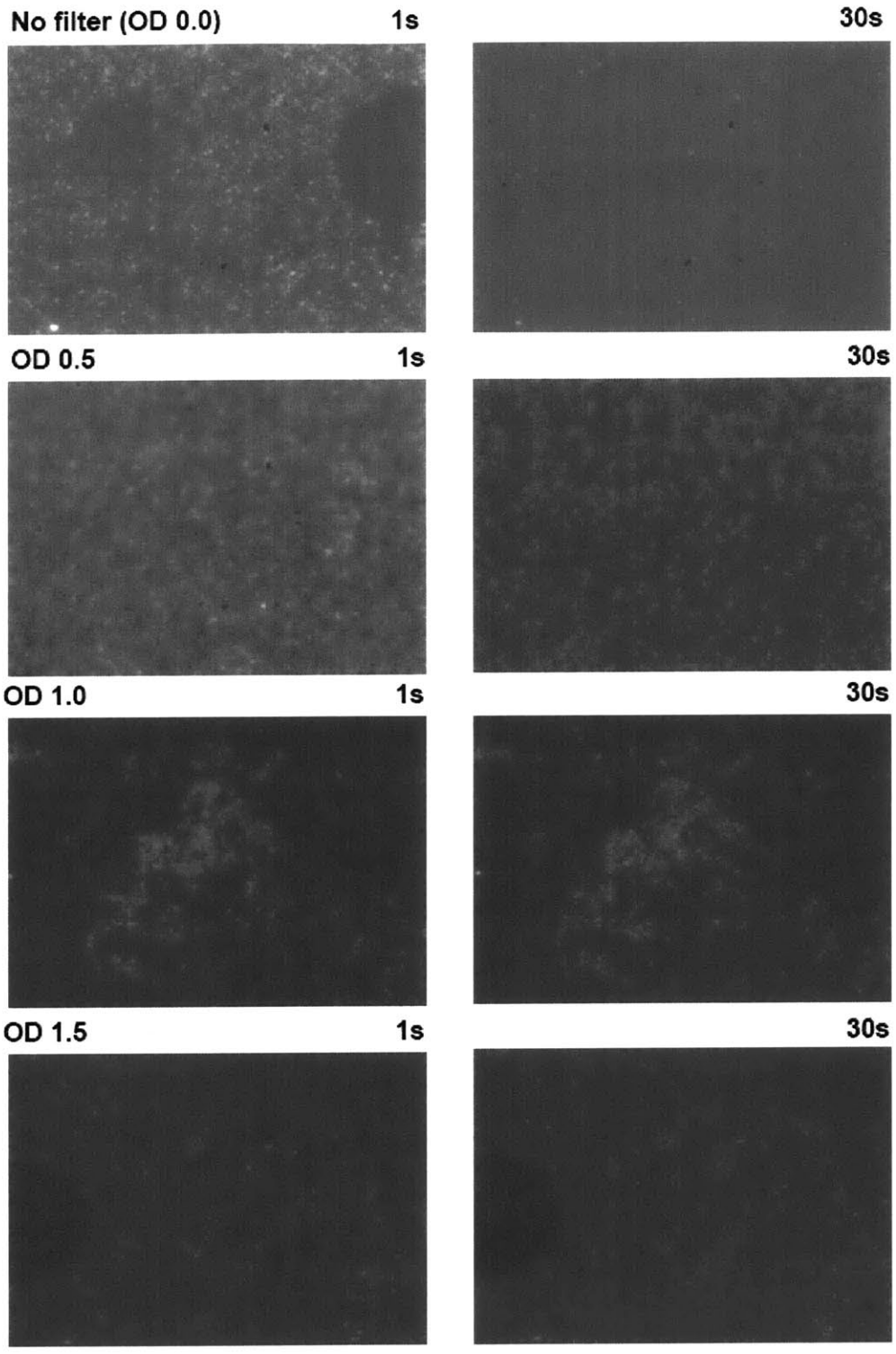

Figure 3-6 Photobleaching effect of a concentrated solution of quantum dots. Filters (OD0.0, OD0.5, OD1.0, OD1.5) were used to reduce excitation power accordingly.

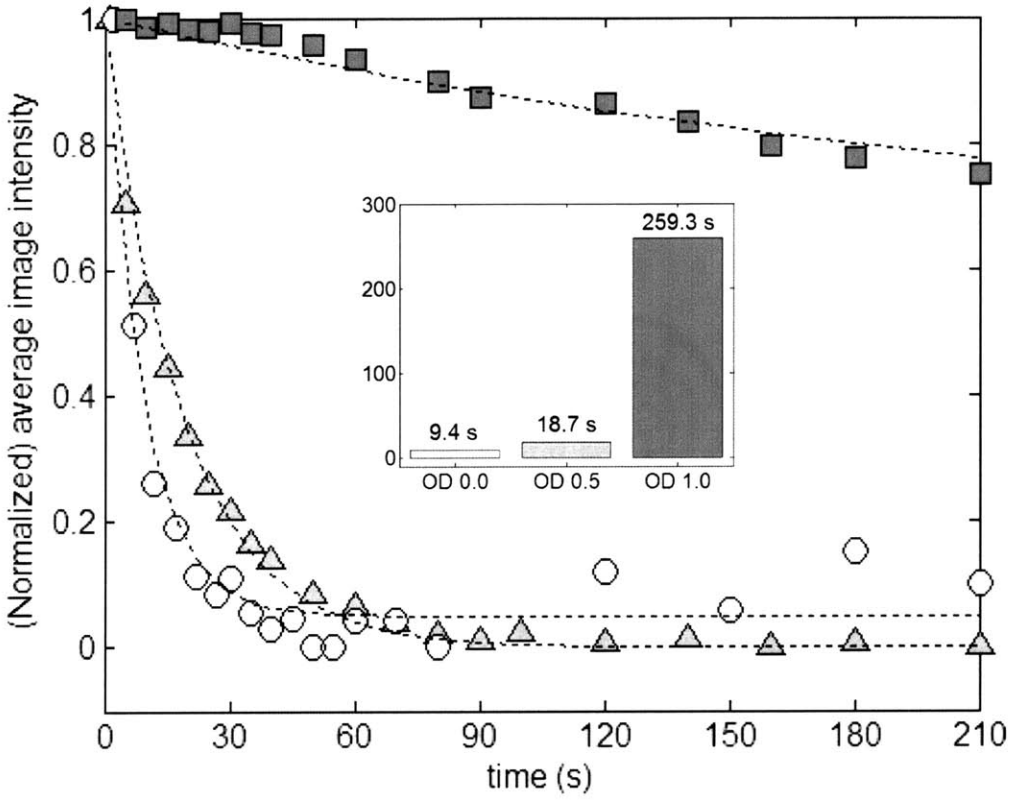

Figure 3-7 Photobleaching of Quantum dots quantified by monitoring average image intensity over time. Sample illuminations of 40 μW/μm2 (OD 0.0, circles and inset's white bar) and 12.5 μW/μm2 (OD 0.5, triangles and light gray bar) caused rapid photobleaching of the QDs (with exponential decay time constants of 9.4 s and 18.7 s, respectively), whereas an excitation level of 4 μW/μm2 (OD 1.0, squares and dark gray bar) significantly limited this decay and allowed for observations windows up to several minutes.

3.3.2. Nanometer Resolution on the Centroid of a Single QD

To demonstrate our ability of achieving nanometer spatial resolution on the location of a single quantum dot, photon flux of individual dots were recorded with a high-sensitivity iCCD. Fig 3-8 shows the typical intensity distribution of a single dot captured in a 100pixels x 100 pixels region on the camera chip. At the center of the spot where the maximum intensity (I_{max}) is 15 photons per pixel, the signal to noise ratio of the image is SNR = $I_{max}/(I_{max} + b^2)^{1/2} \approx 3$ (b is the standard deviation of the background, typically $\sim\sqrt{8}$).

From $\sigma_\mu = \sqrt{\left(\frac{\sigma_0^2}{N} + \frac{a^2/12}{N} + \frac{8\pi\sigma_0^4 b^2}{a^2 N^2}\right)}$, the theoretical error predicted on the centroid determination of this quantum dot is σ_μ = 1.3nm, with N (the overall photons collected from this single dot) being approximately 8.0 x 10^5 and σ_0 = 2 x 113 nm (113 nm being the FWHM of the Gaussian fit).

120 acquisition frames in series revealed the fluctuation of the overall photon flux during each 0.5-s frame time, with an average intensity of 8.8 x 10^5 and standard deviation being 5.4 x 10^3. This variation occured a result of quantum dot blinking, a characteristic process of QDs switching between on and off states. Nonetheless, our method has demonstrated nanometer spatial precision of the localization of a single quantum dot.

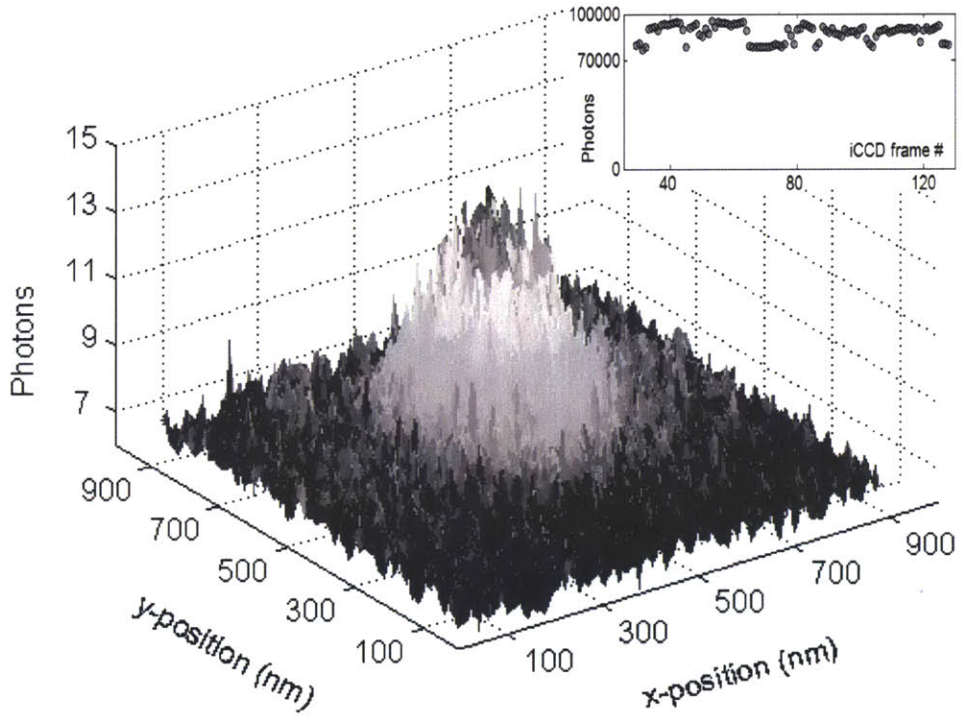

Figure 3-8 Point spread function of a single quantum dot imaged onto a 100 pixels by 100 pixels region with an exposure time of 0.5s. Over one minute recording of the dot (shown as inset) reveals the image intensity fluctuation due to quantum dot blinking.

3.3.3. Tracing QDs Following Incremental Steps of *xy* Piezoelectric Nanopositioner

The piezoelectric stage was moved back and forth in steps, controlled by a custom labview program. The centroid of the quantum dot on the stage was determined using the aforementioned single particle tracking method, and the calculated trajectory was compared to the stage input. One representative step input is shown in Fig 3-9, where T represents the period of the cycle and A defines the amplitude of the imput.

From Fig. 3-10, 100nm steps in x-axis were clearly visualized in both two-dimentional photon intensity image of the single dot and the measured centroid position. For the six images displayed, three on the left side were recorded while the stage was controlled in the half cycle of $+A$, while the rest of the images on the right hand side were recorded during the other half cycle of $-A$. Since each pixel in the image equals to 9nm distance in space, 100nm step increment means approximately 11 pixels shift in the centroid, which is confirmed in both the intensity plot and the trajectory plot in Fig 3-10.

With single dot movement being traced precisely at 100nm amplitude, we further test the accuracy of the method by reducing the step size to 60nm, 40nm, and 20nm. The results following the changes were faily convincing that exact location of a single particle at any given time can be determined with a precision of tens of nanometer. However, the interference of quantum dot blinking at times caused low photon flux during off-state, which could eventually compromise the reliability of the individual data collected during that certain period (Fig 3-11)..

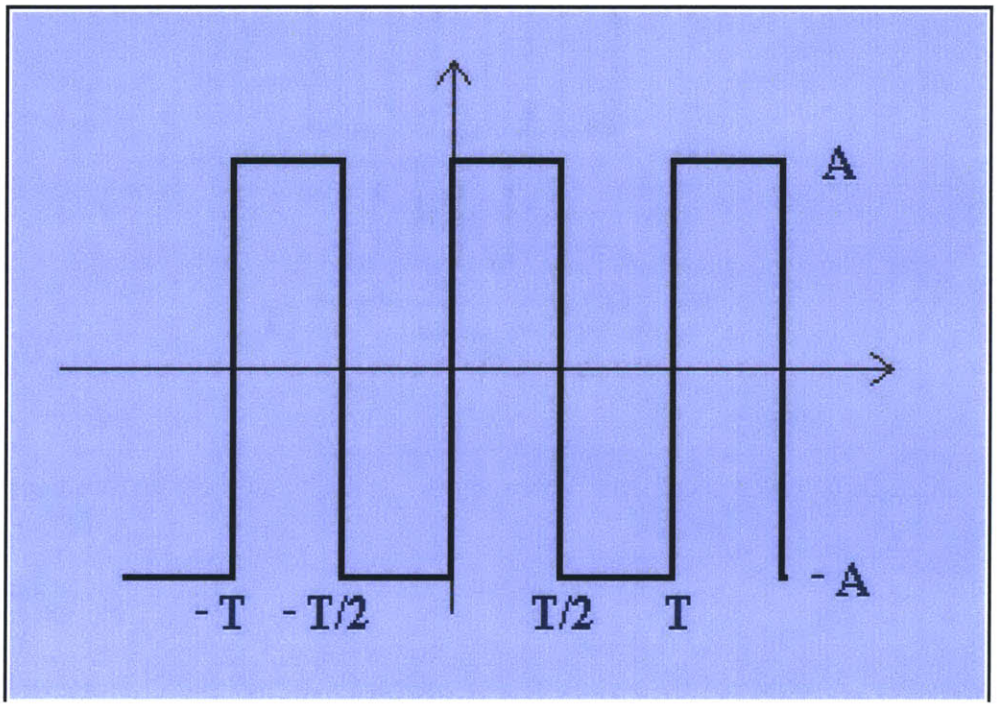

Figure 3-9 Representative step inputs of the stage controlled by the Labview program. T is the period of the step, and A is the amplitude of each displacement.

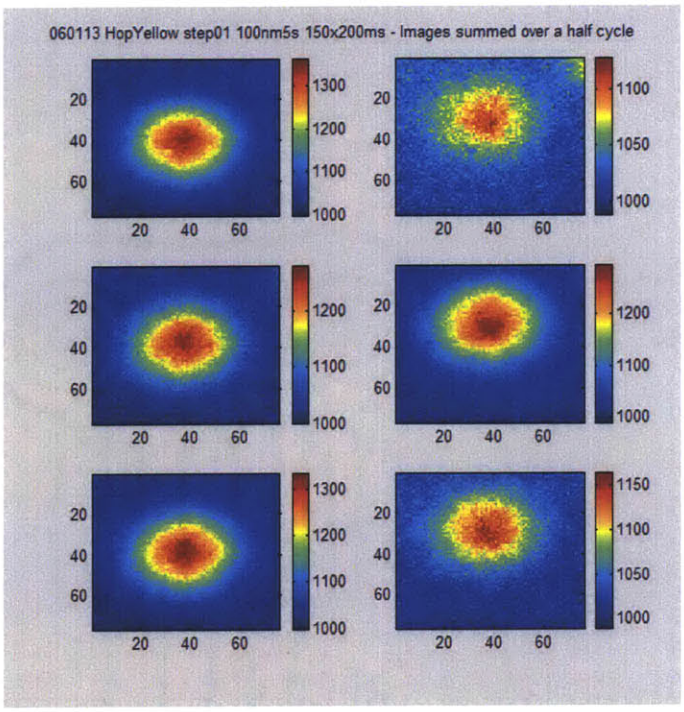

Figure 3-10 Quantum dot trajectory following 100nm steps input from piezoelectric stage in x-axis. Stage was immobilized in y- axis. Top panel reveals the images of a single dot summed over half a cycle, where the alteration of dot location can be clearly distinguished between left and right colums. Bottom panel shows the trajectory of the dot over 150 frames. The unit in Y-axis is in pixel, and 1pixel=9nm.

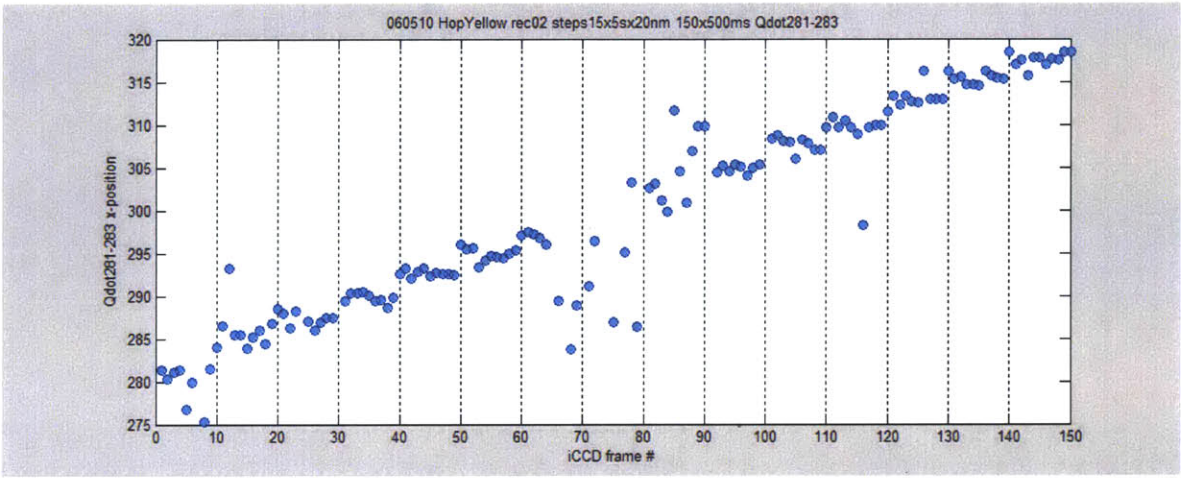

Figure 3-11 Single quantum dot trajectory following 20nm step increments, with 150 frames in total. Stage was translated unidirectionally by each 20nm increments, and kept immobile during each 5s period (10 frames). Blue dots in the trajectory confirmed the tracking method by showing discrete 20nm steps (1 pixel in the y-axis represents 9nm in space). Several data points between frame number 70 to 90 appeared off the intended trajectory due to significant signal reduction during off-state of the dot.

3.3.4. Tracing QDs Following Sinusoidal Oscillation of the Nanopositioner

In the field of biological studies, quite often, the sample is probed under cyclic force application. For instance, in order to study the viscoelastic property of tissue matrices, sinusoidal forces are applied to tissue sample at various levels of frequency and magnitude to obtain the storage modulus and loss modulus of the studied tissue. Similarly, to examine the mechanics of the endothelial glycocalyx in our project, the glycoclayx layer will be subjected to periodic fluid shear stress. Therefore, we shall test the capability of our method to track single dots under sinusoidal oscillation.

To start with, we modifed the Labview program to command the microscope stage to oscillate in x-direction at a given frequency. We first tested sinusoidal oscillation by the stage with an amplitude of 100nm at 0.2Hz and tracked the centroid of a single QD accordingly. At a frame rate of 12.5Hz, the x- position of the dot coincided well with the input, while the y-position was kept still (Fig 3-12).

As we lowered the oscillation amplitude, the overall sinusoidal shape of the input was well retained under both 50nm and 20nm conditions (Fig 3-13 and 3-14), though more irregular data points started to appear as the amplitude kept decreasing.

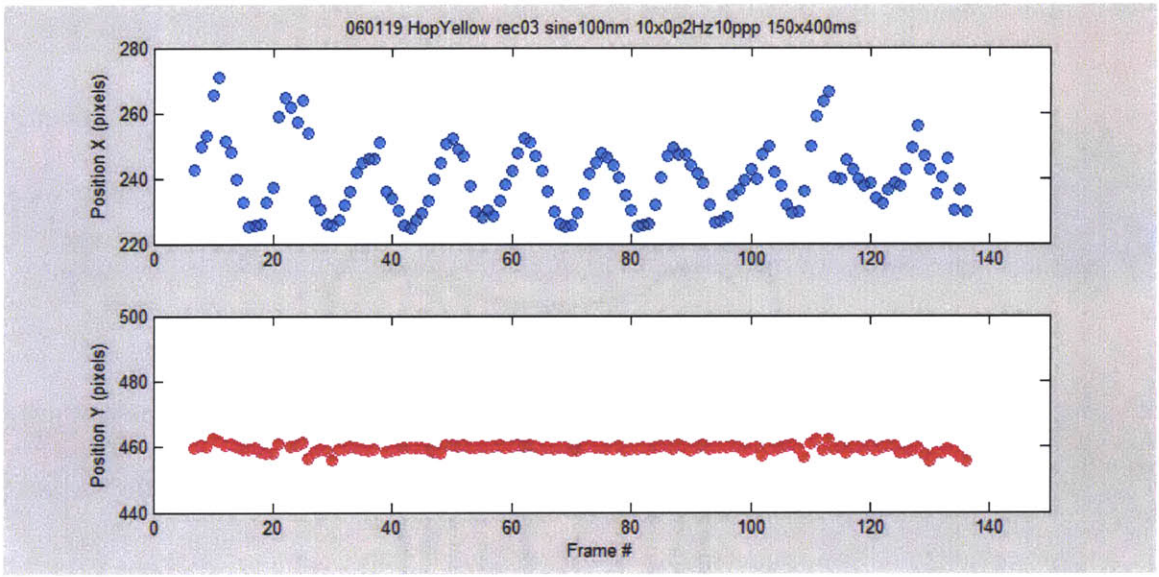

Figure 3-12 Trajectory of a single QD oscillating with an amplitude of 100nm at 0.2Hz. Stage was controlled to oscillate in x-axis with an amplitude of 100nm at 0.2Hz, while kept immobile in y-axis. The blue dots in the upper panel clearly followed the sinusoidal input in x-axis, and the red dots reflected the fixed position in y-axis. Each pixel represents 9nm in space. Camera frame rate is 2.5Hz.

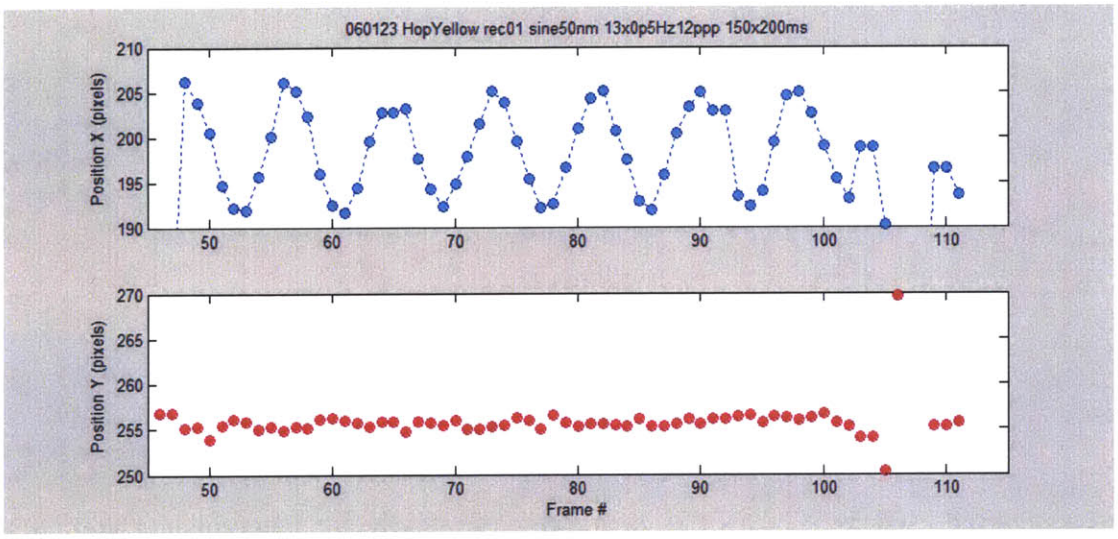

Figure 3-13 Single quantum dot oscillating in x-axis with an amplitude of 50nm at 0.5Hz. Y-position of the stage was kept immobile during the experiment. Each pixel represents 9nm in space. Camera frame rate is 5Hz, thus each cycle contains 10 data points.

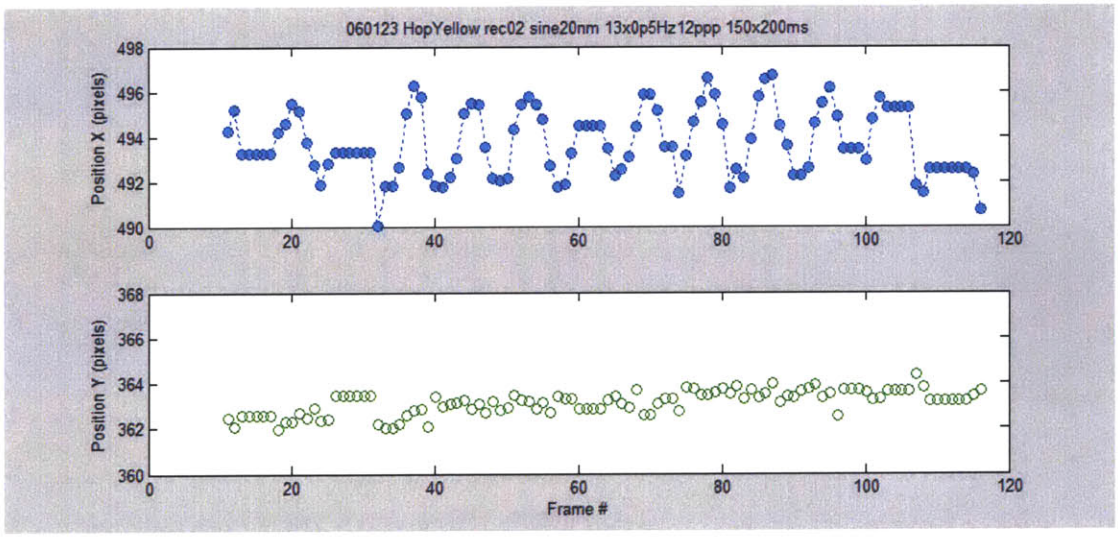

Figure 3-14 Single quantum dot oscillating in x-axis with an amplitude of 20nm at 0.5Hz. Y-position of the stage was kept immobile during the experiment. Each pixel represents 9nm in space. Camera frame rate is 5Hz, thus each cycle contains 10 data points.

3.3.5. Improving Detction Accuracy and Certainty by Applying Discrete Fourier Transform Method

As we explore further to improve our detection accuracy and to minimize the uncertainty of individual data points caused by blinking, we decide to incorporate another piece of useful information ---- *sinusoidal oscillation* ---- into our data analysis.

As Fourier theorem explains, if a series of data points in the time domain are a combination of several sine waves, the Fourier transform of the data will reveal the amplitude and frequency of each sine wave in the frequency domain. The input signal at each individual frequency will appear as a peak along the frequency axis, and the amplitude of the peak is directly related to the magnitude of the sine wave input at this frequency component. When applied to our data, even though the detected trajectory of a single quantum dot does not perfectly follow the periodic input due to noise from different sources, a simple Fourier transform will decompose the data into a set of sine waves at different frequencies. Subsequently, our anticipated data at the given input frequency will stand out in the Fourier domain, and be clearly separated from noise. This method is proved to be very powerful in enhancing our measurement certainty because the noise from individual data points now will have lesser effect in the final determination while the overall trend of the data was taken into account.

One simple example is shown in Fig.3-15. QD sample was oscillated in x-axis with amplitude of 80nm at 0.2Hz while fixed in y-axis. Fourier transform of the data confirmed the periodic motion in x-axis by returning a single peak only at the given input

frequency of 0.2Hz. The fact that the dot was immobilized in y-axis was verified by observing a single peak at DC level (which is at the origin of the frequency axis) along with minimal ruffles appearing in the rest of the frequency domain. Since the useful signal has now been isolated from all the other noise, we need only excerpt the signal at the frequency of our interest and retrieve the corresponding amplitude by applying inverse Fourier transform.

Moreover, as predicted by Parseval's theorem, the peak value p of the power spectrum of the discrete Fourier transform (DFT) of a sine wave, varies as the square of the signal's amplitude, a, times the length of the series, n.

$$p = \sum_{k=0}^{n-1} |X[k]|^2 = \sum_{i=0}^{n-1} |x[i]|^2 \cdot n = a^2 \cdot n$$

where X denotes the DFT of x, and $\Sigma x[i]$ represents the series decomposition of the sine function (37, 101). This correlation between the amplitude a of the input sinusoidal oscillations and the peak height p of the power spectrum of the QD trajectories is validated by Fig. 3-16, where we tested a series of a spanning the range of 8 ~ 200 nm with subnanometer to nanometer increments and obtained the power spectrums respectively. As illustrated by the straight line, fitting $\log_{10}$ (p/n) as a function of $\log_{10}$ (a) returns a linear relationship of slope 2.0786, which confirms the expected quadratic relationship. Furthermore, the method reinstates the ability of our design to resolve single QD trajectory with an accuracy of ~ 4 nm (standard deviation of the spread of the data at a given sine amplitude, and projected onto the x-axis of Fig. 3-16).

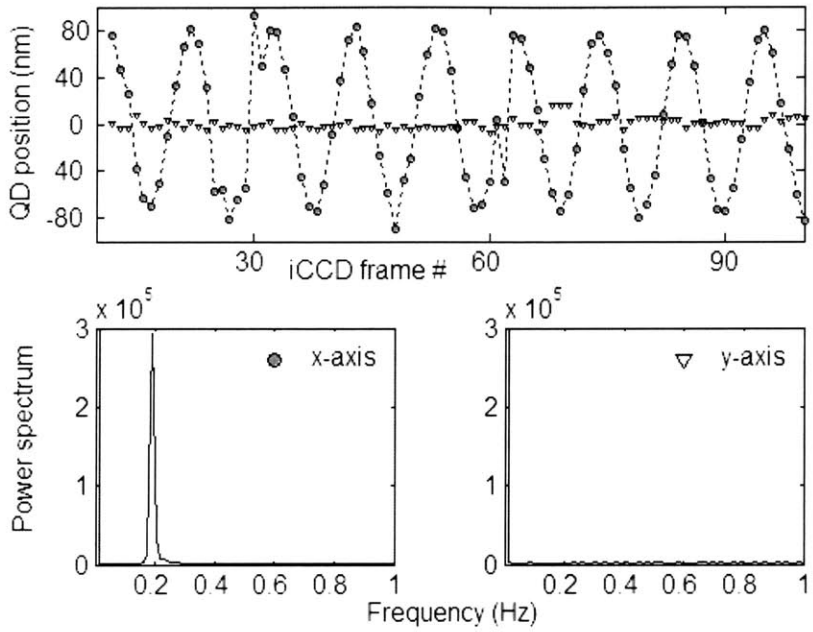

Figure 3-15 Position of a single QD, immobilized onto a high-precision *xy*-stage and translated along its *x*-axis with 0.2-Hz sinusoidal oscillations of amplitude 80 nm *(upper panel).* FFT analysis of the data captures quantitatively both the frequency and the amplitude of the QD motion *(bottom panel).*

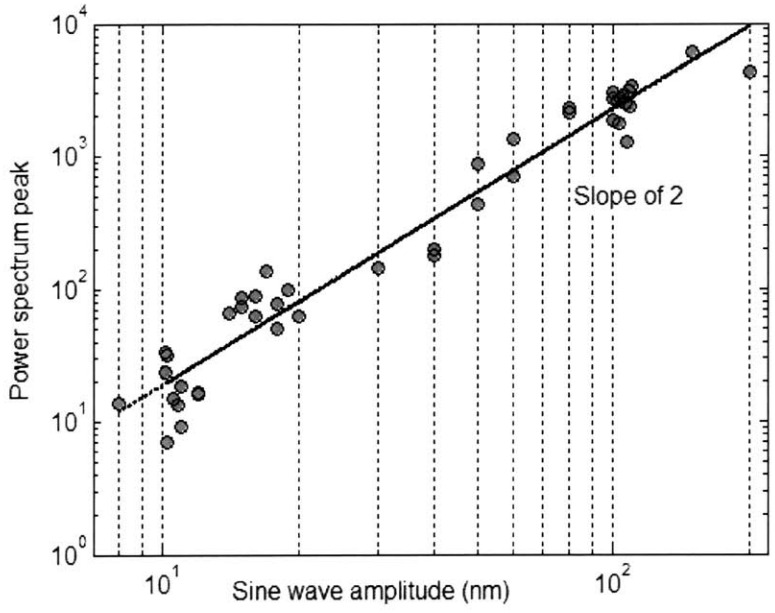

Figure 3-16 The correlation of power spectrum peak attained by Fourier transform versus input sine wave amplitude. A series of test at different levels of sine wave amplitude confirmed the relationship predicted by Parseval's theorem, with data scattering along the line of slope of 2 in a logarithmic plot. Projecting the standard deviation of the data to the x-axis returns the resolution of our detection method ~ 4nm.

3.4. Conclusion and Discussion

In summary, we have described in this chapter an optical imaging method to trace the centroid of individual quantum dots with nanometer spatial precisoin and subsecond temporal resolution. The theoretic prediction of nanometer resolution of this technique was confirmed after several experimental explorations:

1. QD motion induced by 20nm step increments in stage command was conveniently observed.
2. QD motion induced by sinusoidal input commanded at amplitude of 20nm was easily discernible.
3. Fourier transform analysis can improve the detection accuracy on periodic data to approximately 4nm.

Fourier analysis is particularly useful in post-imaging data analysis as to minimize the random noise caused largely by quantum dot blinking. The whole length of the data is processed to return the amplitude of QD periodic motion so that the uncertainty introduced by individual data points will not significantly affect the ultimate spatial resolution. Since cyclic force application is not uncommon in bioassays, our method of single quantum dot tracking in conjuction with Fourier analysis could benefit a number of biological studies without exorbitant hardware investment.

Chapter 4. Three-dimensional Mapping of the Endothelial Glycocalyx Layer

4.1. Introduction

Since the idea of the endothelium covered by a thick surface coating of glycocalyx gained increasing acknowledgements in the field, direct measurement of layer properties have become exceedingly desirable yet the task still remained challenging. One of the important properties of the layer is the geometry, in particular, the thickness of the glycocalyx. Many researchers have now realized that the presence of the glyoccalyx layer may well change our way of understanding the mechanisms behind a number of physilogical and pathological events in the vascular system, such as red blood cell passaging, white blood cell intrusion and endothelial mecahnotransduction. Therefore, theoretical models developed to describe those phenomena all necessitate an accurate measurement of glycocalyx dimension and its mechanical properties that conventional methods have to date not been able to provide.

In this chapter, we present an innovative imaging method to visualize the glycocalyx layer in living cells, and have obtained the first direct measurement of the layer thickness in cultured endothelial cells. This method will also provide opportunies to resolve structures with nanometer resolution in all three dimensions in space, with enormous potential for broad application in biomedical science.

The projects in the following two chapaters were completed as collaboration with Hao Huang, and a large portion of the data shown below was collected using the optical

facility in Prof. Moungi Bawendi's spectroscopy lab in the Department of Biological Engineering.

4.1.1. Existing Techniques to Measure Glycocalyx Thickness

Since the concept of an extracellular layer of membrane-bound substances lining on the vascular walls was originated more than 50 years ago, interest in the area of studying the structure and composition of this surface layer has grown extensively. A substantial amount of effort has been devoted to improving the visualization techniques in resolving the complex structure *in vivo*, yet measuring the thickness of the glycocalyx still remains a challenge. Several techniques that have been developed to detect the endothelial glycocalyx are summarized below.

Visualization of the glycocalyx by electron microscopy

Observation of the glycocalyx by electron microscopy largely depends on the fixation and visualization methods that were used at the time. In 1966, a ruthenium red staining method by Luft (85) revealed a fluffy and irregularly shaped endothelial surface layer with a thichness in the range of 20 nm. However, this could not present the full scope of the structure as the preparation procedure and possibly the dye itself may have caused substantial and irreversible damages to such a fragile structure with high water content. Ruthenium red for instance, may alter the glycocalyx geometry by changing the electrostatic interactions between the macromolecules in the structure. Furthermore, the relatively large molecular size of the dye may not have allowed its full access to the entire glycocalyx region(109).

In an effort to circumvent those limitations, Haldenby et al(66) used a smaller molecule, alcian blue, to improve layer visuliazation as well as to provide additional information on charge density and anionic groups in the studied region. This method found a glycocalyx of about 60nm thick in the rabbit bthoracic aorta, compared with a previously reported 20nm thickness measured with ruthenium red(8). This technique however, may still compromise the integrity of the layer as the washing procedures probably removed plasma proteins that were originally attached to the membrane-bound glycoproteins(8).

To reduce the effect of perfusion fixation on the delicate structure of the endothelial glycocalyx, fluorocarbons were used as non-aqueous vehicles for the fixative osmium tetroxide(137). The glycocalyx layers detected by this method were typically on the order of 60 to 110 nm thick in arterioles and capillaries. A recent study by Rostgaard et al. (123) reported endocapillary glycocalyx measured as 50~100 nm thick. At the same time, filamentous plugs composed of 20 to 40 filaments with a length of ~ 350nm were located on the surface of endothelial fenestrae.

In a word, improvement in the electron microscopy staining techniques indicated a layer of ~100nm thick existing on the endothelial surface. Nevertheless, as the nature of electron microscopy requires harsh preservation and fixation process that would inevitably result in damaging the fragile structure of high water content, observations from those studies may well underestimate the extent of glycocalyx presence in nature.

Visualization of the glycocalyx by intravital microscopy

Quantitative intravital studies of the microcirculation since the late 1970s have indicated the existence of a glycocalyx layer much thicker than observed by electron microscopy. While Klitzman et al. (77) were studying the red cell volume fraction (tube haematocrit) in capillaries of hamster cremaster muscle, unexpected low values of tube haematocrit were obtained in animals when compared to theortical prediction of haematocrit from a glass tube. This discrepancy however, could be explained by assuming "a slow-moving plasma layer on the order of 1 μm thick" responsible for excluding red blood cell from the layer (77). Later reported by Pries et al (110, 111), the dependence of flow resistance on vessel diameter measured in capillaries did not agree with that observed in glass tubes. And the inconsistency led to a hypothesized stationary plasma layer on the endothelial surface, with a thickness of about 1.1 μm. This indirect evidence inspired direct measurement of a fluorescently labeled vascular wall (22, 66, 130), but the fluorescence intensity assessment often failed to yield a precise representation of the geometrical features due to optical limitation of the method. As explained by Gretz et al.(65), intravital measurements in complex optical environment may introduce unexpected errors from several factors including refractive index mismatch and improper focus and edge selection. In addition, disparity between fluorescence microscopy and light microscopy measurements on the same subject seemed to be common in such an application.

For direct visualization of the layer using intravital microscopy, Vink and Duling(157) adopted an alternative approach to label the flowing plasma instead of staining the glycocalyx layer and thus measured plasma exclusion in the blood vessel. When

compared to the anatomical diameter of the capillary, the fluorescent plasma volume was constantly smaller due to dye exclusion by the endothelial surface layer. In addition, as white blood cells fully occupied the anatomic capillary cross section, red blood cells were continually excluded from the near wall region and occupied a significantly smaller volume in the blood vessel (~1.2 μm lesser in diameter). This study provided the first visual demonstration of a countinous glycocalyx layer with a thickness about 0.4 to 0.5 μm decorating on the endothelial surface.

Visualization of the glycocalyx by confocal fluorescence microscopy

In a recent study to investigate the role of glycocalyx in mechanotransduction, Thi *et al.* (149) used confocal microscopy to visualize the immunostained glycocalyx layer in cultured endothelial cells. The layer was clearly observed on the endothelial apical membrane, and enzyme degradation lead to a substantial reduction of membrane-bound glycocalyx appearance. Having confirmed the presence and localization of glycocalyx on cultured endothelial cells, this method yet failed to provide an accurate estimate of glycocalyx thickness due to optical limitation. Even with the assistance of deconvolution technique, confocal microscopy mearly reaches a resolution of about 200nm and can hardly overcome the long-standing roadblock in optical imaging ---- the diffraction limit of light.

In a quick recap, studies in the past have shown an endothelial surface layer existing in both *in vivo* and *in vitro* systems. However, resolving the structure and detailed geometry for the intact glycocalyx layer remaines nontrivial. Meanwhile, partly due to variances in

experimental approach and targeted system, the thickness measurements from several detecting methods did not result in a perfect agreement. Instead, the greatest discrepancy between data could be one order of magnitude away from each other. This challenge calls for a novel imaging system capable of resolving the glycocalyx structure with a spatial resolution superior than conventional optical imaging, yet most importantly, without compromising the integrity of the layer components in such a system. Therefore, we have chosen to apply off-focus imaging mechanism for this purpose to achieve a detailed structure and geometric information of this layer to the extent that would otherwise be impossible to achieve.

4.1.2. Off-focus Imaging Method to Extract Z-depth Information

Due to the diffraction nature of light, the resolution achieved by conventional optical microscopy is often limited to ~250nm, about half the wavelength of light. This means even confocal microscopy can not easily resolve structures with dimensions on the order of 250nm. However, when it comes to locating individual particles in space, single particle tracking technique can help determine the centroid of small particles with near nanometer precision in the image plane. With the assistance of quantum dots as fluorescent tracers, single particle tracking has become an invaluable tool in biological science and has found broad application in areas such as studying transport process in cells, working cycles of molecular motors, membrane receptor/ligand interactions and etc.(9, 37, 97, 139, 150, 160)

As explained in Chapter 3, the x- and y- position in the image plane of a single dot can be determined with nano-resolution by simply applying 2D Gaussian fitting to the point spread function. To extract the z- position of the particle at the same time however, turns out to be nontrivial. The diffraction pattern of a single dot has long been known related to the axial distance (z-depth) of the dot to the objective focal plane, yet the exact calculation of the pattern requires parameters of internal optics that are generally not accessible. Thus it seems impractical to use the theoretic calculation as a reference basis to predict the z-position of single particle.

In one pioneer paper by Speidel *et al.* (140), the authors determined the relationship between the diffraction pattern and z-depth experimentally using off-focus imaging, and thus described a method to track sigle particles with nanometer resolution in all three dimensions in space. In brief, the in-focus image of a point like object is a bright spot with a diameter of $\sim 1.22\lambda/NA$. As the objective focal plane moves away from the particle, complex ring patterns start to form and the ring size increases with the defocus distance. Thus, the z-depth information of the particle is encoded in the ring intensity profile, and one can obtain this z-dependency of ring pattern experimentally. The authors have found that the outermost ring radius in the image scaled linearly with the defocus distance when the object is more than 0.5 μm away from the focal plane, and therefore the ring size becomes a direct indicator of the z- position of the object.

This off-focus method turns out to be extremely powerful in tracking 3D position of individual particles, and researchers have applied the technique not only in tracer

experiments in biology(163), but as well as in microfluidics to measure the flow profile in fluid channels(86) and rheology (105). While the method allows one to follow the three-dimensional migration of objects without switching focal plane, it also provides the possibility of differentiating the z-positions of two dots that are closer than the diffraction limit. For instance, when scanning two dots certain distance away in the z- direction (say ~50nm), the size difference in the off-focus ring of each dot will indicate their exact distance to each other. Along with the help of quantum dots to label different targets through immunostaining, the spatial positions of various proteins in one sample can now be determined to an accuracy that no conventional imaging method could have achieved in living cells.

Based on this off-focus method, we developed an imaging systme to measure the relative positions of several different molecules in space, and applied the principle to obtain the first *in vitro* direct estimate of the glycocalyx thickness.

4.2. Materials and Methods

4.2.1. Optical Setup

4.2.1.1. Optical path

Off-focus imaging was performed on a customized optical bench in Prof. Moungi Bawendi's Spectroscopy lab. However, this method is easily applicable in any commercially available epifluoresence microscope setup in conjuction with a high-sensitivity CCD camera.

A laser beam of 514nm (Innova 70C, Coherent) was collimated through a defocusing lense and a 100X oil immersion objective (Nikon Plan Fluor) to illuminate a circular area with a diameter of ~40μm of the sample positioned on an xyz- piesoelectric nanopositioning stage (Queensgate, T-orquay, U.K). The photons emitted by the QDs in the excitation volume was reflected by a beam splitter to pass through an imaging lens, a notch filter and detected by an image intensified camera of 12-bit resolution and 512 pixels x 512 pixels (iCCD camera, Pentamax, Princeton Instrument). To avoid substantial photobleaching, the typical laser intensity applied in our experiments was tuned in the range of 0.2~1 mW. The results are shown in Fig. 4.1.

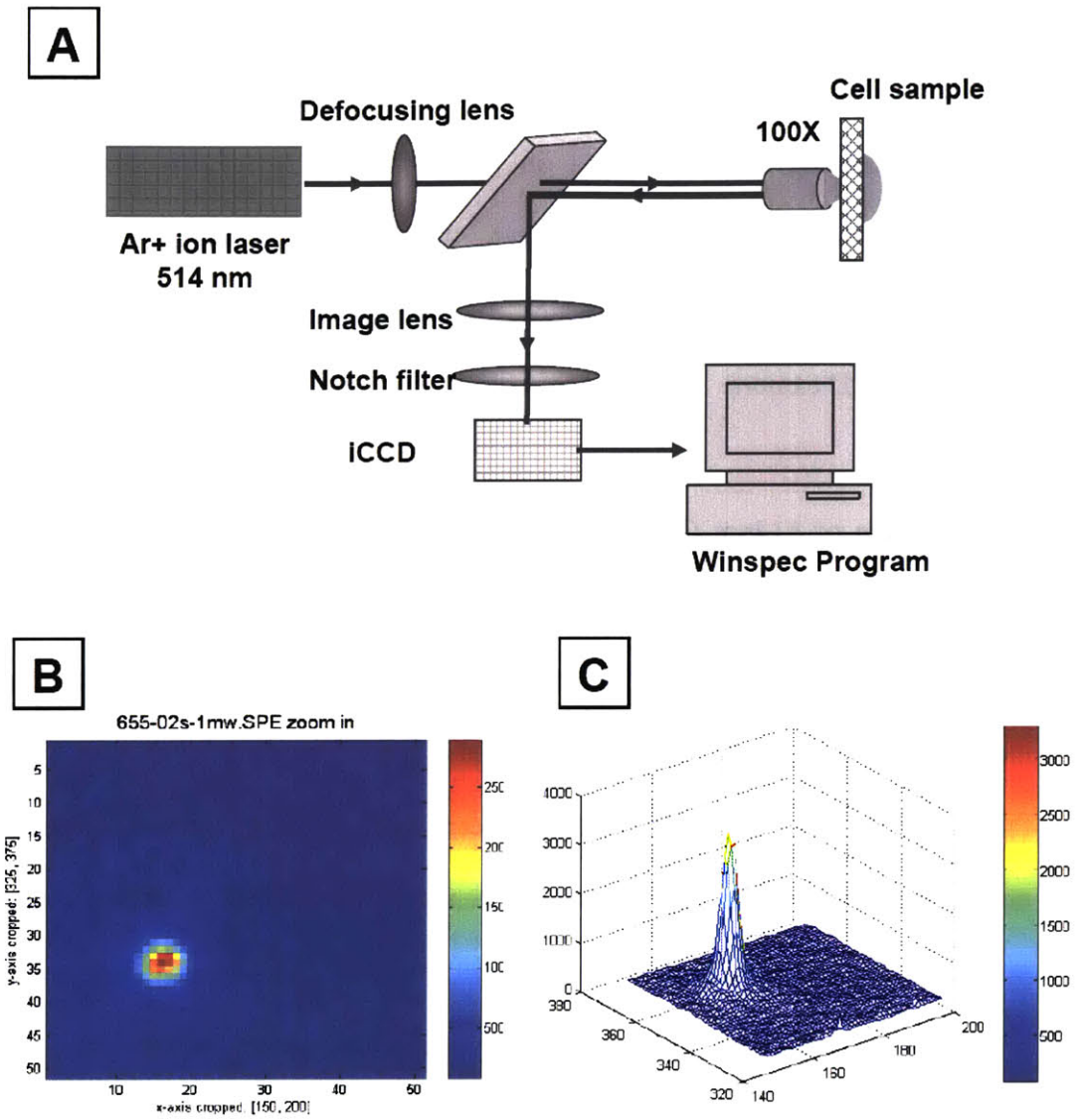

Figure 4-1 Customized optical path for off-focus imaging (A). Three-dimensional photon intensity plot (C) of a single dot captured by the camera (B) indicates high signal to noise ratio (~ 30).

4.2.1.2. Chamber Adaptor

To ensure sample position accuracy, a customized chamber adaptor made from Aluminum was designed to stabilize the cell sample (prepared in flow chambers) onto the nanopositioner. For future reference, the flow chamber geometry and the adapter design are shown in Fig 4-2 and Fig 4-3 respectively.

4.2.1.3. Pixel Size Calibraton

To determine the spatial resolution of our optical system, precision Ronchi ruling glass slides were employed in the calibration tests. In order to provide flexibility in the current setup, we have prepared image lenses of different sizes for need-based use. The calibrated pixel size for the following three conditions is:

1 pixel = 50 nm without image lens

1 pixel = 70 nm with the use of a 200 cm image lens

1 pixel = 90 nm with the use of a 50 cm image lens

Our entire project indeed benefited from this otpcial flexibility, as a 90 nm/pixel setup works the best for off-focus imaging experiment while a 50 nm/pixel setup suits better for flow tracing experiments.

When nanopositioner was in use, sample was translated in x-, y-, z- axises via a controller interface. Nanometer precision of the stage was verified using Ronchi Ruling calibration as well.

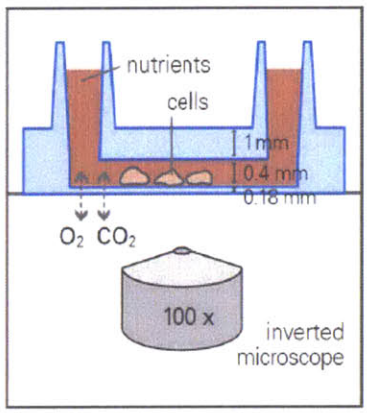

µslide I

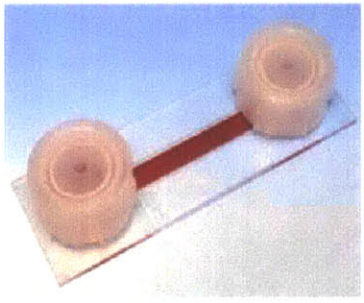

recommended volume per reservoir	600 µl
number of channels	1
volume of the channel	100 µl
height of the channel	0.4 mm
length of the channel	50 mm
width of the channel	5 mm
growth area	2.5 cm^2
bottom matches coverslip	No. 1.5

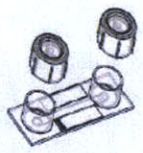

µslide IV

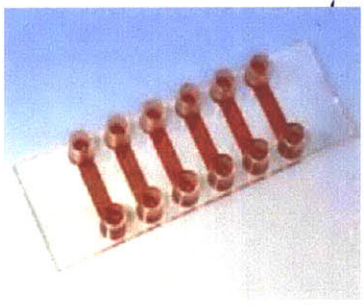

adapters	female Luer
recommended volume per reservoir	60 µl
number of channels	6
volume of each channel	30 µl
height of channels	0.4 mm
length of channels	17 mm
width of channels	3.8 mm
growth area per channel	0.6 cm^2
bottom matches coverslip	No. 1.5

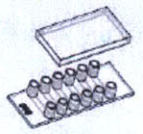

Figure 4-2 Flow chamber geometry (ibidi Inc). Cells were carefully placed in either *µslideI* or *µslideIV* to reach confluence before optical imaging. Source: www.ibidi.com

a) Side view

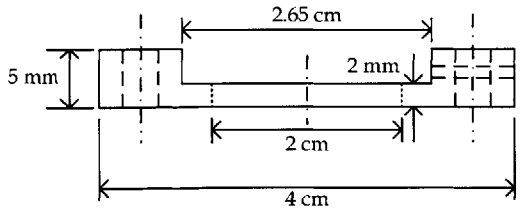

b) Top view

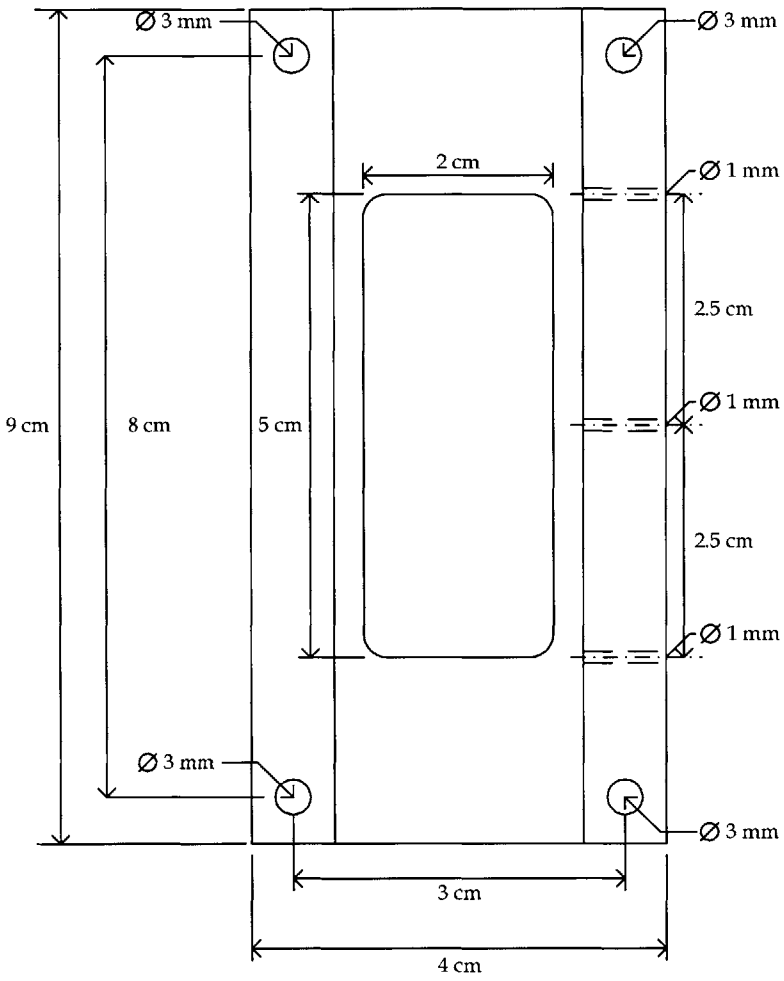

Figure 4-3 Drawing of the adaptor geometry, showing four M3 screws (at the corners of a 3cm X 8cm rectangle) used to stabilize the adaptor to the nanopositioner along with three inserted M1 screws to fix the flow chamber onto the adaptor.

4.2.2. Quantum Dot Selection and Filter Design

Accurate mapping of the endothelial surface layer requires a careful selection of labeling targets, including proper cell reference points in addition to protein constituents in the glycocalyx. We consider the following three candidates as for labeling purposes:

1) Heparan sulfate glycosaminoglycans (HSGAG) to represent the glycocalyx layer;
2) Platelet/endothelial cell adhesion molecule 1 (PECAM-1, same as CD31) to represent endothelila membrane; and
3) Intracellular vesicles to fill the cytoplasm.

Antibodies commercially available against the first two protein targets were later conjugated to quantum dots for multiplex imaging. As illustrated in Fig.4-4, streptavidin-QD655 (quantum dot of emission wavelength at 655nm coupled with streptavidin) was attached to biotinlated HSPG primary antibody as to mark the glycocalyx; mouse IgG-QD605 (quantum dot of emission wavelength at 605nm coupled with IgG molecule) was attached to IgG PECAM-1 primary antibody as to visualize membrane-bound PECAM-1; and non-functional water soluable QD565 was endocytosed by cell to help picture cell body.

As a result of the QD's narrow emission band (FWHM typically < 30nm), signals from quantum dots of the three colors can be collected individually without noticeable spectral interference. Hence, we selected filter "K", "L", "F" for collecting photons from QD565, QD605 and QD 655 respectively. Filter specs shown in Figure 4-5 confirmed successful signal separation. In particular, we chose QD655 and QD605 of close wavelengths as to minimize chromatic aberration of the two during the imaging process.

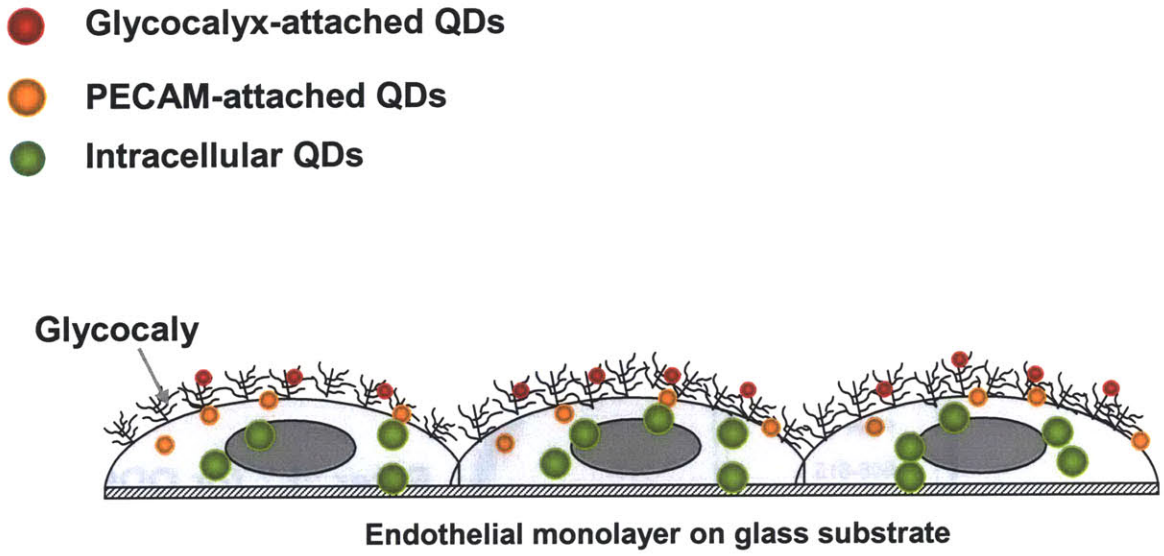

Figure 4-4 Illustation of quantum dot conjugation to endothelial cells, labeling intracellular vesicles (QD565), membrane PECAM-1 (QD605), and glycocalyx (QD655). QD565 were added in the growth medium to be uptaken inside by cells through endocytocis; QD605-IgG particles adhered to antibody attached PECAM molecules through IgG interaction; and QD655-biotin recognized streptavidin-coated heparan sulfate glycosaminoglycan antibody.

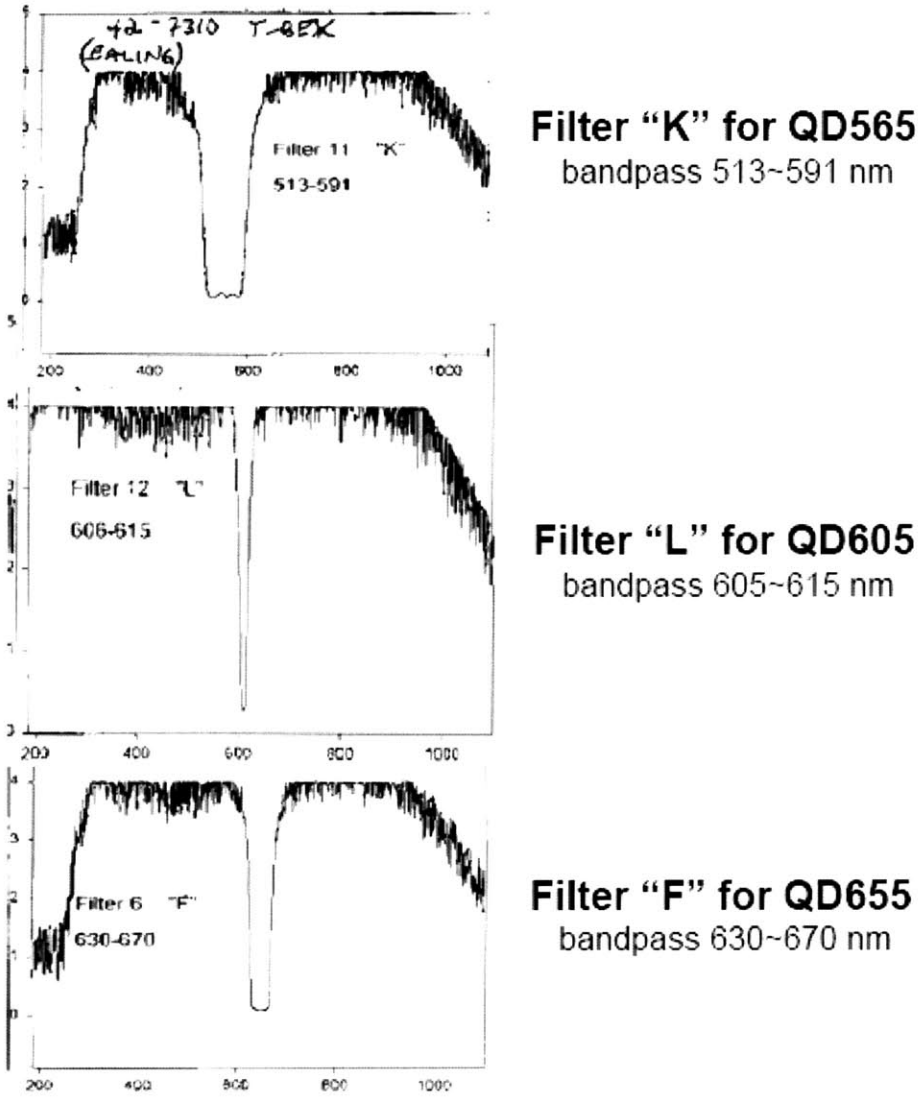

Figure 4-5 Notch filter selection for quantum dots of threedifferent colors. Each plot shows the bandpass for either K, L or F filter.

4.2.3. Cell Sample Preparation

Primary bovine aortic endothelial cells (BAEC-77, passage 10-15) are cultured in DMEM supplemented with 10% fetal calf serum, 1% L-glutamine, and 1% penicillin-streptomycin. Before seeding, cell culture flasks and glass slides are coated with 0.2% gelatin at room temperature. Ibidi microfluidic chambers are coated with 100μg/ml fibronectin to promote cell attachment in micro-enviroment. Cell cultures are kept in a humidified incubator maintained at 37^0C, with 5% CO_2 and 95% air.

After cell monolayers reach confluence in ibidi chamber, three layers of QDs were attached to the cell as follows. Cells were incubated in culture medium with 5nM QD565 (Prof Bawendi's lab) for 15min at 37^0C to allow QD565 to be incorporated into intracellular vesicles via endocytosis. After five quick rinses in DPBS to remove excessive QDs in solution, cells were chilled on ice for 10min and blocked with 2% goat serum and 2% BSA for 20min to reduce nonspecific background staining. To label the glycocalyx layer, cells were incubated with 5 μg/mL heparan sulfate biotin antibody (US Biological) for 20 min and washed three times with DPBS. Cells were subsequently incubated with 2nM streptavidin-QD655 (Invitrogen) for 15 min, and later washed with DPBS. After completing glycocalyx staining, cells were washed three times and incubated with 30μg/ml PECAM-1 IgG antibody (AbD Serotec) for 15min. Finally, IgG QD605 (Invitrogen) were added in a final concentration of 2nM to finish PECAM-1 staining. The cell labeling procedure was performed on ice so as to limit QD endocytosis during the incubation procedure, with the only exception of QD565. Prepared cell

samples were transfered onto the nanopositioner and imaged right afterwards at room temperature.

4.2.4. Data Acquisition and Analysis

Images collected on the iCCD were captured using the WINspec data acquisition software and saved as SPE files. Individual cells were first identified using QD565 signals, and thus images for PECAM-QD and Glycocalyx-QD on the same cell could be recorded later by switching filters. Once a cell has been properly selected, the nanopositioner was locked in x- and y- postion and adjusted only in z-axis to shift its focal plane. Changes in z-axis were typically controlled in 0.25μm or 0.5μm steps. Ring patterns affected by the small adjustments in z-distabnce were recorded for data analysis (Fig 4-6).

A custom-written Matlab code was developed to fit the center spot of the off-focus ring to a two-dimensional (2D) Gaussian function to determine the centroid of the quantum dot in the *xy* plane. Next, 360 lines were radially projected from the center to collect the signal intensity against radial position along each line for a full 360^0 radial integration, which was later fitted to a one-dimensional (1D) multi-Gaussian function to find the center of the outermost ring. The relative z-distance between different dots can thus be calculated by referring the outermost ring radius to the calibration curve (r_0 *vs.* z).

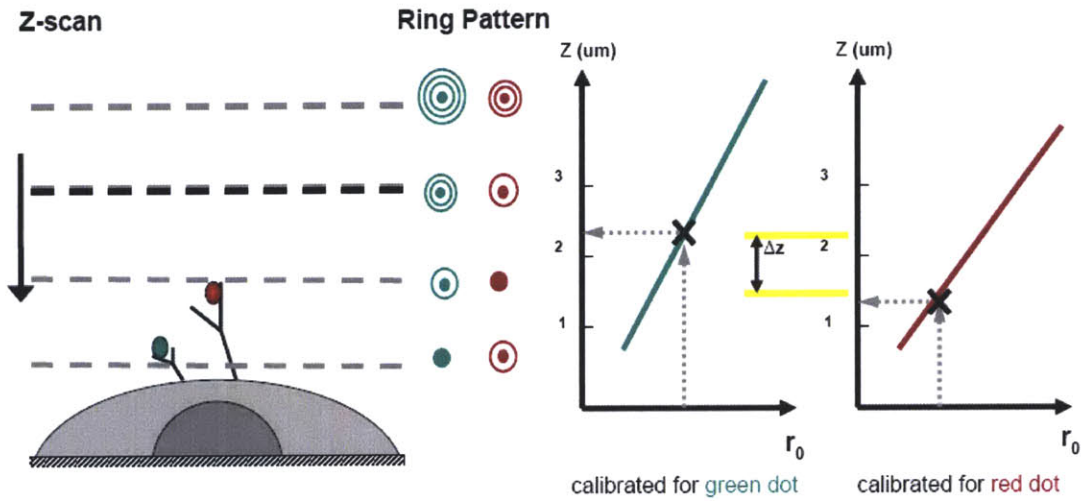

Figure 4-6 Method to assert the relative z-distance between two dots. Sample was scanned on successive focal planes and the size of the outermost ring for each dot was calculated by Gaussian fitting and refered to the calibration curve to determine their z-position.

4.2.5. Theoretical Principles

A quantum dot nanoparticle can be considered as a point source of fluorescence in optical microscopy. The emitted fluorescent light from the point source forms a real image on the CCD image plane via the microscope objective. The image of an in-focus point source is a well-known Airy disc, with the center spot having a diameter of ~ 1.22λ/NA, where λ is the imaging wavelength and NA is the numerical aperture of the objective. When the point source is located out of the focal plane, the image will then be expanded into a considerably larger diffraction pattern (59, 100).

In order to generate a diffraction pattern with clear interference fringes, the emitted fluorescent light shoud be coherent or partially coherent. Quantum dots used in this study have narrow emission spectrums, with typical FWHM < 30nm. Therefore, for QD655 (emission wavelength at 655nm), the coherence length estimated by $L = \frac{\lambda^2}{\Delta\lambda}$ is about 21λ, which is more than sufficient to observe clear fringes in the diffraction pattern.

One commonly used diffraction model to predict the intensity distribution of the diffraction pattern was developed by Gibson and Lanni(59). It presented a comprehensive form of point spread function (PSF) based on Kirchhoff's diffraction integral formula. The three-dimensional intensity distribution is expressed as a function of r (radial position on the image plane) and z (defocus depth):

$$I(r,z) = \left| C \int_0^1 J_0\left(\frac{2\pi}{\lambda} \cdot \frac{NA}{\sqrt{M^2 - NA^2}} \rho \cdot r\right) \cdot \exp[iW(z,\rho)] \cdot \rho d\rho \right|^2$$

, where C is a constant, λ is the emission wavelength, NA is the numerical aperture of the objective lens, M is the

magnification of the microscope system, and ρ is the dimensionaless radial coordinate of the objective aperture (59, 86, 105). The phase aberration function, $W(z,\rho)$, is a product of the wave number $\frac{2\pi}{\lambda}$ and optical path length difference (OPD) which can be further written as $OPD = n_i z\sqrt{1-(\frac{NA\rho}{n_i})^2}$, where n_i denotes the refractive index of the immersion oil. When the particle is in focus at z=0, this formular is then reduced to the planar Airy function $I(r,0) = \left| C\int_0^1 J_0(\frac{2\pi}{\lambda}\cdot\frac{NA}{\sqrt{M^2-NA^2}}\rho\cdot r)]\cdot\rho d\rho \right|^2$.

4.3. Results

4.3.1. Observing Off-focus Ring Pattern

To demonstrate the capability of the imaging system to visualize off-focus ring pattern, we spin-coated a thin layer of quantum dots onto a glass slide for imaging tests. Figure 4-7 shows the image patterns of a single quantum dot captured by the iCCD camera while adjusting the sample only in z-axis. When the quantum dots were in focus, the imaging pattern for each individual dot appeared as a single circular spot. As the scanning plane moved away from the nanoparticles, complex ring intensity patterns were formed. The outermost ring radius increased with distance from the in-focus plane as shown in the figure.

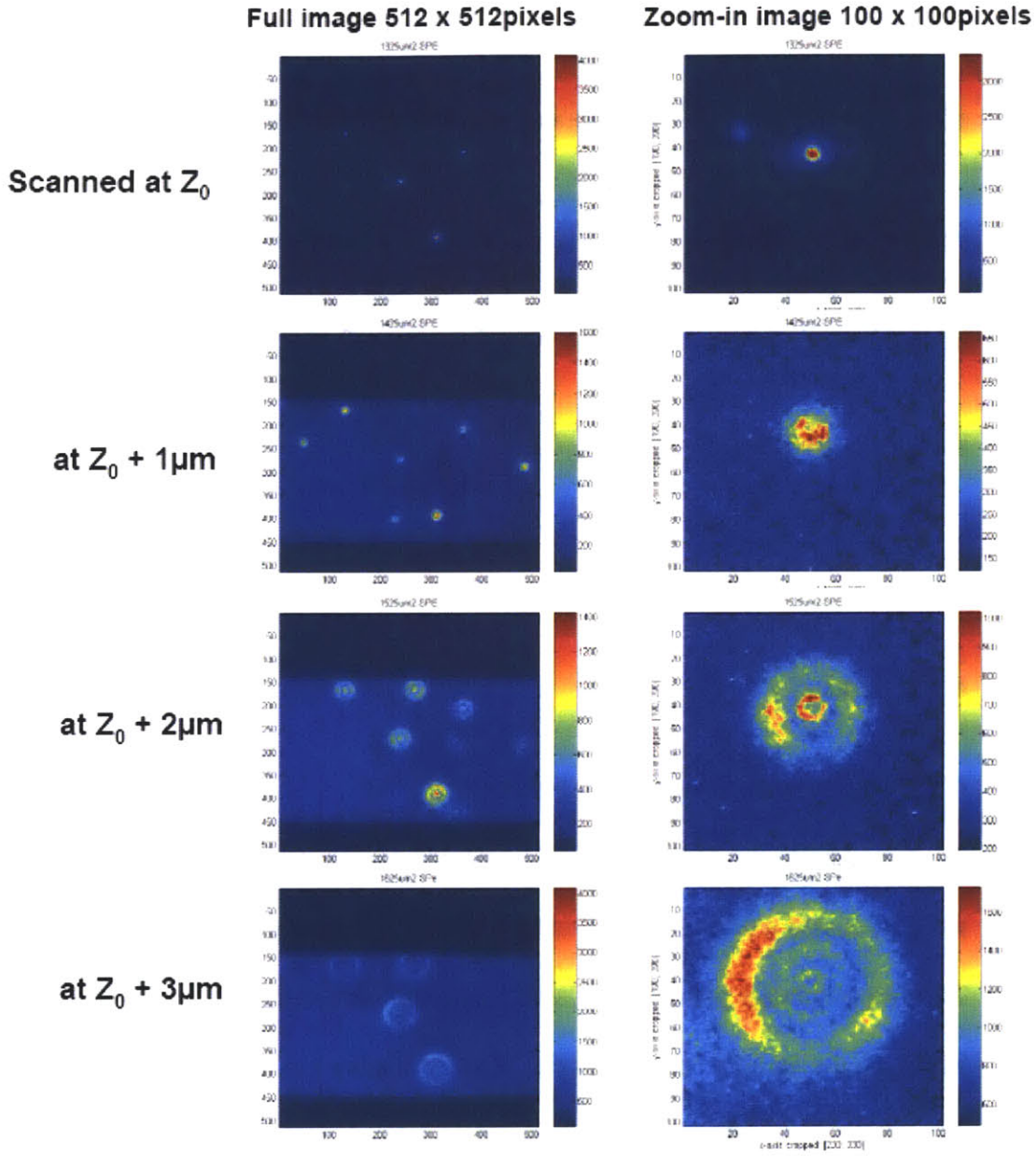

Figure 4-7 Representative images of single quantum dots recorded at different z-plane. Left colum contains the full images of several dots in a 512x512 pixels image frame; right colum contains the zoom-in image of the same quantum dot in a 100 pixels x100 pixels image frame.

To ascertain the radius of the outermost ring, which indicates the z-postion of the particle, we fit the intensity profile to multi-Gaussian function as in Fig 4-8. First, we find the center of the pattern by fitting the innermost bright spot to a two-dimensional Gaussian function. Once the centroid is determined (x=168, y=207 in this case), 360 lines are radially projected from the center to integrate the signal intensity for a full circle against each distance along the radial axis. Next, the radial integrated intensity is fitted to a combination of multi-Gaussian functions (summation of two Gaussians in this case) and the center of the farthest Gaussian intensity ring is returned as the outermost ring size.

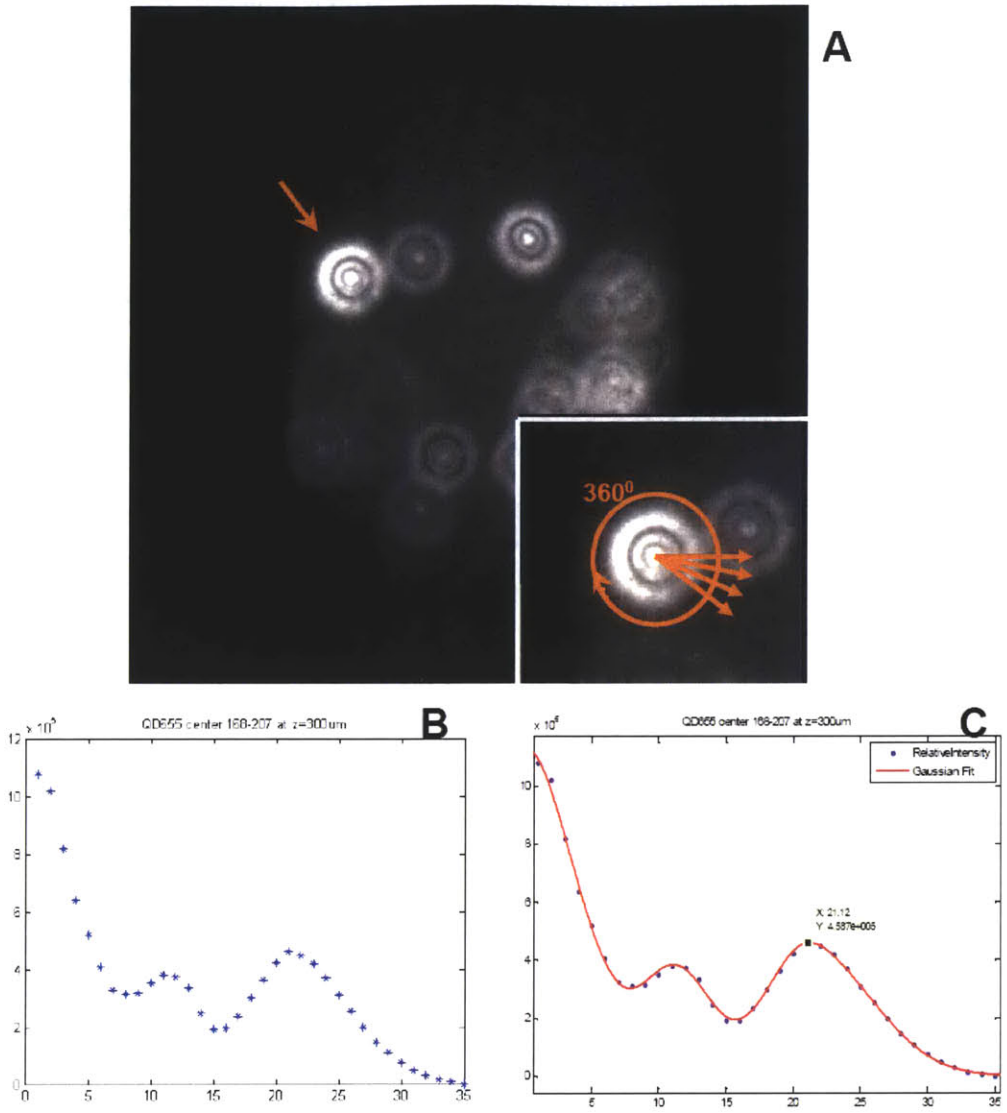

Figure 4-8 Gaussian fitting method to determine the outermost ring radius. Once a dot (insert of A) was chosen from a camera image of several defocused dots (A), the radial integration of photon intensity from the center of the dot is plotted agaist the radial distance (blue in B), and fitted to a multi-Gaussian function to calculate the center of the outermost ring (fitting result shown as red curve in C).

4.3.2. Curve Calibration for Quantum Dots of Different Colors

To calibrate the relationship between the defocus distance and the outermost ring radius, first, we spincoated quantum dots on a glass coverslip for imaging. The coverslip was previous tested using AFM to ensure the surface roughness (~2nm variation) was negligible to our measurements. During the image acquisition, we shifted the image plane from in-focus position to ~ 4μm away from focus by every 0.25 μm and measured the ring size with respect to z-distance. Finally we fit all the z versus r data to a linear equation to determine the slope, $\Delta z/\Delta r$. The accuracy of this method was indicated by the standard deviation of the measured ring sizes of several dots at the same image plane. Due to the wavelength-dependency of the diffraction pattern, we processed the calibration for dots of different colors individually, as shown in Fig 4.9. When two dots observed in the same image plane differs by 1pixel in size, it is thus inferred that they are separated by 114nm along the z-direction. Spatial resolution determined from the calibration measurement was ~ 15nm, by calculating the standard deviation of observed ring sizes of a group of dots placed in the same z-plane.

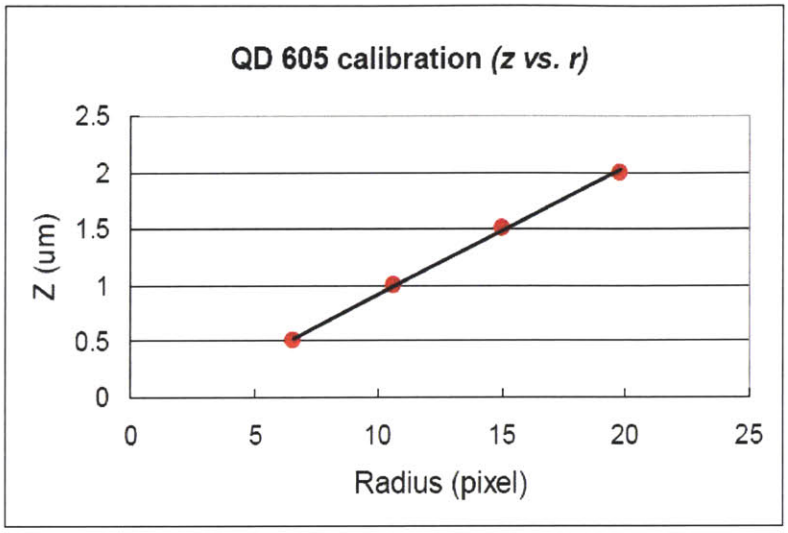

$QD605$

$z=z_0+0.1139\,r$

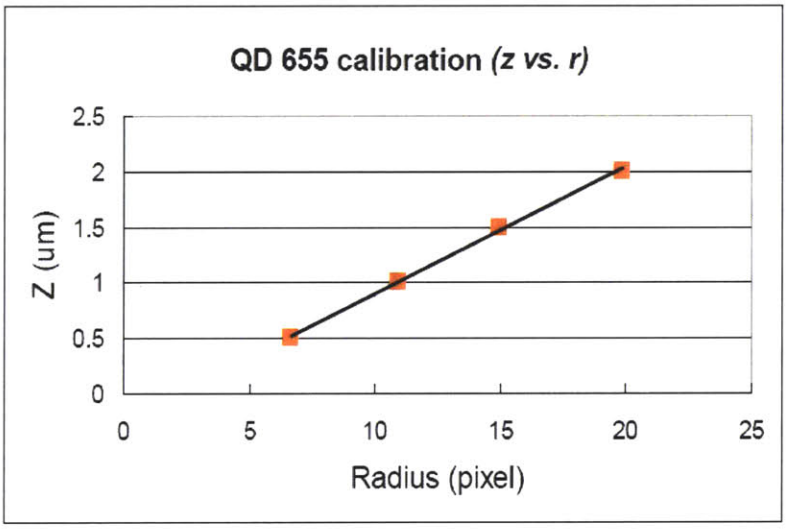

$QD655$

$z=z_0+0.1145\,r$

Figure 4-9 Defocused calibration for QD605 and QD655 respectively. By linear approximation, 1 pixel change in the size of off-focus ring (r) indicates ~114nm difference in off-focus distance (z).

4.3.3. Three-dimensional Mapping of the Glycocalyx Layer

Following proper staining procedure described earlier in the chapter, the endothelial monolayer is marked with three layers of quantum dots: QD565 (green) inside vesicles, QD605 (orange) attached to PECAM-1, and QD655 (red) attached to glycocalyx.

Once the cell sample is fixed onto the microscope stage, filter "K" is used to pass exclusively the photons from QD565 to locate individual cells. The nanopositioner is then placed to a reference position so that the focal plane of the objective falls in the medium right outside the cell body, where the camera starts to capture images at a frame rate of 5Hz. As the scanning plane moves toward and through the cell by every 0.5 μm step, ring patterns of the same dots change accordingly and dots at deeper z-positions start to appear. Fig.4-10 gives an example of approximately ten QD565-containing vesicles detected in one cell as the objective scanned through the cell body. After completing the collection of QD565 signal, we switched to filter "L" and "F" to repete the same procedure with QD605 and QD655.

When comparing the images of the three dots scanned at the same z-plane (Fig.4-11), the ring patterns indicate vesicles (QD565) as being the furthest from the scanning plane while the glycocalyx (QD655) as being the closest to the scanning plane. The relative postions of the three layers from the data in fact, corroborates with the cell structure physiologically, with the glycocalyx being the outermost layer and the vesicles being the intracellular parts.

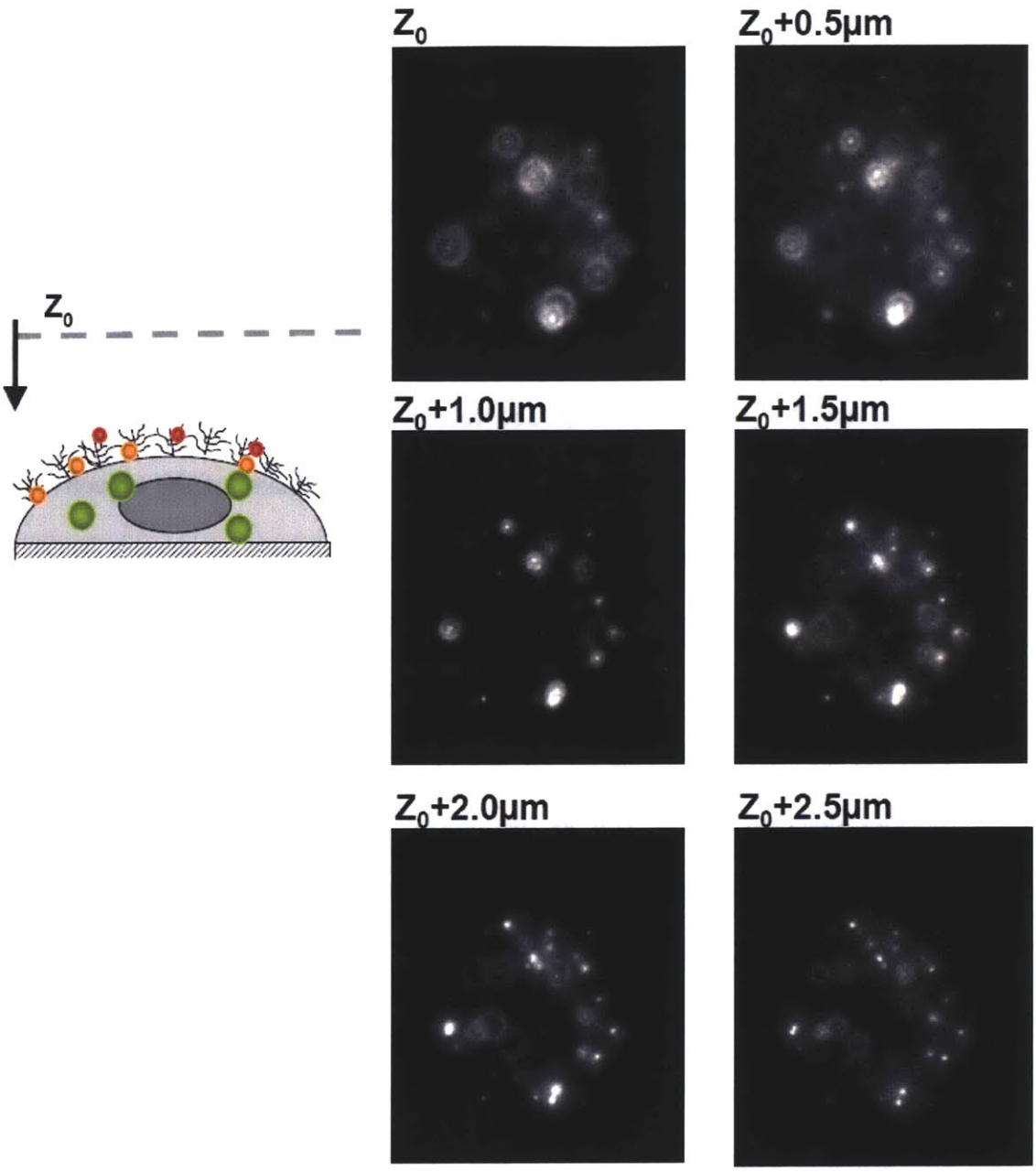

Figure 4-10 Off-focus images of intracellular QD565 at the scanning planes. As the objective focus moves closer to the cell body, the ring patterns of various intracellular vesicles in different positions gradually changes.

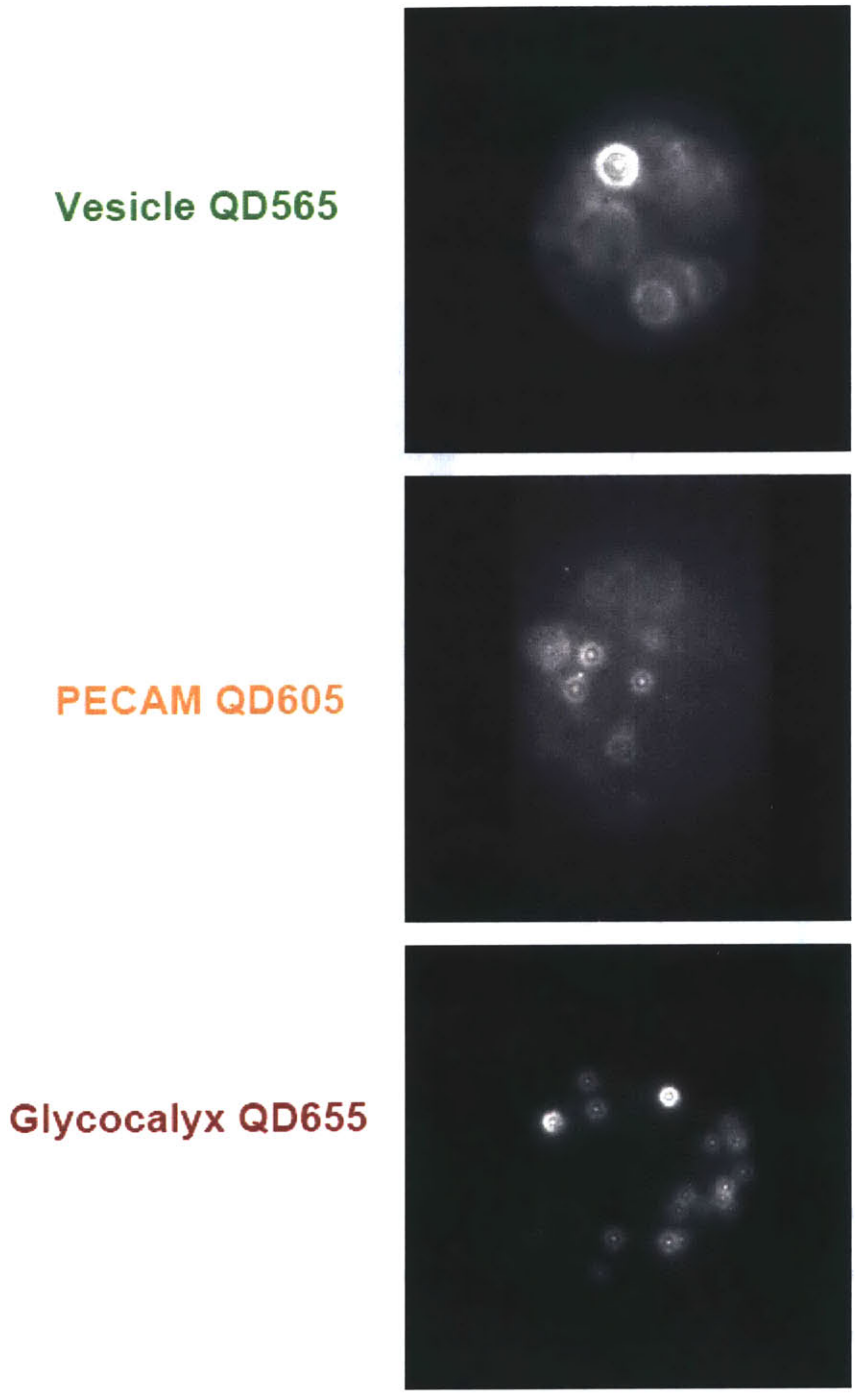

Figure 4-11 Representative images of QD565, QD605 and QD655 recorded at the same scanning plane. As dots of different colors appeared with different ring sizes scanning at the same z-plane, the relative position of the three layer (vesicle, PECAM and glycocalyx) inferred from the data corrobates with common perception of their physical location.

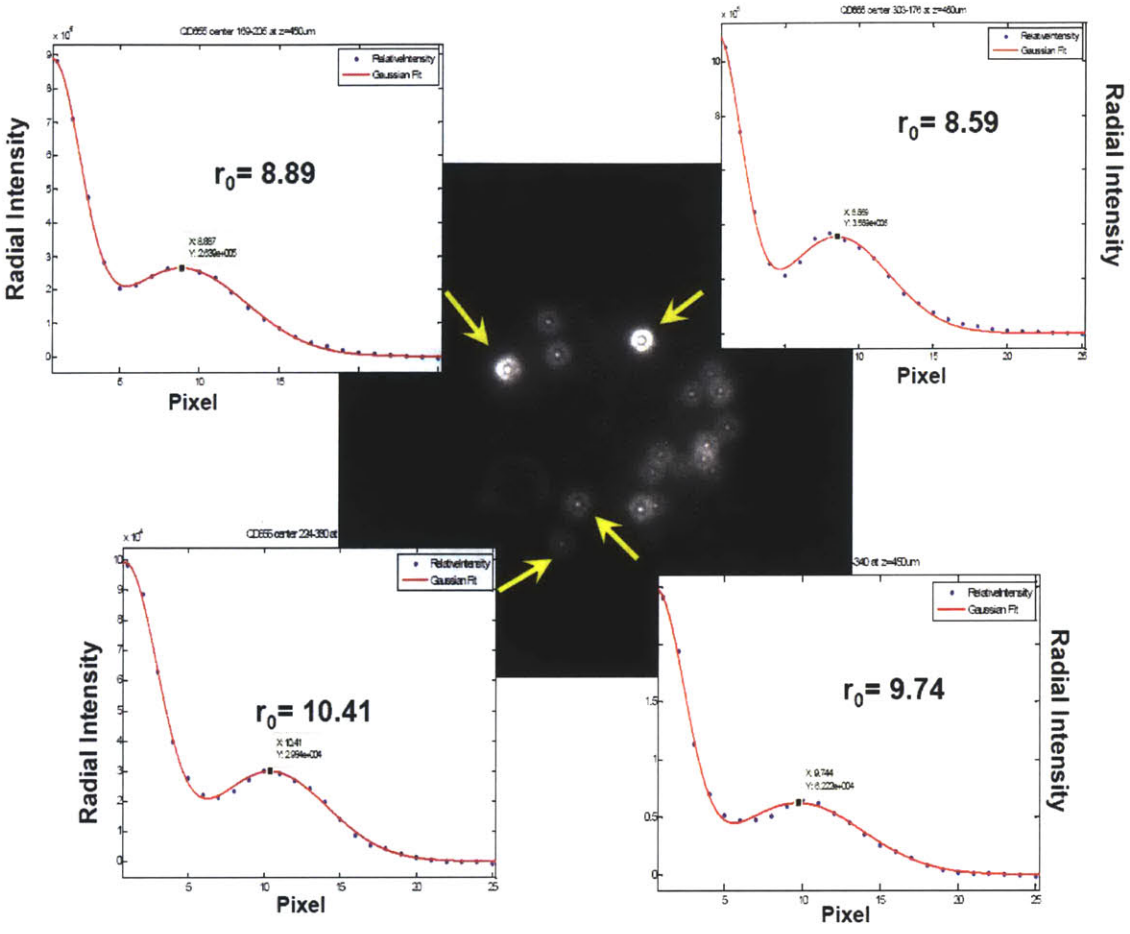

Figure 4-12 Illustration of obtaining outermost ring radius from off-focus rings for individual dots. As for each dot in the image frame, radial integration projected from the center of the spot yields the photon intensity profile with respect to the distance away from the center, which is later fitted into multi-Gaussian function to determine the outermost ring radius.

Fig 4-12 illustrates the typical procedure to obtain the size of each off-focus ring, used later to calculate the z-positon of the same dot. First, a proper ring spot is selected (typically SNR > 3), and the centroid of the ring pattern is found by fitting the central bright spot to a two-dimensional Gaussian, using the method described in Chapter 3. Once the centroid is determined, 360 lines were radially projected from the center to collect the signal intensity against radial position along each line for a full circle radial integration. Then, the radial intensity profile is fitted to a one-dimensional multi-Gaussian function to acquire the center of the outermost ring. In certain cases when two ring patterns moderately overlap with each other, the radial integration can be adjusted accordingly by subtracting the overlapping regions from the overall intensity.

After processing all the data for QD565, QD605 and QD655, the precise location of each dot can be determined by obtaining x-, y- position from Gaussian fitting of the central spot, and z- postion from referring the ring radius to the calibration curve. Thus, we have located within one cell, seven vesicle-QDs, eight PECAM-QDs, and thirteen glycocalyx-QDs, as listed in table 4-1.

A total of 28 dots, including all three colors are placed in a 3D space based on their relative positions to each other (Fig 4-13). The maximum z-distance between vesicle-dots and glycocalyx-dots is roughly 3.5 μm, on the same order of known cell body height. Inserting a reference plane at z = 4μm (transparent blue) near the PECAM-dots (yellow marker), the glycocalyx-dots (red marker) are distinguished generally on the extracellular side of the membrane.

Vesicles QD565

Number	X (μm)	Y (μm)	Z (μm)
1	8.05	3.74	2.62
2	6.88	10.58	1.46
3	13.27	16.34	1.57
4	12.28	4.01	1.48
5	15.52	4.28	1.71
6	5.26	9.23	1.71
7	9.58	14.27	1

PECAM QD605

Number	X (μm)	Y (μm)	Z (μm)
1	10.39	8.15	4.27
2	3.64	9.23	3.93
3	5.17	5.54	4.16
4	11.56	4.64	4.24
5	8.59	13.1	4.21
6	12.19	0.59	4.1
7	10.21	3.74	4.15
8	1.48	15.53	3.93

Glycocalyx QD655

Number	X (μm)	Y (μm)	Z (μm)
1	1.21	5.45	4.51
2	13.27	2.84	4.55
3	7.51	17.6	4.42
4	6.16	21.2	4.34
5	5.71	4.19	4.45
6	4.81	1.31	4.48
7	17.77	7.7	4.58
8	13.18	18.05	4.47
9	14.62	17.78	4.51
10	20.92	10.67	4.47
11	19.39	5.9	4.55
12	14.26	14.72	4.46
13	14.35	21.2	4.22

Table 4-1 X-,y-,z- positions of vesicle-QDs, PECAM-QDs and Glycocalyx-QDs within one cell.

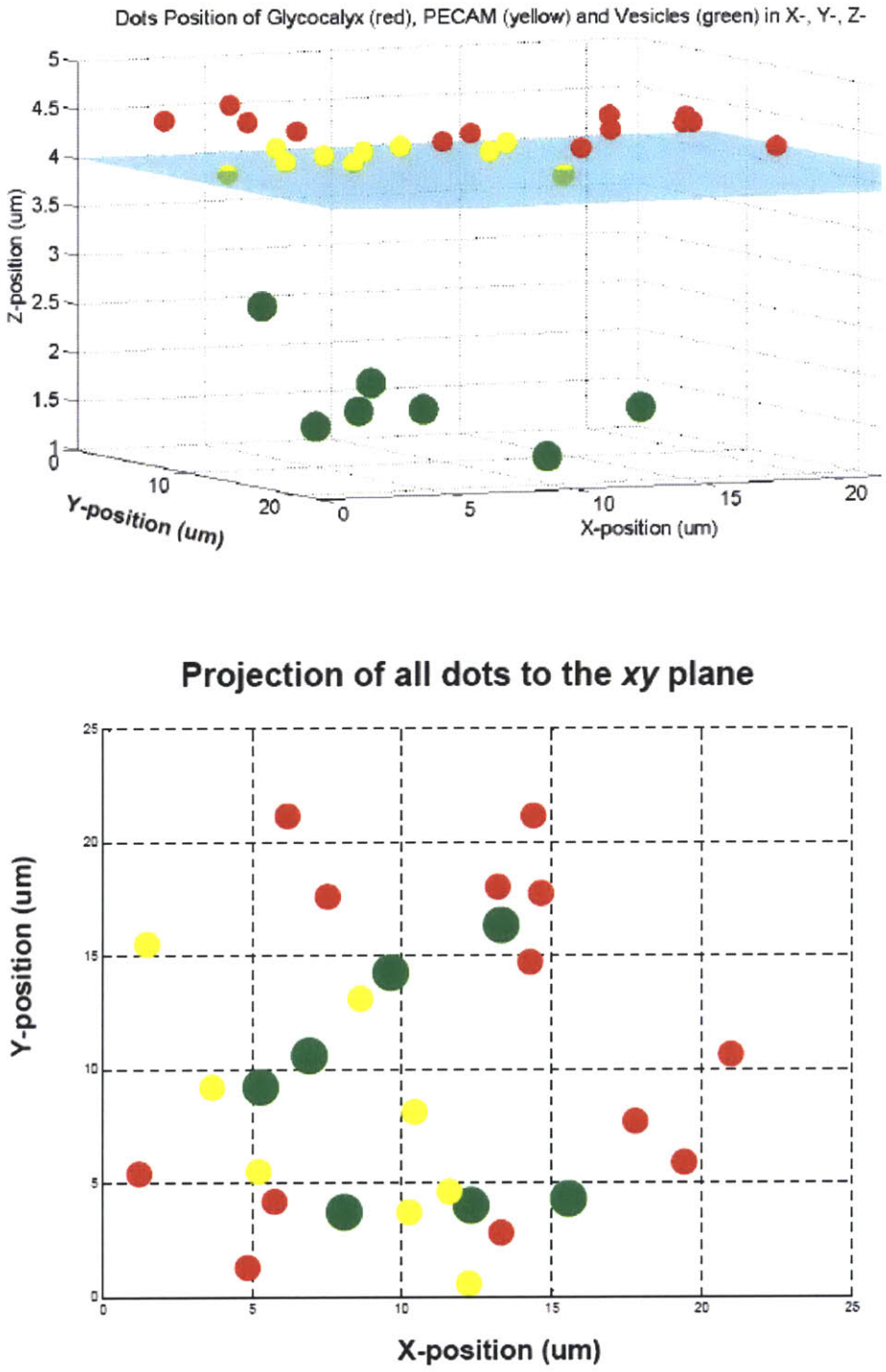

Figure 4-13 Three-dimensional mapping of all dots in space (top), including vesicles (green), PECAM (yellow), and glycocalyx (red). A reference plane set at z=4um indicates the relative position of PECAM and glycocalyx. X-y- plane projection of the same dots gives additional view of their spatial relationship.

4.3.4. Estimating Glycocalyx Thickness

With the glycocalyx layer mapped in a 3D space, the thickness of the layer can be estimated by comparing the relative distance between the glycocalyx-dots and the membrane. Here are two possible approaches for this purpose.

Method 1: Direct readout of thickness from Glycocalyx-PECAM pair

Once we have several PECAM-dots covering the cell membrane, the glycocalyx thickness can be obtained directly from the z-difference of a glycocalyx-PECAM pair, given the membrane waviness between the two dots in the pair is negligible. A close examination of all the dots in space (Fig 4-14) reveals one glycocalyx-PECAM pair that satisfies the criteria. The PECAM-dot in this pair is located at x=5.17 μm, y=5.54 μm and z= 4.16 μm; while the glycocalyx-dot is located at x=5.71 μm, y=4.19 μm and z= 4.45μm. Assuming the PECAM-dot is close enough to the glycocalyx-dot in x-y- plane, PECAM-dot can thus be used as the membrane reference, and the z-difference between the two dots, Δz=0.29 μm, is an estimate of the glycocalyx thickness at this location.

Providing a simple and direct readout of the thickness, this method however, appears inefficient when only one such dot pair can be found on a cell sample with more than 20 dots in total. The majority of the dots end up useless in terms of finding glycocalyx thickness. Therefore, we need to improve the method so that the spatial information of all available dots can contribute to the result.

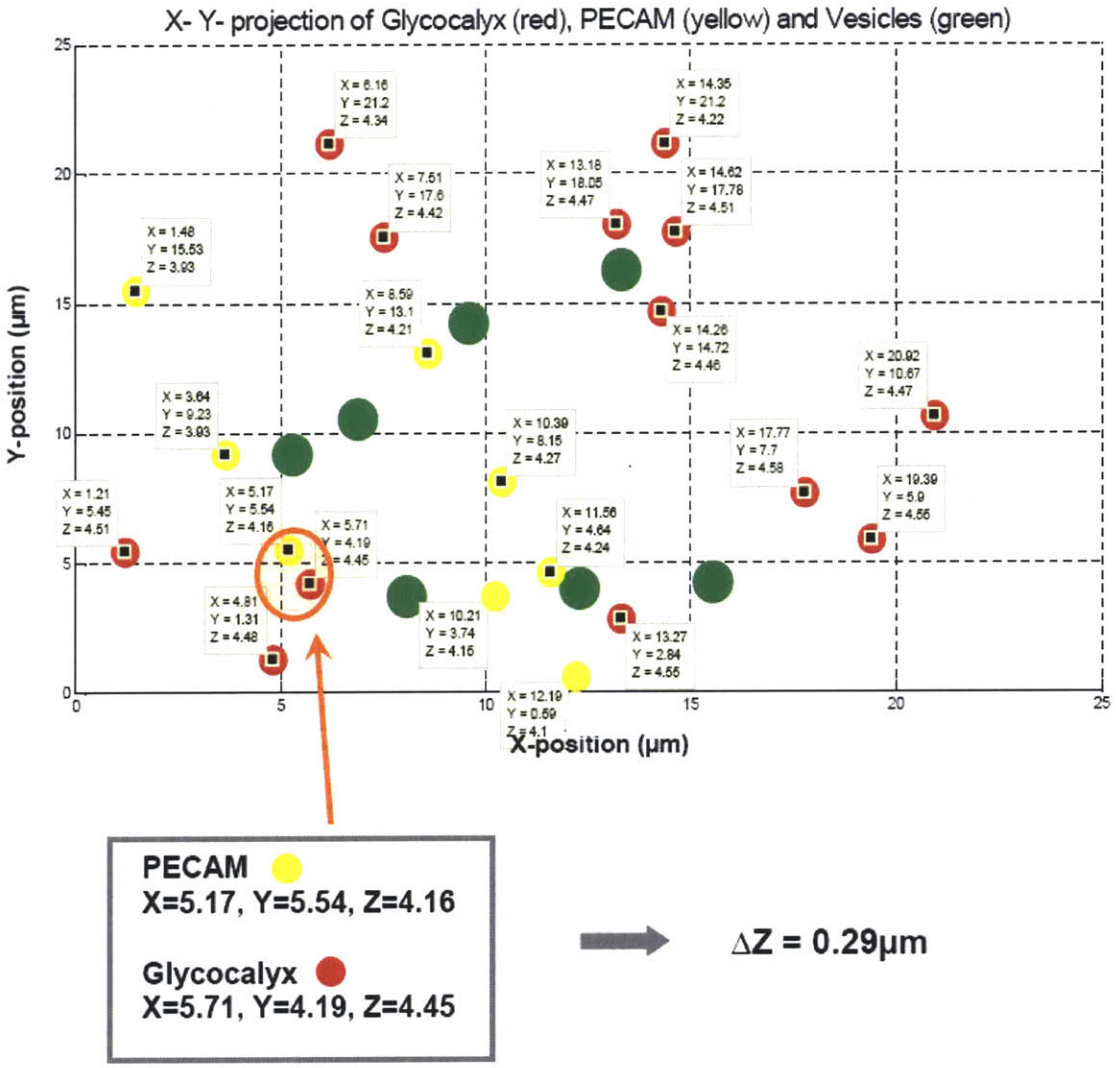

Figure 4-14 Two-dimensional mapping providing the detailed spatial position of each dot, including glycocalyx-dot (red), PECAM-dot (yellow) and vesicle-dot (green). Estimating from the PECAM-glycocalyx pair that are closely neighbouring to each other, the glycocalyx thickness from at this location is about 290nm.

Method 2: Membrane surface fitting using PECAM dots

Assuming an ellipsoidal shape of the cell body, consistent with reported AFM measurements (11), we can simulate a continuous surface of cell membrane by fitting the positions of eight PECAM-dots to an ellipsoidal surface. Illustrated in Fig 4-15, a typical ellipsoid is described by $\frac{(x-x_0)^2}{x_r^2} + \frac{(y-y_0)^2}{y_r^2} + \frac{(z-z_0)^2}{z_r^2} = 1$, with six input variables $x_0, y_0, z_0, x_r, y_r, z_r$ controlling the shape. Applying non-linear curve fitting in least square sense, we have obtained an ellipsoidal membrane that includes most of the PECAM-dots as expected (Fig 4-16). Matlab-returned six parameters,

$$\begin{array}{lll} x_0 = 12.23\mu m, & y_0 = 12.47\mu m, & z_0 = 1.39\mu m; \\ x_r = 22.27\mu m, & y_r = 38.28\mu m, & z_r = 2.88\mu m \end{array}$$

, fall into the physical range of cell geometry. Therefore, the z-distance of each individual glycocalyx-dot above membrane can be calculated by comparing it to z-position of the membrane right beneath the dot (at the same x and y postion). Table 4-2 shows the result of the ΔZ of each glycocalyx-dot, which indicates how far the dot is attached above the membrane. The mean of the ΔZ yields an estimate of average glycocaly thickness on the cell, about 0.35 μm, which is on the same order of magnitude of the result from method 1.

$$\frac{(x-x_0)^2}{x_r^{\,2}} + \frac{(y-y_0)^2}{y_r^{\,2}} + \frac{(z-z_0)^2}{z_r^{\,2}} = 1$$

$$x_0 = 0, \quad y_0 = 0, \quad z_0 = 0;$$

$$x_r = 5, \quad y_r = 3, \quad z_r = 2.$$

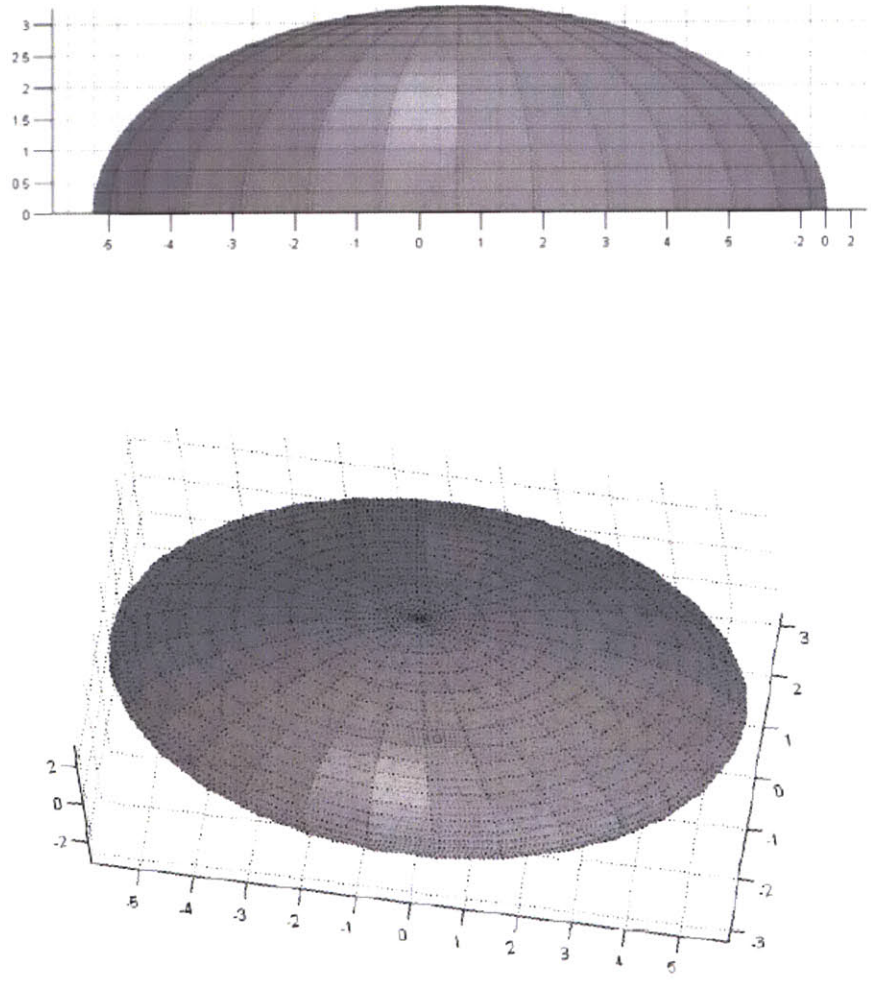

Figure 4-15 Representative ellipsoidal surface to simulate cell membrane.

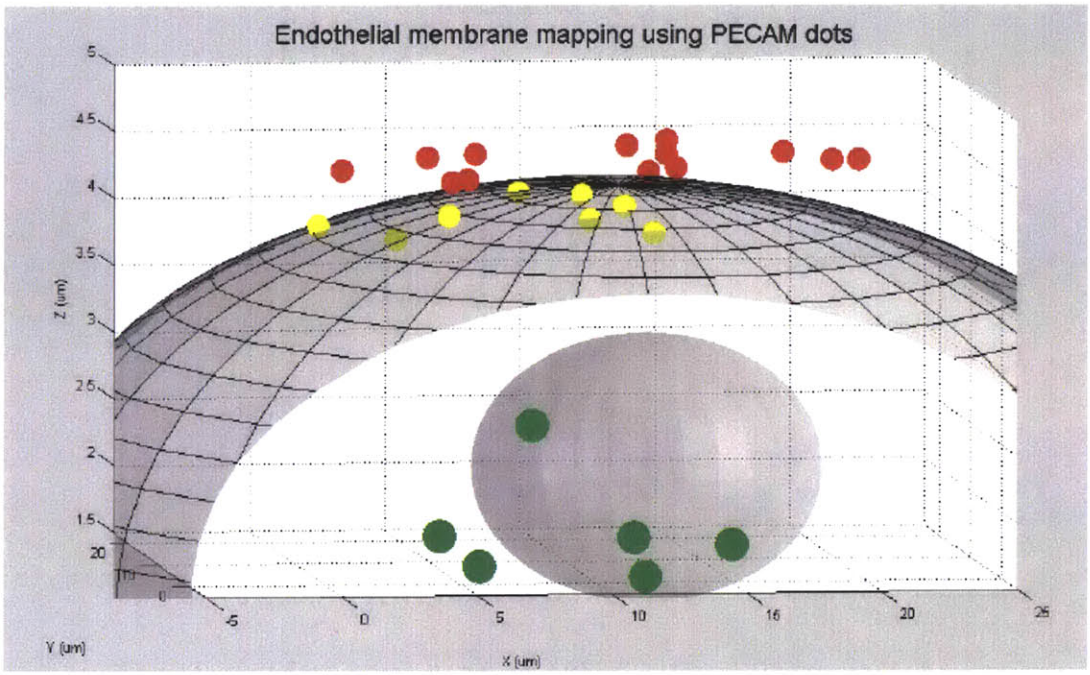

$$\frac{(x-x_0)^2}{x_r^{\,2}} + \frac{(y-y_0)^2}{y_r^{\,2}} + \frac{(z-z_0)^2}{z_r^{\,2}} = 1$$

$$x_0 = 12.23\mu m, \quad y_0 = 12.47\mu m, \quad z_0 = 1.39\mu m;$$

$$x_r = 22.27\mu m, \quad y_r = 38.28\mu m, \quad z_r = 2.88\mu m.$$

Figure 4-16 Matlab fitting using 8 PECAM dots (yellow marker) generates a simulated membrane surface just beneath the glycocalyx layer (red marker). The hollow space encompassed by intracellular vesicles (green marker) indicates the presence of the nucleus.

Glycocalyx-dots ΔZ from membrane

Number	X (μm)	Y (μm)	Z (μm)	Z_membrane (μm)	Δ Z (μm)
1	1.21	5.45	4.51	3.84	0.67
2	13.27	2.84	4.55	4.17	0.38
3	7.51	17.6	4.42	4.18	0.24
4	6.16	21.2	4.34	4.08	0.26
5	5.71	4.19	4.45	4.07	0.38
6	4.81	1.31	4.48	3.97	0.51
7	17.77	7.7	4.58	4.16	0.43
8	13.18	18.05	4.47	4.24	0.23
9	14.62	17.78	4.51	4.22	0.29
10	20.92	10.67	4.47	4.04	0.43
11	19.39	5.9	4.55	4.07	0.48
12	14.26	14.72	4.46	4.25	0.21
13	14.35	21.2	4.22	4.18	0.04
Average Δ Z (μm)					0.35
Standard Deviation (μm)					0.17

Table 4-2 The distance of each glycocalyx-dot away from the fitted membrane yields an estimate of the glycocalyx thickness, 0.35 ±0.17μm.

4.4. Conclusion and Discussion

As described in this chapter, we have developed an optical imaging system capable of tracking single particles in all three spatial dimensions with nanometer resolution. When employed in conjuction of quantum dots, this 3D tracking method may be implemented in a number of important biological investigations, overcoming several limitations that have been barricading other conventional tracking techniques. To name a few, this method provides excellent opportunities for researchers:

1. to three-dimensionally track the position of individual particles (including DNA, proteins, or most other biological targets) with a spatial resolution nearly impossible by traditional optical methods including confocal microscopy,
2. to continuously monitor the location or the dynamics of the object for significantly longer period of time with high temperal resolution,
3. to observe biological events that evolve in a larger time scale that would not otherwise be possible to trace, and
4. to resolve sub-micron structures with dimensions comparable to (or even smaller than) the diffraction limit of light.

With this method in use, we have for the first time mapped the endothelial glycocalyx layer in living cells in a three-dimensional space, and estimated the *in vitro* thickness of this endothelial surface layer. The two estimation methods we applied yield similar glycocalyx thickness, both on the same order of magnitude with the limited *in vivo* observation.

Another interesting optical aspect of quantum dots is their structure of emission dipole that can be used to track the orientation of single nanoparticles. Recently demonstrated by Brokmann *et al.*(21), defocused optical imaging can generate inference patterns encoding orientational information of the quantum dot. By fitting the contour intensity to an analytic formula, one can determine the dot orientation (Θ, Φ), Θ being the angle with respect to the optical axis, and Φ being the angle projected onto XY plane. This method may provide opportunities in studies where not only spatial position of single dot but also the rotational dynamics is desirable.

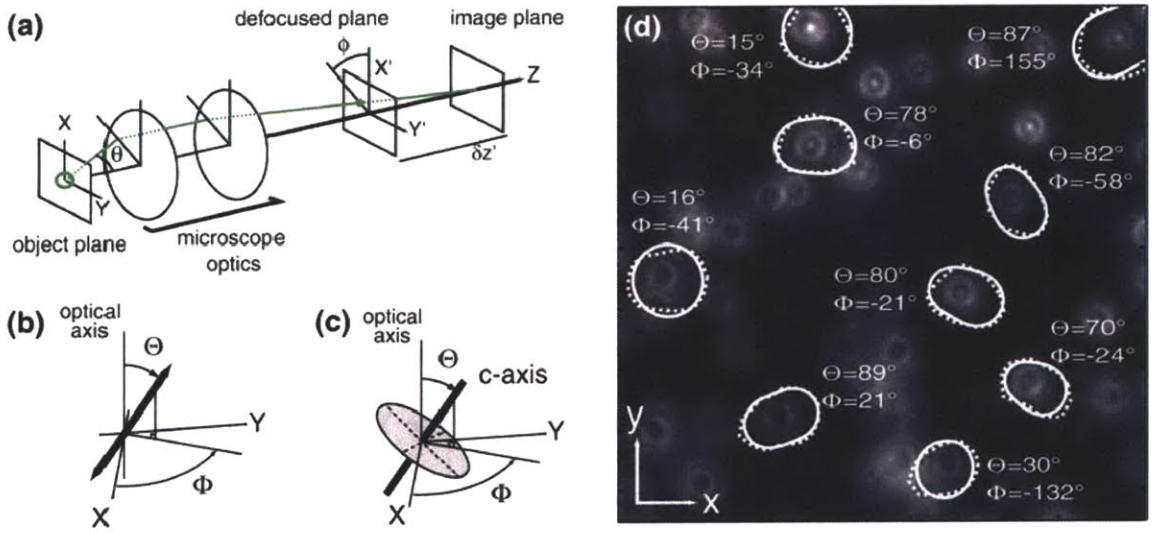

Figure 4-17 Off-focus ring pattern of quantum dots contains orientational information (21). Panel (a) illustrates the principle of defocus imaging; (b) and (c) defines the orientation of single dot with respect to optical asis (Θ) and XY plane (Φ); (d) demonstrates imaging sample of quantum dots with different orientations determined by fitting contour intensity to an analytic formula. Figure from Brokmann *et al.*(21)

Chapter 5. Measuring the Dynamics of Endothelial Glycocalyx under unsteady flow

5.1. Introduction

A wide range of studies have demonstrated the importance of the glycocalyx in regulating vascular functions, including mechanotransduction, endothelial permeability, leukocyte attachment and red blood cell passage (55, 69, 147, 149, 157, 161, 162, 165). The glycocalyx, appearing as an interface between the endothelial cells and the flowing blood (or blood cells), provides the direct contact ground where major mechanical deformations of both sides occur. Thereofore, our understanding of the mechanism behind those hemodynamically-induced biological events largely depends on the answer to one central question ----- *what is the mechanical property of the glycocalyx?* .

Despite the fact that the mechanical properties of endothelial cells have been matters of study for a very long period of time with a variety of experimental approaches availabe for this purpose, previous studies of the glycocalyx provides very limited information about its mechanical properties. Elasticity, or the Young's modulus, of a cell can easily be examined by a number of probing techniques, such as micropipette aspiration, cell indentation, optical traps, magnetic twisting, and AFM(94). The application of those techniques to the glycocalyx however, turns out to be mostly unrealistic. The highly-hydrated fragile structure can hardly resist the force exerted by AFM tip or cell poker, and the use of microspheres in magnetic twisting or optical traps seems inapproriate when studying structures such as the glycoclcayx with sub-micron dimension.

In order to measure directly the elasticity of an intact glycocalyx layer on living cells, we have developed an ultra-resolution imaging technique to trace the motion of the glycocalyx-attached nanoparticles (quantum dots) when subjected to oscillatory flow controlled in a micro-fluidic system. The flow-induced deformation under various levels of shear stress thus enables us a direct estimation of the shear modulus, for the glycocalyx matrix with a thickness of ~ 350nm as previously obtained. Selecting quantum dots as fluorescent tracer in this method posseses a number of advantages over using traditional fluorophores in optical microscopy, as previously discussed in Chapter 4 and again later.

5.1.1.Mechanical Properties of the Glycocalyx

To date, there are still no direct measurements of the elasticity of the core structure of the glycocalyx (e.g. proteoglycans) similar to those performed on other cellular components, such as actin filaments and microtubules (62, 76). The sub-micron dimension and the fragile polysaccharide nature of the glycocalyx layer have created great challenges for the application of conventional mechanical probing techniques.

Among limited experimental data on the mechanical properties of the glycocalyx layer, one pioneer study by Vink *et al* (67, 158)shows that the glycoclayx *in vivo* can be crushed to as much as 20% of its undeformed thickness by the passage of a leukocyte through a capillary, and the layer gradually recovers with a time constant of ~0.4s.

Based on this observation, Weinbaum *et al* (162) developed a model to estimate the flexural rigidity, *EI*, of the layer. The model treats the core proteins as elastic fibers and

uses small deflection theory to predict the long-time final decay of the fiber's elastic recoil (161). This lineraized model therefore predicts the *EI* of the glycocalyx to be 700 $pN{\cdot}nm^2$, about 1/20 of the measured value of an F-actin filament (53). Furethemore, it suggests that the tip deflection of a single fiber under a fluid shear stress of 10 dynes/cm2 at the edge of the glycocalyx layer is only 17.9nm (162). More recently, Han *et al.* stated a more sophisticated large deformation model for elastica that predicts the *EI* is 490 $pN{\cdot}nm^2$ (67). As those models provide only theoretical frameworks, proper experimental approach needs to be developed to directly measure the mechanical properties of the glycocalyx in reality.

5.1.2.Existing Models of the Glycocalyx

5.1.2.1. Hemodynamic model for flow in the glycocalyx

Several recent studies focusing on the role of the glycoclayx in mechanotransduction, in WBC rolling and RBC passaging in capillary all adopted the assumption that the fluid shear stress at the edge of the glycocalyx is greatly reduced as it propagates through the fiber matrix and the resulting shear stress at the endothelial membrane is effectively zero (67, 149, 162, 168). This can be explained in the hemodynamic model as following (161).

The hemodynamic model for the flow in the glycocalyx begins with applying the Brinkman equation to a poroelastic layer with small solid volume fraction, stated as

$$\begin{aligned} -\mu\nabla\times\nabla\times v \; - Kv \; &= \nabla p \\ \nabla\cdot v \; &= 0, \end{aligned}$$

where v is the fluid velocity in the layer, p is the pressure field, μ is the fluid dynamic viscosity and K is the hydraulic resitivity(40). The viscous

drag can be characterized by a dimensionless variable $\delta^2 = \mu/(h^2 K)$, where h is the effective thickness of the layer. δ^2 represents the ratio of the viscous drag forces caused by fluid-velocity gradients in the glycocalyx layer to the permeation-induced viscous drage due to the fluid motion relative to the solid constitute of the matrix. Estimates of K ~ 10^{10}-10^{11}dyn·s/cm^4(41, 162), μ ~0.01 dyn·s/cm^4 (equal to blood plasma)(161) and h~0.5μm give rise to δ^2, in the range of 10^{-4}~10^{-3}. Therefore, for such small values of δ^2 (<<1), a Darcy flow dominates away from outer edge of the glycocalyx layer, and the fluid shear stress on the membrane is attenuated to almost zero.

5.1.2.2. Models for restoring mechanism

Three models have been developed to explain the restoration mechanism behind the experimental observation that the glycocalyx layer recovers ~ 1s after it has been crushed by a passing white blood cell. Weinbaum *et al* (161) summarized the three models in a recent review paper.

a. Oncotic model

Pries and Secomb (112, 132) developed an oncotic model that states even a small difference between the protein concentration in the glycocalyx and the plasma concentration in blood would be capable of generating sufficient osmotic pressure to exclude red blood cells from the glycoclayx layer under physiological flow conditions in capillaries. The source of the restoration force of a compressed glycocalyx layer, anayzed by this model, is chemical in nature instead of mechanical.

This model suggests that when in equilibrium, the excessive oncotic pressure within the layer would be balanced by tension in the layer. Compression of the layer by mechanical load (e.g. during red blood cell passaging) would result in a further enhanced pressure difference and a reduced tension that together could balance the external force. During the recovery phase once the load is lifted, tension within the layer would then be reestablished to restore the condition in equilibrium. Their analysis shows that an oncotic pressure of only 20 dynes/cm^2 in equilibrium could be large enough to exlude red blood cell from the glycocalyx layer (132, 161).

b. Elastohydrodynamic model

Elastohydrodynamic model, first introduced by Weinbaum *et al.* (162), considers the core protein fibers having a finite flexural rigidity, *EI*, that could withstand fluid shear stress exerted at the outer edge of the fibers in the physiological range. Based on the observation of the glycocalyx compression by the passage of a WBC(158), this model predicts the flexural rigidity of the layer, *EI*, to be 700 pN·nm^2.

Later, Han *et al.* (67) developed a more sophisticated nonlinear elastohydrodynamic model that predicted a two-phase recovering mechanism to explain the time-dependent restoration of the glycocalyx after the passage of the WBC. As shown in Fig 1-8(a), during intitial phase for large compression, the glycocalyx is less than 36% of its uncompressed thickness, and the ends of fibers appear parallel to the endothelial membrane. Once entering phase two, the fibers recover bending similarly to the shape of

elastic bars. According to their analysis, shown in Fig 1-8(b), the model shows a good agreement with experimental data regarding the transients of glycocalyx recovery.

c. Mechano-electrochemical model

In this model, Damiano & Stace described that the structural integrity and restoration mechanism of the glycocalyx originate from its electrochemical nature of higly-charged macromolecules in a mixture hydrated in an electrolytic fluid (41). In the absence of axial flow in the vessel, they considered one-dimensional finite deformation of the layer, modeled as an isotropic quaternary mixture. Based on the assumption that the volume fractions of the solid and ionic constituents and the viscosity of the fluid constituents are all negligible, they applied the constitutive law using Nernst-Planck equation to describe the solid and ionic flux. Consequently, the model predicts that the glycocalyx recovers after deformation as a result of a combination of electrostatic and chemical potential gradients. The interaction of the fixed-bound charges in the matrix with the free ions in the solution generates the electrostatic potential gradient across the matrix, whereas a higher concentration of bound GAGs, glycoproteins, and proteoglycans compared to the corresponding consitituents in the blood is the main reason of the chemical potential gradient. Their prediction of the recovery process (also shown in Fig 1-8(a)), compared with observation of ~1s recovery time (158), gives rise to an estimated fixed-charge density of the glycocalyx layer of ~1mEq/l (41).

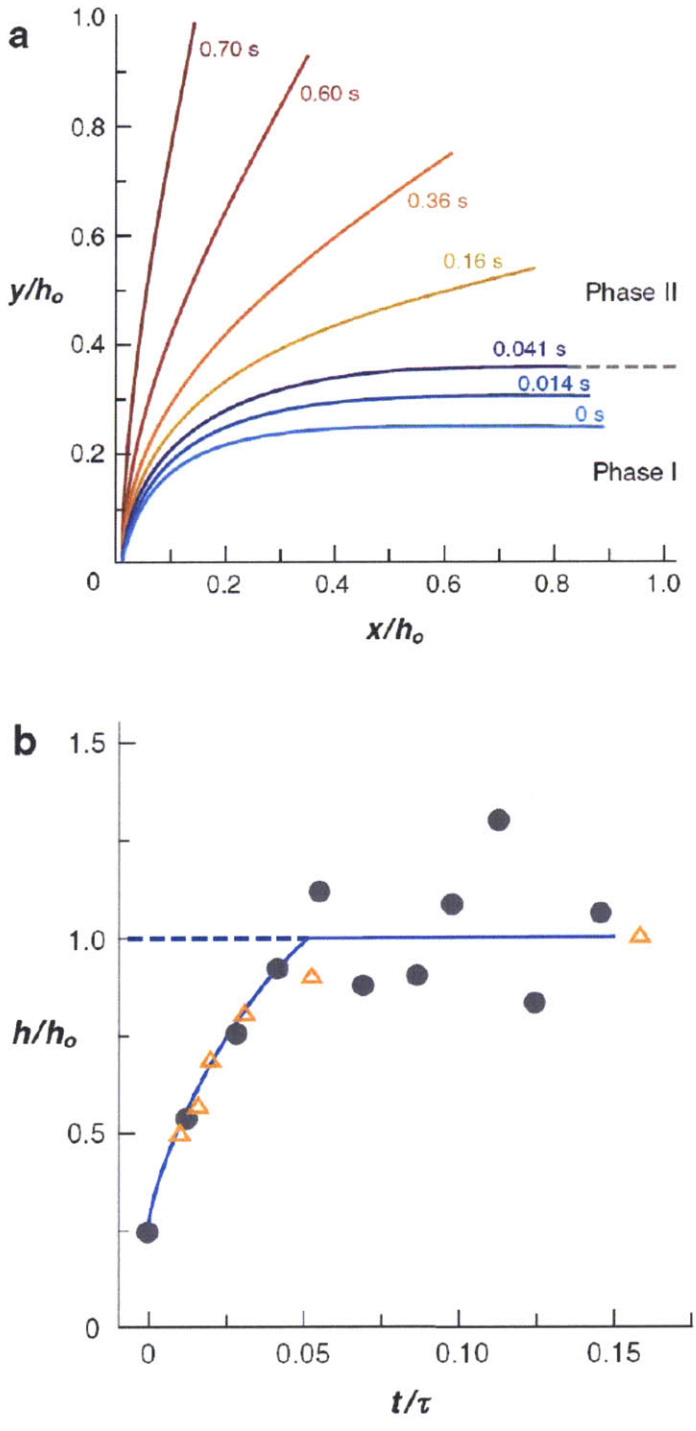

Figure 5-1 (a) Time-dependent glycocalyx layer restoration after compression by a WBC experiencing two phase transition, predicted by Han et al.(67). (b) Comparison of model prediction by Han (*solid line*) and prediction by Damiano & Stace (41)(*open triangle*), with experimental results (67, 158), describing time constants of glycocalyx recovery (161).

5.2. Materials and Methods

5.2.1.Cell Sample Preparation

Primary bovine aortic endothelial cells (BAEC-77, passage 10-15) are cultured in DMEM supplemented with 10% fetal calf serum, 1% L-glutamine, and 1% penicillin-streptomycin. Before seeding, cell culture flasks and glass slides are coated with 0.2% gelatin at room temperature. Microfluidic chambers are coated with 100μg/ml fibronectin to promote cell attachment in micro-enviroment. Cell cultures are kept in a humidified incubator maintained at 37^0C, with 5% CO_2 and 95% air.

After cell monolayers reach confluence in flow chamber (ibidi, Munich, Germany), two layers of QDs were attached to the cell as follows. Cells were incubated in culture medium with 5nM QD565 (gift from Prof Bawendi's lab) for 15min at 37^0C to allow QD565 into intracellular vesicles via endocytosis. After five times quick rinses in DPBS to remove excessive QDs in solution, cells were chilled on ice for 10min and blocked with 2% goat serum and 2% BSA for 20min to reduce nonspecific background staining. To label the glycocalyx layer, cells were incubated with 5 μg/mL heparan sulfate biotin antibody (US Biological) for 20 min and washed three times with DPBS. Cells were subsequently incubated with 2nM streptavidin-QD655 (Invitrogen) for 15 min, and later washed with DPBS. Cell labeling procedure was performed on ice so as to limit QD endocytosis during the incubation procedure, with the only exception of QD565. Cell samples were later transfered onto the nanopositioner and imaged at room temperature.

5.2.2.Flow System Setup

A high-precision peristaltic pump (ISMATEC) was used to generate flow to subject endothelial cells to oscillatory shear stress. The most common flow input in our experiments was in cycles of 2s forward and 2s backward, with a flow rate of 9ml/min, which converts to a shear stress of 15 dynes/cm^2 exerting on cells.

5.2.3.Optical Setup

Similar to the method described in Chapter 4, a laser beam of 514nm (Innova 70C, Coherent) was collimated through a defocusing lense and a 100X oil immersion objective (Nikon Plan Fluor) to illuminate a circular area with a diameter of ~40μm of the sample positioned on an xyz- piesoelectric nanopositioning stage (Queensgate). The photons emitted by the QDs in the excitation volume was reflected by a beam splitter to pass through an imaging lens, a notch filter and detected by an image intensified camera of 12-bit resolution and 512 pixels x 512 pixels (iCCD camera, Pentamax).

5.2.4.Data Acquisition and Analysis

Images from the iCCD were captured using the WINspec data acquisition software and saved as SPE files. Individual cells were first identified using QD565 signals, and thus images for Glycocalyx-QD on the same cell could be recorded later by switching filters. A custom-written Matlab code was developed to fit one point spread function (PSF) in successive frames to a two-dimensional (2D) Gaussian function. The position of the QD's center is therefore determined by the Gaussian fitting and used to compute the particle trajectory over time.

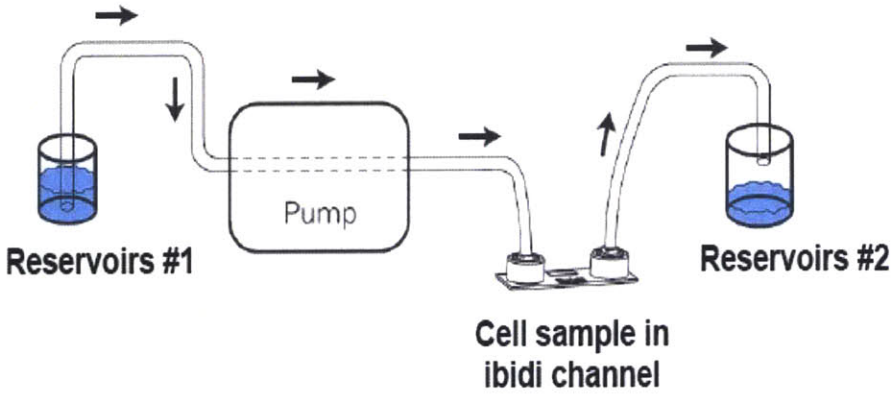

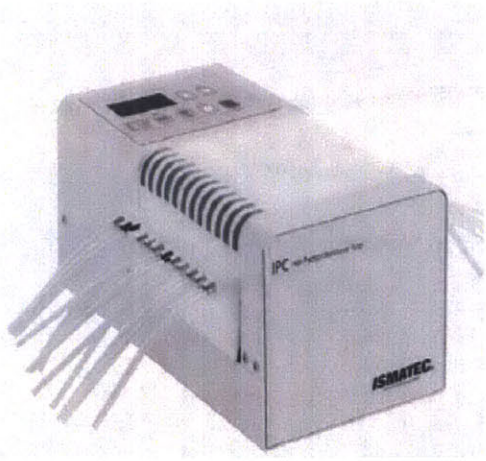

High-precision peristaltic pump

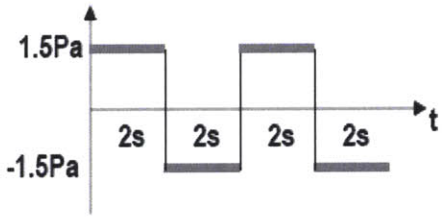

Flow input

Figure 5-2 Flow system to subject cyclic shear stress to endothelial cells placed in flow channel.

5.3. Results

5.3.1.Flow-induced Dynamics of the Endothelial Glycocalyx

After quantum dots are conjugated to the glycocalyx layer, cell sample is assembled in a microfluidic system that applies cyclic shear stress to the endothelial monolayer. The magnitude of controlled shear stress, determined by chamber geometry and flow rate, is typically 15 dynes/cm^2 at a flow rate of 9ml/min. Once the flow chamber is immobilized on the microscope stage, certain region of interest is selected (usually by adjusting the image frame to cover one integral cell) and the positions of quantum dots in this region are recorded during flow application.

One representative recording at a frame rate of 5Hz is shown in Fig 5-3, where 0.25Hz flow is started in the vertical direction. Over a period of ~80s, the x-postion of the quantum dot (yellow arrow in Fig5-3) reflects random drifting of the cell, while the y-position clearly indicates oscillations in sync with the flow (Fig 5-4). Fourier analysis in Fig 5-4 further confirms flow-induced dot motion, by showing a peak signal at 0.25Hz only in the y-axis power spectrum. Secondary oscillation is also observed within each cycle, due to the pulsation generated by the peristaltic pump. Similarly, the oscillation caused by the pulsation at a frequency of 1.5Hz, is decoded in the power spectrum as minor tails around 1.5Hz. Statistics over 15 dots on 3 independent samples find flow-induced glycocalyx deformation to be 108nm on average, with a standard deviation of 77nm suggesting variation from cell to cell and point to point on a single cell.

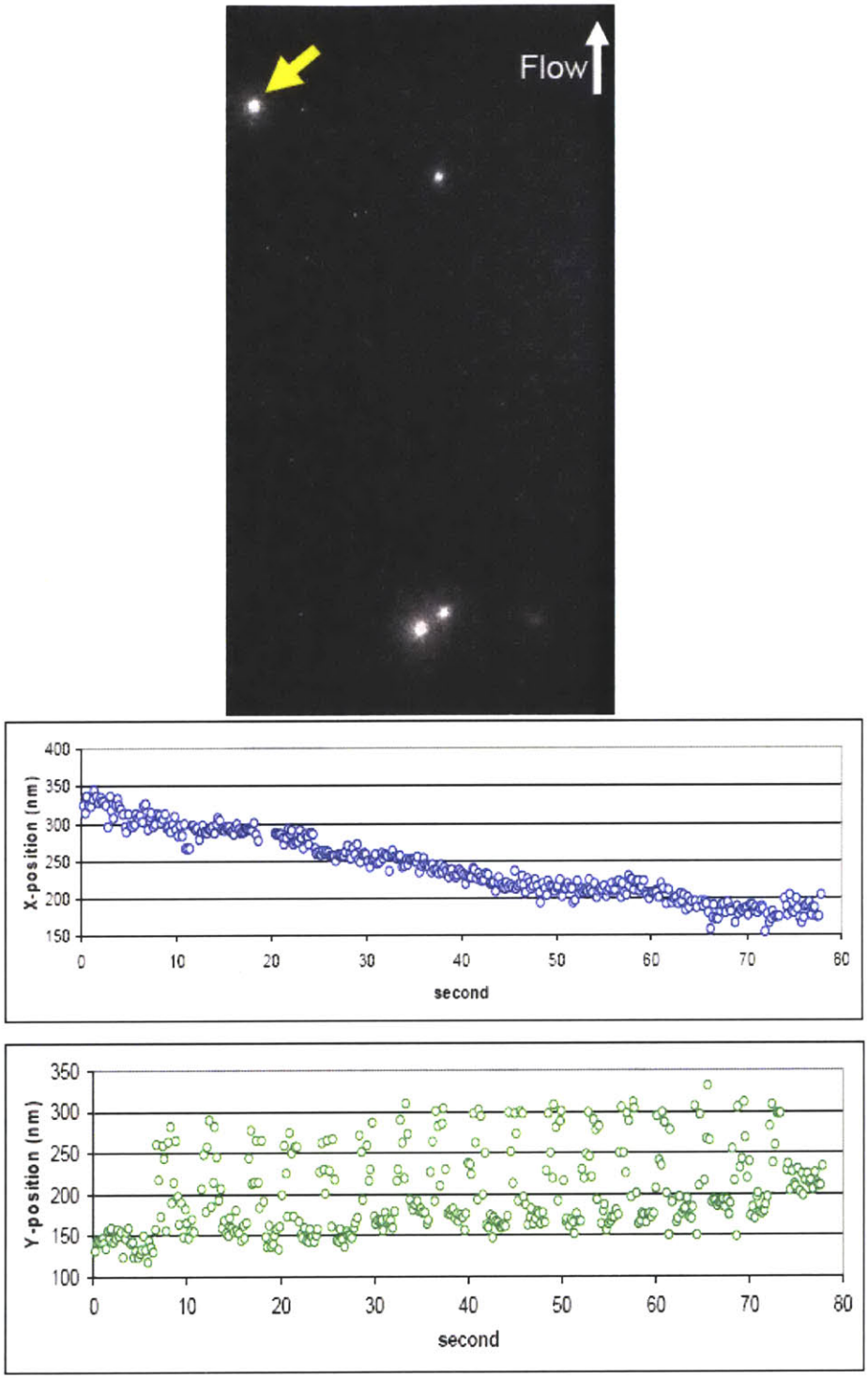

Figure 5-3 Representative image of quantum dots during flow application. X-position of the dot over time reflects a random drifting of the cell, while y-position indicates flow-induced oscillation.

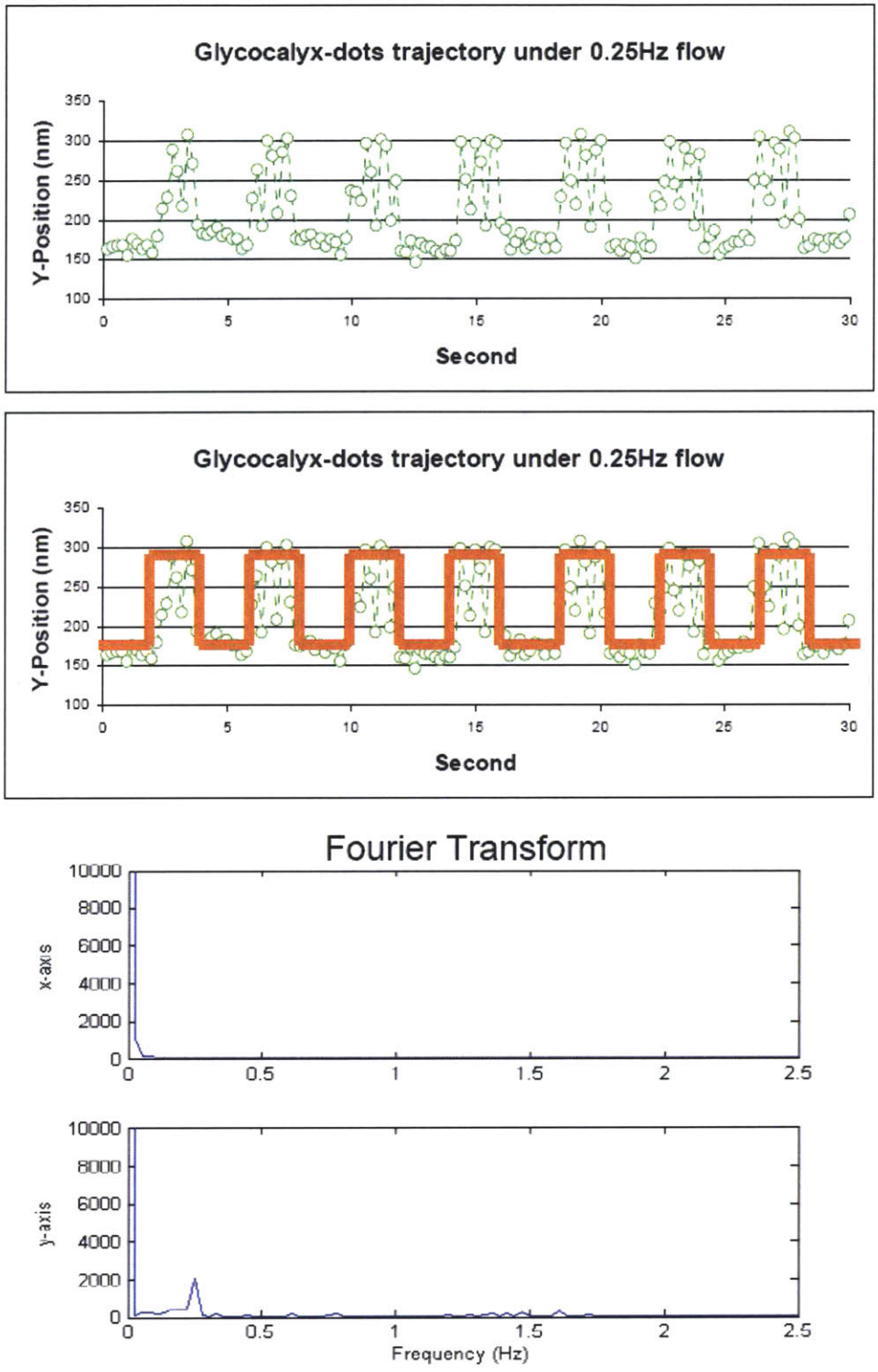

Figure 5-4 Fourier analysis of the data in Fig 5-3 corroborates the dot's cyclic motion in y-axis (shown as a peak at 0.25Hz in the power spectrum) and random drifting in x-axis (no frequency signal except for DC gain in the power spetrum).

A set of control experiments and theoretical estimates were carried out to ensure the measured oscillation indeed represents flow-induced glycocalyx deformation, not otherwise.

1. Glycocalyx-bound dot motion without flow

Right after quantum dots were attached to the glycocalyx strands, cell sample was imaged under microscope without flow presence. Restricted random motion of glycocalyx-bound dots was monitored over time per each 0.2s time interval, shown in Fig 5-5. The square root of the mean square displacement of a single dot is calculated as $\sqrt{\langle \Delta r(t)^2 \rangle} \approx 15nm$, meaning the average distance a dot moves during 0.2s is on the order of 15nm. To ensure the dot is properly attached to the glycalyx instead of freely floating in the medium, we estimated the Brownian motion of a single dot dispersed in water. The diffusivity of a dot with a diameter of ~20nm at room temperature is $D = \frac{K \bullet T}{2\pi \eta a} \approx 4 \times 10^{-11}\ m^2/s$, where K is the Boltzman constant ($1.38 \times 10^{-23} m^2 kg/s^2 K$), T represents the absolute temperature (~300K at room temperature), η denotes the dynamic viscosity of the liquid ($\sim 10^{-3}$ Pa·s), and a means the particle size (~ 10nm in radius). Since the Brownian motion of a particle is determined by the diffusivity of the solution, the average distance a free 20nm-sized particle during each 0.2s time interval is about $\sqrt{\langle \Delta r(t)^2 \rangle} = \sqrt{6D \cdot \Delta t} \approx 7\mu m$. Had the dot not attached to the glycocalyx strand, it would have moved ~7μm during each step in the trajectory, more than two orders of magnitude greater than the observed 15nm motion. It thus can be concluded that the dots are successfully attached to the matrix.

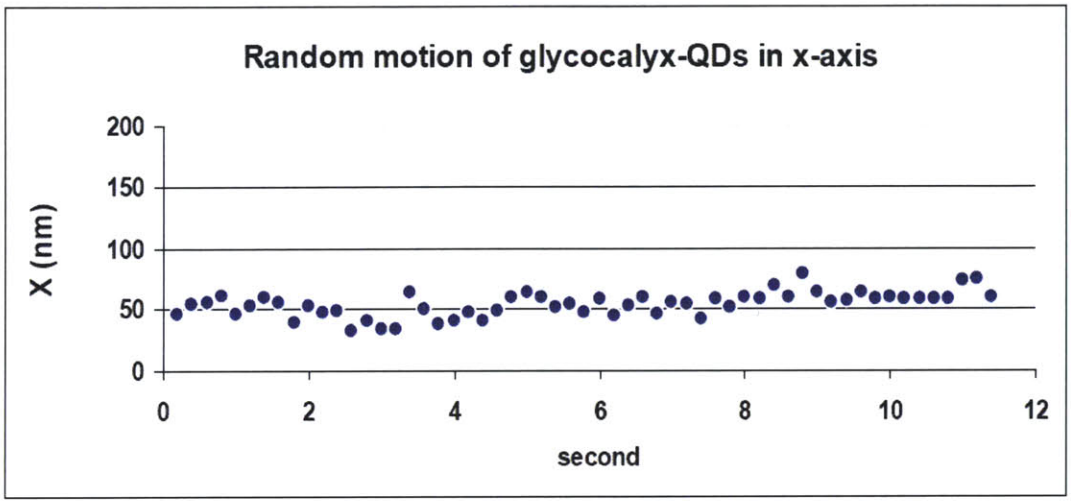

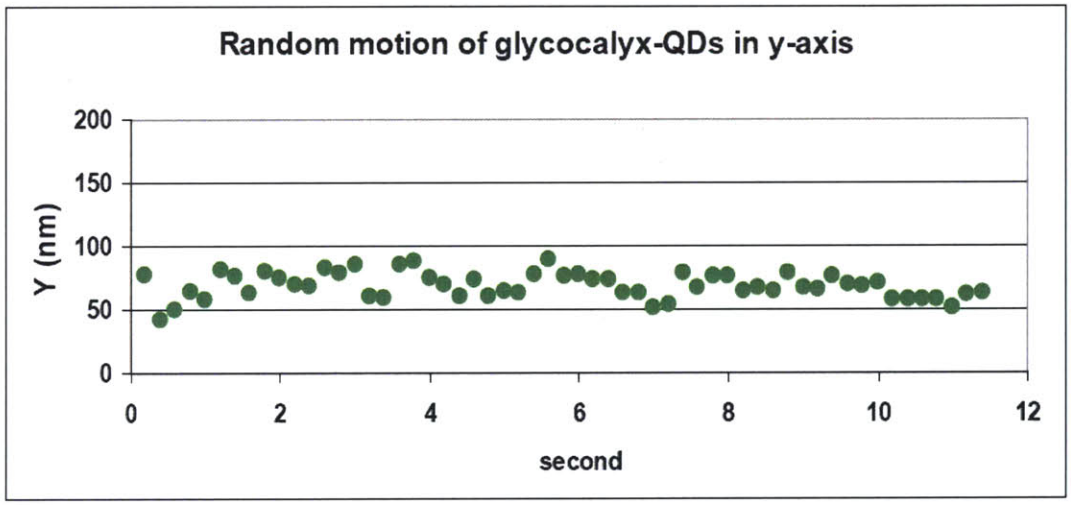

Figure 5-5 Glycocalyx-attached quantum dots monitored over time without flow application. Square root of the mean square displacement of dot random motion during each 0.2s interval is $\sqrt{\langle \Delta r(t)^2 \rangle} \approx 15nm$, confirming the dots are properly bound to the glycocalyx strands.

2. Fluid drag on the dot *versus* protein bond strength

When we applied flow to the QDs-imbedded glycocalyx matrix, the fluid drag on the dot was negligible compared to the bond strength that brings the dot and glycocalyx strands together. The fluid drag on a 20nm sized particle is $F = 6\pi \eta a v$, thus approximately $10^{-4} pN$ in our case. The rupture force of the streptaividin-biotin bond that links a quantum dot to the glycocalyx is measured to be on the order of 5pN by optical trapping technique(103), 4 orders of magnitude greater than the fluid drag on the dot. Thus, bond interation is sufficiently strong to ensure firm attachment of dots to the matrix.

3. Flow-induced motion of membrane-bound quantum dots

By conjugating quantum dots to PECAM on endothelial membrane (as described in Materials and Methods), we observed flow-induced membrane movement as an indication of endothelial cell itself influenced by shear. At a shear stress of 15dynes/cm^2, membrane oscillation induced by the flow stayed within a range of ~ 20nm (Fig 5-6), near the limit of our detection precision. The small magnitude of cell deformation confirmed a much stiffer nature of cell body, compared to the large deformation of the glycocalyx caused by shear stress of same magnitude. The shear modulus of the endothelial cell, by approximating cell height on the order of ~4μm(12), is estimated to be ~ 300Pa. This is consistent with previous observations of endothelial stiffness measured by other techniques (99, 128)

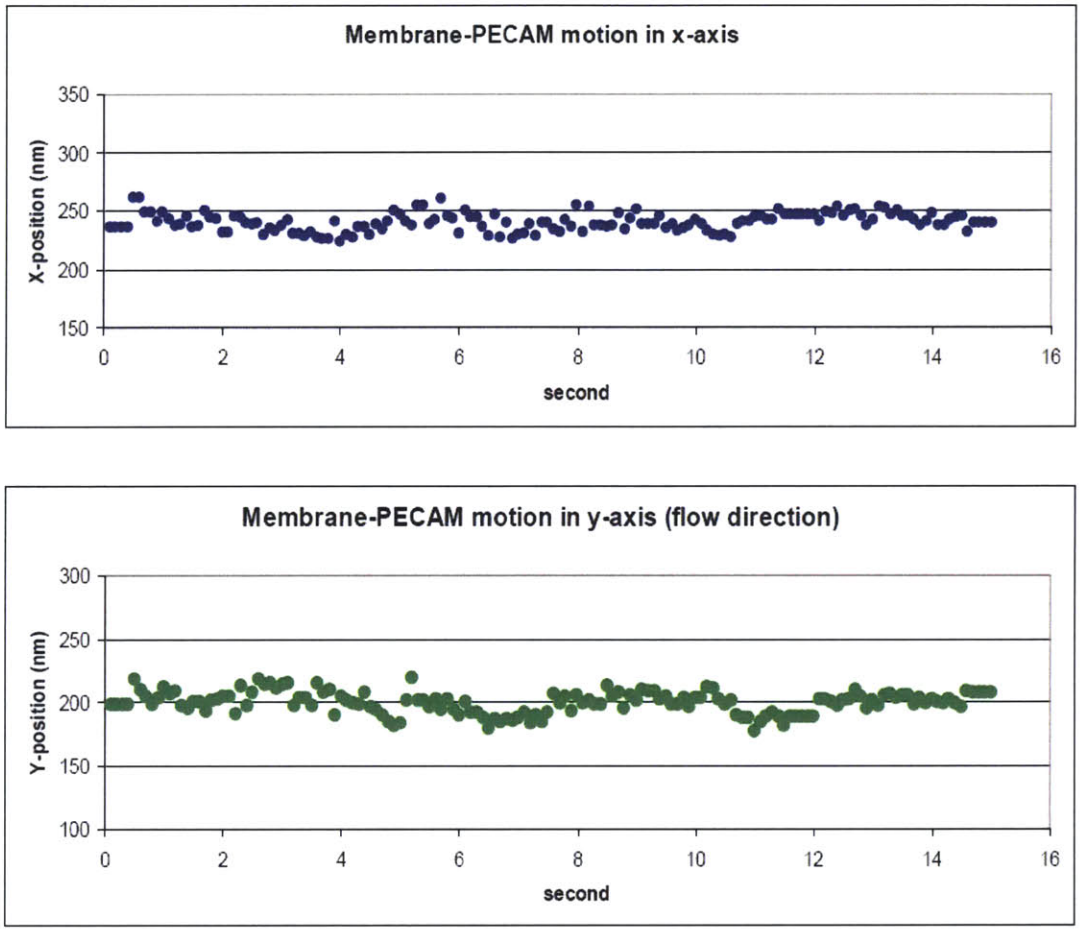

Figure 5-6 Membrane-bound PECAM motion driven by cyclic fluid shear stress of 15 dynes/cm^2 at 0.25Hz. Flow-induced membrane motion in the y-axis (flow direction) stayed within a range of ~20nm, much less compared to the glycocalyx motion under similar shear application.

5.3.2. Shear Modulus of the Endothelial Glycocalyx

The shear modulus, G, of a three-dimensional matrix is defined by $G = \frac{\sigma}{\Delta x / h}$, where σ denotes shear stress, Δx represents the deformation under shear, and h is the matrix thickness (Fig 5-7). Shear stress σ is maintained at a 1.5Pa during flow, and h is previously measured to be ~ 350nm for the glycocalyx layer. Therefore, with glycocalyx deformation Δx =108±77nm, shear modulus of this matrix is estimated to be $G = 6.7 \pm 3.3 Pa$.

The elasticity of endothelial cell itself has been examined in both experimental and analytical studies. Indentation experiments using atomic force microscopy (AFM) technique reported endothelial stiffness on the order of ~ 800Pa (99). Micropipette aspiration of an endothelial cell yielded a Young's modulus of the cell in the range from 200Pa to 800 Pa (128, 148). Theoretical studies also predicted cell elasticity on the same order of magnitude (126, 148). These moduli all indicate a much stiffer nature of the endothelial cell than the glycocalyx. Thus, flow-driven membrane motion should be negligible compared to the deformation of the glycocalyx under shear, which is confirmed in our observation of membrane molecules (PECAM) in Fig 5-6.

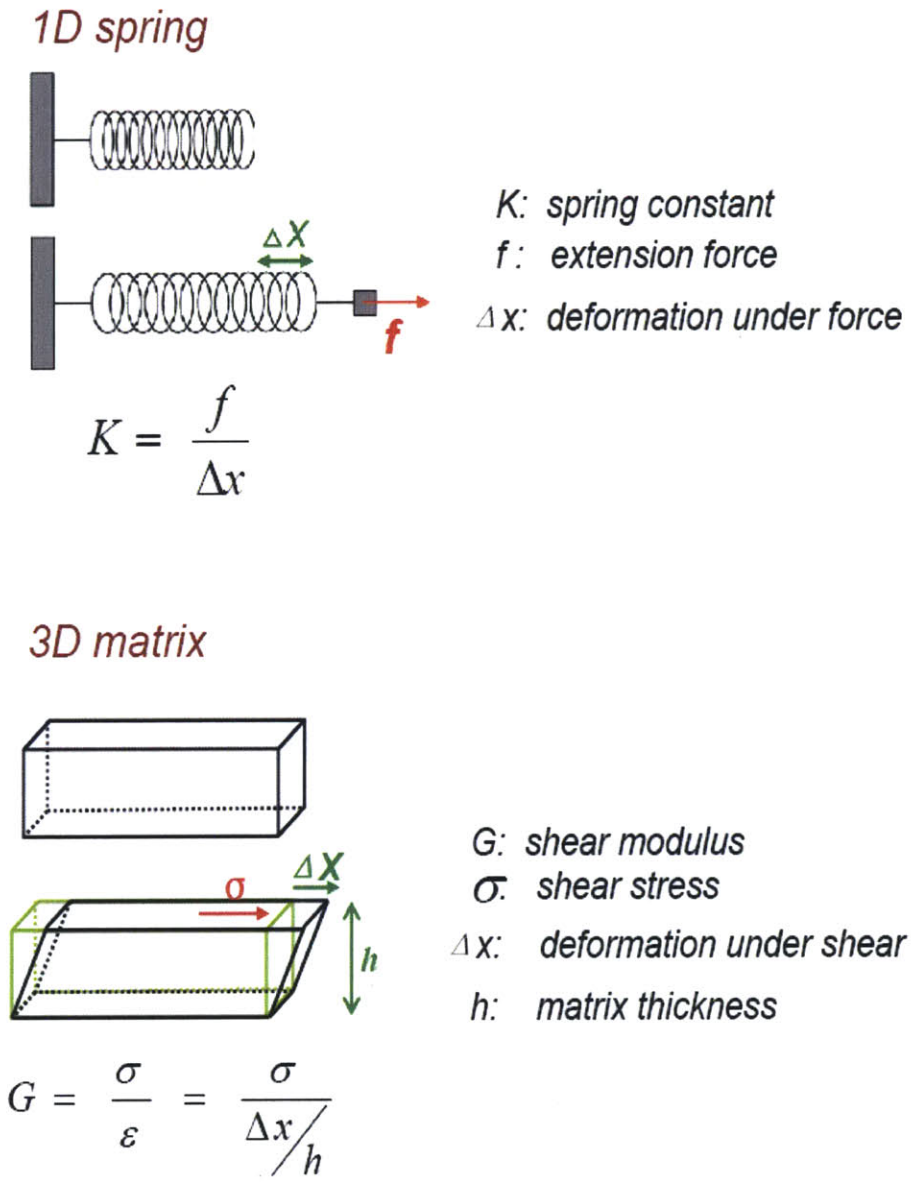

Figure 5-7 Schematic representation of the spring constant of a spring and the shear modulus of a three-dimensional elastic matrix.

5.3.3.Shear-dependency of Glycoclayx's Shear's Modulus

Extending from the endothelial membrane, the glycocalyx is an elastic structure readily deflected by flluid shear stress. Therefore, the greater force we apply, the larger deformation it possibly experiences. Under extreme conditions though, there may be certain physical limits that bounds the maximum layer deformation. To examine the shear dependency of the glycocalyx stiffness, we subjected cells to different levels of shear stress starting from 0.5 Pa to 2 Pa. Typically, the magnitude of shear stress is adjusted by controlling the output of the pump at the desired flow rate that passes through the flow chamber. As we observed, not only does glycocalyx deformation increase with shear, as shown in Fig 5-8, the layer also becomes stiffer.

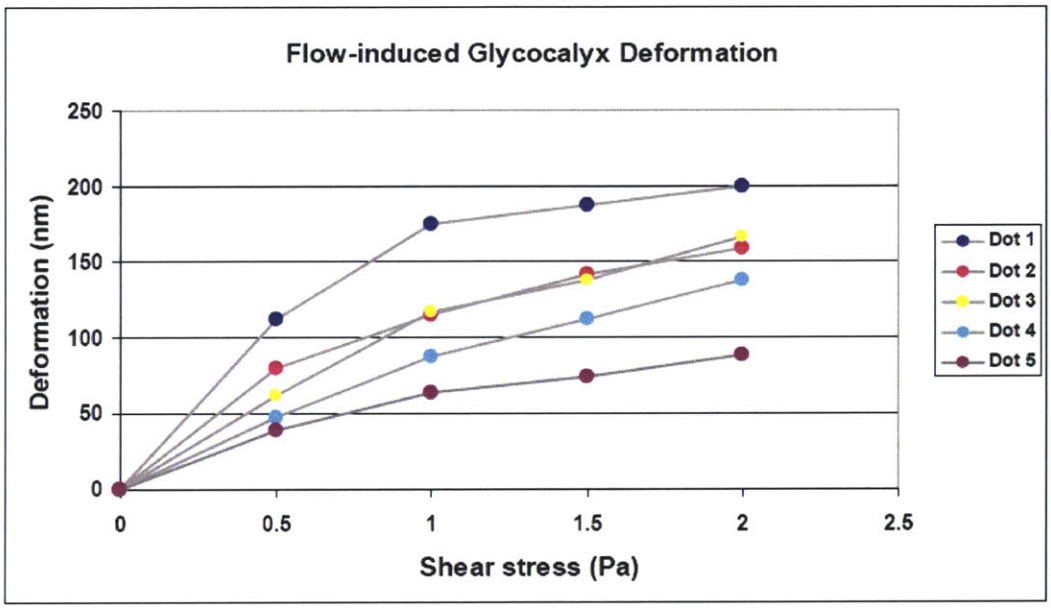

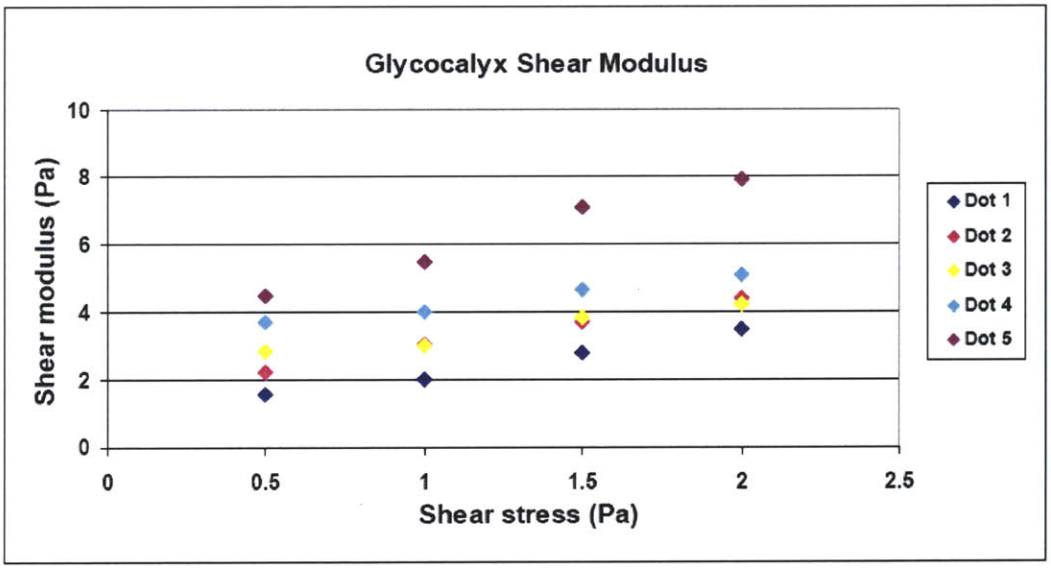

Figure 5-8 Shear-dependency of glycocalyx-deformation under flow. As fluid shear stress increases, deformation keeps increasing and eventually plateaus at high shear stress level.

5.4. Conclusion and Discussion

Using single particle tracking method previously developed, we have successfully located glycocalyx-attached quantum dots with nm spatial resolution and thus have monitored continuously flow-induced layer deformation over minutes. Data have shown the shear modulus of endothelial surface layer to be ~ 6.7Pa, suggesting a significantly softer gel-nature compared to the endothelial cell itself. Increased level of shear stress results in extended layer deformation that plateaus at high shear stress, due to the physical limits that eventually confines the layer extension.

As widely known, flow exerts a pround impact on various aspects of endothelial function, including its mechanical properties. Continuous flow application has been shown to increase endothelial stiffness and reshape its topology and intracellular structure (127). Major structural components such as actin cytoskeleton and intermediate filaments all undergo significant remodeling processes under flow that lead to both global and local adjustments of cell stiffness (11, 68, 102, 127). The glycocalyx, as the interface between flow and endothelium, is possibly modulated by the flow as well. Our method hence provides the opportunity for future study of the change in the mechanical properties of the glycocalyx under flow influence.

Chapter 6. Conclusions and Discussion

6.1. Glycocalyx Serves as Endothelial Mechanosenser to Fluid Shear Stress

In this thesis, we have examined the role of the glycocalyx in mechanotransduction by studying the well-characterized responses of endothelial cells to fluid shear stress. The responses of the glycocalyx degraded cells differ significantly from control cells in several ways 1) 24~48 hr of laminar flow application is not sufficient to induce degraded cell's alignment and proliferation suppression as compared to normal cells; 2) Flow onset does not cause degraded cells to migrate significantly slower than static condition, as opposed to untreated cells which rapidly decrease their motility by 40% during the first few hours of flow application. In concert with several other recent studies of the endothelial glycocalyx (55, 146, 147, 149), we conclude that the glycocalyx plays an important role in mechanotransduction, and further that the removal of the glycocalyx appears to turn off the EC response to shear stress. The evidence of reorganization of glycocalyx under flow also leads us to speculate that not only does the glycocalyx transform mechanical force into biochemical signals inside the cells, but it also has an adaptive mechanism to reorganize itself so as to reduce the shear gradient to which individual endothelial cells are exposed under flow. Other researchers have reported that fluid shear stress could stimulate the incorporation of hyaluronan into the glycocalyx matrix(64), and increased synthesis of sulfated GAGs was also observed under high shear stress (40 dyn/cm^2) condition (6). Fluid shear could possibly promote HSPG synthesis, but our data at the moment are insufficient to resolve this question.

6.2. Implementation of an Ultra-resolution Optical System for Single Particle Tracking to Estimate the *in vivo* Thickness of Endothelial Surface Layer

We have demonstrated the use of an optical imaging system capable of tracking single particles in all three spatial dimensions with nanometer resolution. When employed in conjuction of quantum dots, this 3D tracking method may be implemented in a number of important biological investigations, overcoming several limitations that have been barricading other conventional tracking techniques. To name a few, this method provides excellent opportunities for researchers:

1. to three-dimensionally track the position of individual particles (including DNA, proteins, or most other biological targets) with a spatial resolution nearly impossible by traditional optical methods including confocal microscopy,
2. to continuously monitor the location or the dynamics of the object for significantly longer period of time with high temperal resolution,
3. to observe biological events that evolve in a larger time scale that would not otherwise be possible to trace, and
4. to resolve sub-micron structures with dimensions comparable to (or even smaller than) the diffraction limit of light.

With this method in hand, we have for the first time mapped the endothelial glycocalyx layer in living cells in a three-dimensional space, and estimated the *in vitro* thickness of this endothelial surface layer to be ~350nm. The two calculation methods we applied yield similar values of glycocalyx thickness, commensurate with reported *in vivo* observation.

6.3. Flow-induced Dynamics of the glycocalyx

Using single particle tracking method previously developed, we have successfully located glycocalyx-attached quantum dots with nm spatial resolution and thus have monitored continuously flow-induced layer deformation over minutes. Our data have shown the shear modulus of endothelial surface layer to be ~ 6.7Pa, suggesting a significantly softer gel-nature compared to the endothelial cell itself. Increased level of shear stress results in extended layer deformation that plateaus at high shear stress due to the physical limits that eventually confines the layer extension.

6.4. Future Work

The methods developed in this thesis provide a framework to study a variety of biochemical and mechanical properties of micro-scale or nano-scale biomaterials, such as the delicate endothelial glycocalyx. Future studies may include:

1. long-term impact of flow application on the glycocalyx composition and structure;
2. flow-induced glycocalyx deformation in z-axis, which indicates the change in layer thickness after compression by shear stress;
3. the differences of the glycocalyx expression in laminar region *versus* disturbed flow region;
4. single molecular trafficking and signalling processes that requires detection techniques with a capability of ultra-spatial and high-temperal resolution, and etc.

References

1. **Ainslie KM, Garanich JS, Dull RO, and Tarbell JM.** Vascular smooth muscle cell glycocalyx influences shear stress-mediated contractile response. *J Appl Physiol* 98: 242-249, 2005.
2. **Akerman ME, Chan WC, Laakkonen P, Bhatia SN, and Ruoslahti E.** Nanocrystal targeting in vivo. *Proc Natl Acad Sci U S A* 99: 12617-12621, 2002.
3. **Alivisatos AP, Gu W, and Larabell C.** Quantum dots as cellular probes. *Annu Rev Biomed Eng* 7: 55-76, 2005.
4. **Ando J, Tsuboi H, Korenaga R, Takahashi K, Kosaki K, Isshiki M, Tojo T, Takada Y, and Kamiya A.** Differential display and cloning of shear stress-responsive messenger RNAs in human endothelial cells. *Biochem Biophys Res Commun* 225: 347-351, 1996.
5. **Andres JL, DeFalcis D, Noda M, and Massague J.** Binding of two growth factor families to separate domains of the proteoglycan betaglycan. *J Biol Chem* 267: 5927-5930, 1992.
6. **Arisaka T, Mitsumata M, Kawasumi M, Tohjima T, Hirose S, and Yoshida Y.** Effects of shear stress on glycosaminoglycan synthesis in vascular endothelial cells. *Ann N Y Acad Sci* 748: 543-554, 1995.
7. **Aslam M DA.** *Bioconjugation: Protein Coupling Techniques for the Biomedical Sciences*. London: Macmillan Ref., 1998.
8. **Baldwin AL and Winlove CP.** Effects of perfusate composition on binding of ruthenium red and gold colloid to glycocalyx of rabbit aortic endothelium. *J Histochem Cytochem* 32: 259-266, 1984.
9. **Barak LS and Webb WW.** Fluorescent low density lipoprotein for observation of dynamics of individual receptor complexes on cultured human fibroblasts. *J Cell Biol* 90: 595-604, 1981.
10. **Barbee K, Davies P, and Lal R.** Shear stress-induced reorganization of the surface topography of living endothelial cells imaged by atomic force microscopy. *Circ Res* 74: 163-171, 1994.
11. **Barbee KA, Davies PF, and Lal R.** Shear stress-induced reorganization of the surface topography of living endothelial cells imaged by atomic force microscopy. *Circ Res* 74: 163-171, 1994.
12. **Barbee KA, Mundel T, Lal R, and Davies PF.** Subcellular distribution of shear stress at the surface of flow-aligned and nonaligned endothelial monolayers. *Am J Physiol* 268: H1765-1772, 1995.
13. **Bashkin P, Razin E, Eldor A, and Vlodavsky I.** Degranulating mast cells secrete an endoglycosidase that degrades heparan sulfate in subendothelial extracellular matrix. *Blood* 75: 2204-2212, 1990.
14. **Bass MD and Humphries MJ.** Cytoplasmic interactions of syndecan-4 orchestrate adhesion receptor and growth factor receptor signalling. *Biochem J* 368: 1-15, 2002.
15. **Benedict CR, Pakala R, and Willerson JT.** Endothelial-dependent procoagulant and anticoagulant mechanisms. Recent advances in understanding. *Tex Heart Inst J* 21: 86-90, 1994.

16. **Berry D, Kwan CP, Shriver Z, Venkataraman G, and Sasisekharan R.** Distinct heparan sulfate glycosaminoglycans are responsible for mediating fibroblast growth factor-2 biological activity through different fibroblast growth factor receptors. *Faseb J* 15: 1422-1424, 2001.
17. **Berry D, Shriver Z, Natke B, Kwan CP, Venkataraman G, and Sasisekharan R.** Heparan sulphate glycosaminoglycans derived from endothelial cells and smooth muscle cells differentially modulate fibroblast growth factor-2 biological activity through fibroblast growth factor receptor-1. *Biochem J* 373: 241-249, 2003.
18. **Bikfalvi A, Klein S, Pintucci G, and Rifkin DB.** Biological roles of fibroblast growth factor-2. *Endocr Rev* 18: 26-45, 1997.
19. **Braunwald E.** Shattuck lecture--cardiovascular medicine at the turn of the millennium: triumphs, concerns, and opportunities. *N Engl J Med* 337: 1360-1369, 1997.
20. **Breslow JL.** Cardiovascular disease burden increases, NIH funding decreases. *Nat Med* 3: 600-601, 1997.
21. **Brokmann X, Ehrensperger M, Hermier J, Triller A, and Dahan M.** Orientational imaging and tracking of single CdSe nanocrystals by defocused microscopy. *Chemical Physics Letters* 406: 210-214, 2005.
22. **Brouland JP, Gilbert MA, Bonneau M, Pignaud G, Bal Dit Solier C, and Drouet L.** Macro and microheterogeneity in normal endothelial cells: differential composition of luminal glycocalyx and functional implications. *Endothelium* 6: 251-262, 1999.
23. **Bruchez M, Jr., Moronne M, Gin P, Weiss S, and Alivisatos AP.** Semiconductor nanocrystals as fluorescent biological labels. *Science* 281: 2013-2016, 1998.
24. **Caro C, Fitz-Gerald J, and Schroter R.** Atheroma and arterial wall shear. Observation, correlation and proposal of shear-dependent mass transfer mechanism for atherogenesis. *Proc R Soc Lond B Biol Sci* 117: 109-159, 1971.
25. **Chambers R ZB.** Imtercellular cement and capillary permeability. *Physiol Rev* 27: 436-463, 1947.
26. **Chambers R, Zweifach, BW.** Intercellular cement and capillary permeability. *Physiol Rev* 27: 436-463, 1947.
27. **Chan WC and Nie S.** Quantum dot bioconjugates for ultrasensitive nonisotopic detection. *Science* 281: 2016-2018, 1998.
28. **Chan WCW MD, Gao X, Bailey RE, Han M, Nie S.** Luminescent quantum dots for multiplexed biological detection and imaging. *Curr Opin Biotechnool* 13: 40-46, 2002.
29. **Clough G.** Relationship between microvascular permeability and ultrastructure. *Prog Biophys Mol Biol* 55: 47-69, 1991.
30. **Clough G and Michel CC.** The ultrastructure of frog microvessels following perfusion with the ionophore A23187. *Q J Exp Physiol* 73: 123-125, 1988.
31. **Copley AL.** The endo-endothelial fibrin lining. A historical account. *Thromb Res Suppl* 5: 1-26, 1983.
32. **Copley AL.** Hemorheological aspects of the endothelium-plasma interface. *Microvasc Res* 8: 192-212, 1974.

33. **Copley AL.** The physiological significance of the endoendothelial fibrin lining (EEFL) as the critical interface in the 'vessel-blood organ' and the importance of in vivo 'fibrinogenin formation' in health and disease. *Thromb Res Suppl* 5: 105-145, 1983.
34. **Cornhill JF and Roach MR.** A quantitative study of the localization of atherosclerotic lesions in the rabbit aorta. *Atherosclerosis* 23: 489-501, 1976.
35. **Cunningham KS and Gotlieb AI.** The role of shear stress in the pathogenesis of atherosclerosis. *Lab Invest* 85: 9-23, 2005.
36. **Curry FR.** Microvascular solute and water transport. *Microcirculation* 12: 17-31, 2005.
37. **Dahan M, Levi S, Luccardini C, Rostaing P, Riveau B, and Triller A.** Diffusion dynamics of glycine receptors revealed by single-quantum dot tracking. *Science* 302: 442-445, 2003.
38. **Dall L, Barnes WG, Lane JW, and Mills J.** Enzymatic modification of glycocalyx in the treatment of experimental endocarditis due to viridans streptococci. *J Infect Dis* 156: 736-740, 1987.
39. **Damiano ER.** The effect of the endothelial-cell glycocalyx on the motion of red blood cells through capillaries. *Microvasc Res* 55: 77-91, 1998.
40. **Damiano ER, Duling BR, Ley K, and Skalak TC.** Axisymmetric pressure-driven flow of rigid pellets through a cylindrical tube lined with a deformable porous wall layer. *J Fluid Mech* 314: 163-189, 1996.
41. **Damiano ER and Stace TM.** A mechano-electrochemical model of radial deformation of the capillary glycocalyx. *Biophys J* 82: 1153-1175, 2002.
42. **Davies P.** Flow-mediated endothelial mechanotransduction. *Physiol Rev* 75: 519-560, 1995.
43. **Davies P, Remuzzi A, Gordon EJ, Dewey CF, Jr., and Gimbrone MA, Jr.** Turbulent fluid shear stress induces vascular endothelial cell turnover in vitro. *Proc Natl Acad Sci USA* 83: 2114-2117, 1986.
44. **Davies PF, Dewey CF, Jr., Bussolari SR, Gordon EJ, and Gimbrone MA, Jr.** Influence of hemodynamic forces on vascular endothelial function. In vitro studies of shear stress and pinocytosis in bovine aortic cells. *J Clin Invest* 73: 1121-1129, 1984.
45. **Davies PF, Remuzzi A, Gordon EJ, Dewey CF, Jr., and Gimbrone MA, Jr.** Turbulent fluid shear stress induces vascular endothelial cell turnover in vitro. *Proc Natl Acad Sci U S A* 83: 2114-2117, 1986.
46. **Davies PF, Remuzzi A, Gordon EJ, Dewey CF, Jr., and Gimbrone MA, Jr.** Turbulent fluid shear stress induces vascular endothelial turnover *in vitro*. *Proc Natl Acad Sci, USA* 83: 2114-2117, 1986.
47. **DePaola N, Gimbrone MA, Jr., Davies PF, and Dewey CF, Jr.** Vascular endothelium responds to fluid shear stress gradients. *Arterioscler Thromb* 12: 1254-1257, 1992.
48. **Dewey CF, Jr.** Effects of fluid flow on living vascular cells. *J Biomech Eng* 106: 31-35, 1984.
49. **Dewey CF, Jr., Bussolari SR, Gimbrone MA, Jr. , and Davies PF.** The dynamic response of vascular endothelial cells to fluid shear stress. *J Biomech Eng* 103: 177-185, 1981.

50. **Dubertret B, Skourides P, Norris DJ, Noireaux V, Brivanlou AH, and Libchaber A.** In vivo imaging of quantum dots encapsulated in phospholipid micelles. *Science* 298: 1759-1762, 2002.
51. **Dull RO, Dinavahi R, Schwartz L, Humphries DE, Berry D, Sasisekharan R, and Garcia JG.** Lung endothelial heparan sulfates mediate cationic peptide-induced barrier dysfunction: a new role for the glycocalyx. *Am J Physiol Lung Cell Mol Physiol* 285: L986-995, 2003.
52. **Dulles R and Davies P.** Flow modulation of agonist (ATP)-response (Ca2+) coupling in vascular endothelial cells. *Am J Physiol* 261: H149-H154, 1991.
53. **Dupuis DE, Guilford WH, Wu J, and Warshaw DM.** Actin filament mechanics in the laser trap. *J Muscle Res Cell Motil* 18: 17-30, 1997.
54. **Fisher AB, Chien S, Barakat AI, and Nerem RM.** Endothelial cellular response to altered shear stress. *Am J Physiol Lung Cell Mol Physiol* 281: L529-533, 2001.
55. **Florian JA, Kosky JR, Ainslie K, Pang Z, Dull RO, and Tarbell JM.** Heparan sulfate proteoglycan is a mechanosensor on endothelial cells. *Circ Res* 93: e136-142, 2003.
56. **Gamse G, Fromme HG, and Kresse H.** Metabolism of sulfated glycosaminoglycans in cultured endothelial cells and smooth muscle cells from bovine aorta. *Biochim Biophys Acta* 544: 514-528, 1978.
57. **Gerion D PF, Williams SC, Parak WJ, Zanchet D, et al.** Synthesis and properties of biocompatible water-soluble silica-coated CdSe/ZnS semiconductor quantum dots. *J Phys Chem B* 105: 8861-8871, 2001.
58. **Ghosh RN and Webb WW.** Automated detection and tracking of individual and clustered cell surface low density lipoprotein receptor molecules. *Biophys J* 66: 1301-1318, 1994.
59. **Gibson SF and Lanni F.** Diffraction by a circular aperture as a model for three-dimensional optical microscopy. *J Opt Soc Am A* 6: 1357-1367, 1989.
60. **Gimbrone MA, Jr.** Endothelial dysfunction, hemodynamic forces, and atherosclerosis. *Thromb Haemost* 82: 722-726, 1999.
61. **Gimbrone MA, Jr., Topper JN, Nagel T, Anderson KR, and Garcia-Cardena G.** Endothelial dysfunction, hemodynamic forces, and atherogenesis. *Ann N Y Acad Sci* 902: 230-239, 2000.
62. **Gittes F, Michey B, Nettleton J, and Howard J.** Flexural rigidity of microtubules and actin filaments measured from thermal fluctuations in shape. *J Cell Biol* 120: 923-934, 1993.
63. **Glagov S, Zarins C, Giddens DP, and Ku DN.** Hemodynamics and atherosclerosis. Insights and perspectives gained from studies of human arteries. *Arch Pathol Lab Med* 112: 1018-1031, 1988.
64. **Gouverneur M, Spaan JA, Pannekoek H, Fontijn RD, and Vink H.** Fluid shear stress stimulates incorporation of hyaluronan into endothelial cell glycocalyx. *Am J Physiol Heart Circ Physiol* 290: H458-452, 2006.
65. **Gretz JE and Duling BR.** Measurement uncertainties associated with the use of bright-field and fluorescence microscopy in the microcirculation. *Microvasc Res* 49: 134-140, 1995.

66. **Haldenby KA, Chappell DC, Winlove CP, Parker KH, and Firth JA.** Focal and regional variations in the composition of the glycocalyx of large vessel endothelium. *J Vasc Res* 31: 2-9, 1994.
67. **Han Y, Weinbaum S, Spaan JAE, and Vink H.** Large-deformation analysis of the elastic recoil of fiber layers in a Brinkman medium with application to the endothelial glycocalyx. *J Fluid Mech* 554: 217-235, 2006.
68. **Helmke BP, Thakker DB, Goldman RD, and Davies PF.** Spatiotemporal analysis of flow-induced intermediate filament displacement in living endothelial cells. *Biophys J* 80: 184-194, 2001.
69. **Henry CB and Duling BR.** Permeation of the luminal capillary glycocalyx is determined by hyaluronan. *Am J Physiol* 277: H508-514, 1999.
70. **Hines MA G-SP.** Synthesis and characterization of strongly luminescing ZnS-capped CdSe nanocrystals. *J Phys Chem* 100: 468-471, 1996.
71. **Hohng S HT.** Near-complete suppression of quantum dot blinking in ambient conditions. *J Am Chem Soc* 126: 1324-1325, 2004.
72. **Hu X and Weinbaum S.** A new view of Starling's hypothesis at the microstructural level. *Microvasc Res* 58: 281-304, 1999.
73. **Jaiswal JK, Mattoussi H, Mauro JM, and Simon SM.** Long-term multiple color imaging of live cells using quantum dot bioconjugates. *Nat Biotechnol* 21: 47-51, 2003.
74. **Kamm RD.** Cellular fluid mechanics. *Annu Rev Fluid Mech* 34: 211-232, 2002.
75. **Khachigian LM, Anderson KR, Halnon NJ, Gimbrone MA, Jr., Resnick N, and Collins T.** Egr-1 is activated in endothelial cells exposed to fluid shear stress and interacts with a novel shear-stress-response element in the PDGF A-chain promoter. *Arterioscler Thromb Vasc Biol* 17: 2280-2286, 1997.
76. **Kishino A and Yanagida T.** Force measurements by micromanipulation of a single actin filament by glass needles. *Nature* 334: 74-76, 1988.
77. **Klitzman B and Duling BR.** Microvascular hematocrit and red cell flow in resting and contracting striated muscle. *Am J Physiol* 237: H481-490, 1979.
78. **Kloepfer JA MR, Wong MS, Nealson KH, Stucky G, Nadeau JL.** Quantum dots as strain- and metabolism-specific microbiological labels. *Appl Environ Microbiol* 69: 4205-4213, 2003.
79. **Lakowicz JR, Gryczynski I, Gryczynski Z, Nowaczyk K, and Murphy CJ.** Time-resolved spectral observations of cadmium-enriched cadmium sulfide nanoparticles and the effects of DNA oligomer binding. *Anal Biochem* 280: 128-136, 2000.
80. **Laskov R, Michaeli RI, Sharir H, Yefenof E, and Vlodavsky I.** Production of heparanase by normal and neoplastic murine B-lymphocytes. *Int J Cancer* 47: 92-98, 1991.
81. **Levesque MJ, Nerem RM, and Sprague EA.** Vascular endothelial cell proliferation in culture and the influence of flow. *Biomaterials* 11: 702-707, 1990.
82. **Ley K.** Molecular mechanisms of leukocyte recruitment in the inflammatory process. *Cardiovasc Res* 32: 733-742, 1996.
83. **Lijnen HR and Collen D.** Endothelium in hemostasis and thrombosis. *Prog Cardiovasc Dis* 39: 343-350, 1997.
84. **Luckhoff A and Clapham DE.** Inositol 1,3,4,5-tetrakisphosphate activates an endothelial Ca(2+)-permeable channel. *Nature* 355: 356-358, 1992.

85. **Luft JH.** Fine structures of capillary and endocapillary layer as revealed by ruthenium red. *Fed Proc* 25: 1773-1783, 1966.
86. **Luo R, Yang, XY., Peng, XF., Sun, YF.** Three-dimensional tracking of fluorescent particles applied to micro-fluidic measurements. *J Micromech Microeng* 16: 1689-1699, 2006.
87. **Mahtab R HH, Murphy CJ.** Temperature- and salt-dependent binding of long DNA to protein-sized quantum dots: thermodynamics of "inorganic protein"-DNA interactions. *JAmChemSoc* 122: 14-17, 2000.
88. **Malek AM and Izumo S.** Mechanism of endothelial cell shape change and cytoskeletal remodeling in response to fluid shear stress. *J Cell Sci* 109 (Pt 4): 713-726, 1996.
89. **Marcum JA and Rosenberg RD.** Anticoagulantly active heparan sulfate proteoglycan and the vascular endothelium. *Semin Thromb Hemost* 13: 464-474, 1987.
90. **Matzner Y, Bar-Ner M, Yahalom J, Ishai-Michaeli R, Fuks Z, and Vlodavsky I.** Degradation of heparan sulfate in the subendothelial extracellular matrix by a readily released heparanase from human neutrophils. Possible role in invasion through basement membranes. *J Clin Invest* 76: 1306-1313, 1985.
91. **Mertens G, Cassiman JJ, Van den Berghe H, Vermylen J, and David G.** Cell surface heparan sulfate proteoglycans from human vascular endothelial cells. Core protein characterization and antithrombin III binding properties. *J Biol Chem* 267: 20435-20443, 1992.
92. **Michalet X PF, Lacoste TD, Dahan M, Bruchez M, et al.** Properties of fluorescent semiconductor nanocrystals and their applications to biological labeling. *Single Mol* 2: 260-276, 2001.
93. **Mochizuki S, Vink H, Hiramatsu O, Kajita T, Shigeto F, Spaan JA, and Kajiya F.** Role of hyaluronic acid glycosaminoglycans in shear-induced endothelium-derived nitric oxide release. *Am J Physiol Heart Circ Physiol* 285: H722-726, 2003.
94. **Mofrad MRK and Kamm RD.** *Cytoskeletal Mechanics*: Cambridge University Press, 2006.
95. **Moon JJ, Matsumoto M, Patel S, Lee L, Guan JL, and Li S.** Role of cell surface heparan sulfate proteoglycans in endothelial cell migration and mechanotransduction. *J Cell Physiol* 203: 166-176, 2005.
96. **Murray CB ND, Bawendi MG.** Synthesis and characterization of nearly monodisperse CdE(E=S, Se, Te)semiconductor nanocrystallities. *J Am Chem Soc* 115: 8706-8715, 1993.
97. **Nan X, Sims PA, Chen P, and Xie XS.** Observation of individual microtubule motor steps in living cells with endocytosed quantum dots. *J Phys Chem B* 109: 24220-24224, 2005.
98. **Nerem RM, Levesque MJ, and Cornhill JF.** Vascular endothelial morphology as an indicator of the pattern of blood flow. *J Biomech Eng* 103: 172-176, 1981.
99. **Ohashi T, Ishii Y, Ishikawa Y, Matsumoto T, and Sato M.** Experimental and numerical analyses of local mechanical properties measured by atomic force microscopy for sheared endothelial cells. *Biomed Mater Eng* 12: 319-327, 2002.
100. **Olsen M G ARJ.** Out-of-focus effects on particle image visibility and correlation in microscopic particle image celocimetry. *Exp Gluids (Suppl)* 29: s166-s174, 2000.

101. **Oppenheim A, Wilsky AS.** *Signals and Systems*. Upper Saddle River, NJ: Prentice Hall, 1996.
102. **Osborn EA, Rabodzey A, Dewey CF, Jr., and Hartwig JH.** Endothelial actin cytoskeleton remodeling during mechanostimulation with fluid shear stress. *Am J Physiol Cell Physiol* 290: C444-452, 2006.
103. **Ota T, Sugiura T, and Kawata S.** Rupture force measurement of biotin-streptavidin bonds using optical trapping. *Applied Physics Letters* 87, 2005.
104. **Parak WJ GD, Pellegrino T, Zanchet D, Micheel C, et al.** Biological applications of colloidal nanocrystals. *Nanotechnology* 14: R15-27, 2003.
105. **Park JS, Choi, CK., Kihm K. D.** Temperature measurement for a nanoparticle suspension by detecting Brownian motion using optical serial sectioning microscopy (OSSM). *Meas Sci Technol* 16: 1418-1429, 2005.
106. **Pathak S CS, Arnheim N, Thompson ME.** Hydroxylated quantum dots as luminescent probes for in situ hybridization. *J Am Chem Soc* 123: 4103-4104, 2001.
107. **Peng XG SM, Kadavanich AV, Alivisatos AP.** Epitaxial growth of highly luminescent CdSe/CdS core/shell nanocrystals with photostability and electronic accessibility. *J Am Chem Soc* 119: 7019-7029, 1997.
108. **Pinaud F, King D, Moore HP, and Weiss S.** Bioactivation and cell targeting of semiconductor CdSe/ZnS nanocrystals with phytochelatin-related peptides. *J Am Chem Soc* 126: 6115-6123, 2004.
109. **Pries AR, Secomb TW, and Gaehtgens P.** The endothelial surface layer. *Pflugers Arch* 440: 653-666, 2000.
110. **Pries AR, Secomb TW, Gaehtgens P, and Gross JF.** Blood flow in microvascular networks. Experiments and simulation. *Circ Res* 67: 826-834, 1990.
111. **Pries AR, Secomb TW, Gessner T, Sperandio MB, Gross JF, and Gaehtgens P.** Resistance to blood flow in microvessels in vivo. *Circ Res* 75: 904-915, 1994.
112. **Pries AR, Secomb TW, Jacobs H, Sperandio M, Osterloh K, and Gaehtgens P.** Microvascular blood flow resistance: role of endothelial surface layer. *Am J Physiol* 273: H2272-2279, 1997.
113. **Rabodzey A, Yao Y, Luscinskas WF, Shaw S, and Dewey Jr C.** Endothelial cells early response to flow may be mediated by VE-cadherins. *In Review*, 2006.
114. **Remuzzi A, Dewey CJ, Davies P, and Gimbrone MJ.** Orientation of endothelial cells in shear fields *in vitro*. *Biorheology* 21: 617-630, 1984.
115. **Resnick N and Gimbrone MA, Jr.** Hemodynamic forces are complex regulators of endothelial gene expression. *Faseb J* 9: 874-882, 1995.
116. **Resnick N, Yahav H, Khachigian LM, Collins T, Anderson KR, Dewey FC, and Gimbrone MA, Jr.** Endothelial gene regulation by laminar shear stress. *Adv Exp Med Biol* 430: 155-164, 1997.
117. **Rosenberg RD, Shworak NW, Liu J, Schwartz JJ, and Zhang L.** Heparan sulfate proteoglycans of the cardiovascular system. Specific structures emerge but how is synthesis regulated? *J Clin Invest* 100: S67-75, 1997.
118. **Ross R.** Atherosclerosis--an inflammatory disease. *N Engl J Med* 340: 115-126, 1999.
119. **Ross R.** Atherosclerosis is an inflammatory disease. *Am Heart J* 138: S419-420, 1999.
120. **Ross R.** Cell biology of atherosclerosis. *Annu Rev Physiol* 57: 791-804, 1995.

121. **Ross R.** The pathogenesis of atherosclerosis- an update. *New Engl J Med* 314: 488-499, 1986.
122. **Ross R and Glomset J.** The pathogenesis of atherosclerosis. *New Engl J Med* 295: 369-377, 1976.
123. **Rostgaard J and Qvortrup K.** Electron microscopic demonstrations of filamentous molecular sieve plugs in capillary fenestrae. *Microvasc Res* 53: 1-13, 1997.
124. **Satcher R, Bussolari S, Gimbrone MJ, and Dewey CJ.** The distribution of fluid forces on model arterial endothelium using computational fluid dynamics. *J Biomech Eng* 114: 309-316, 1992.
125. **Satcher R, Dewey Jr CF, and Hartwig J.** Mechanical remodeling of the endothelial surface and actin cytoskeleton induced by fluid flow. *Microcirculation* 4: 439-453, 1997.
126. **Satcher RL, Jr. and Dewey CF, Jr.** Theoretical estimates of mechanical properties of the endothelial cell cytoskeleton [see comments]. *Biophys J* 71: 109-118, 1996.
127. **Sato M, Nagayama K, Kataoka N, Sasaki M, and Hane K.** Local mechanical properties measured by atomic force microscopy for cultured bovine endothelial cells exposed to shear stress. *J Biomech* 33: 127-135, 2000.
128. **Sato M, Theret D, Wheeler L, Ohshima N, and Nerem R.** Application of the micropipette technique to the measurement of cultured procine aortic endothelial cell viscoelastic properties. *J Biomech Eng* 112: 263-268, 1990.
129. **Schnapp BJ, Gelles J, and Sheetz MP.** Nanometer-scale measurements using video light microscopy. *Cell Motil Cytoskeleton* 10: 47-53, 1988.
130. **Schnitzer JE, Shen CP, and Palade GE.** Lectin analysis of common glycoproteins detected on the surface of continuous microvascular endothelium in situ and in culture: identification of sialoglycoproteins. *Eur J Cell Biol* 52: 241-251, 1990.
131. **Secomb TW, Hsu R, and Pries AR.** Effect of the endothelial surface layer on transmission of fluid shear stress to endothelial cells. *Biorheology* 38: 143-150, 2001.
132. **Secomb TW, Hsu R, and Pries AR.** A model for red blood cell motion in glycocalyx-lined capillaries. *Am J Physiol* 274: H1016-1022, 1998.
133. **Shen J, Luscinskas F, Dewey CJ, and Gimbrone MJ.** Fluid shear stress modulates cytosolic free calcium in vascular endothelial cells. *Am J Physiol* 262: C384-C390, 1992.
134. **Shen J, Luscinskas FW, Connolly A, Dewey CF, Jr., and Gimbrone MA, Jr.** Fluid shear stress modulates cytosolic free calcium in vascular endothelial cells. *Am J Physiol* 262: C384-390, 1992.
135. **Shyy JY, Lin MC, Han J, Lu Y, Petrime M, and Chien S.** The cis-acting phorbol ester "12-O-tetradecanoylphorbol 13-acetate"-responsive element is involved in shear stress-induced monocyte chemotactic protein 1 gene expression. *Proc Natl Acad Sci U S A* 92: 8069-8073, 1995.
136. **Simons M and Horowitz A.** Syndecan-4-mediated signalling. *Cell Signal* 13: 855-862, 2001.
137. **Sims DE, Westfall JA, Kiorpes AL, and Horne MM.** Preservation of tracheal mucus by nonaqueous fixative. *Biotech Histochem* 66: 173-180, 1991.

138. **Skinner MP, Lucas CM, Burns GF, Chesterman CN, and Berndt MC.** GMP-140 binding to neutrophils is inhibited by sulfated glycans. *J Biol Chem* 266: 5371-5374, 1991.
139. **Smith PR, Morrison IE, Wilson KM, Fernandez N, and Cherry RJ.** Anomalous diffusion of major histocompatibility complex class I molecules on HeLa cells determined by single particle tracking. *Biophys J* 76: 3331-3344, 1999.
140. **Speidel M, Jonas A, and Florin EL.** Three-dimensional tracking of fluorescent nanoparticles with subnanometer precision by use of off-focus imaging. *Opt Lett* 28: 69-71, 2003.
141. **Springer TA.** Traffic signals on endothelium for lymphocyte recirculation and leukocyte emigration. *Annu Rev Physiol* 57: 827-872, 1995.
142. **Squire JM, Chew M, Nneji G, Neal C, Barry J, and Michel C.** Quasi-periodic substructure in the microvessel endothelial glycocalyx: a possible explanation for molecular filtering? *J Struct Biol* 136: 239-255, 2001.
143. **Stace TM and Damiano ER.** An electrochemical model of the transport of charged molecules through the capillary glycocalyx. *Biophys J* 80: 1670-1690, 2001.
144. **Sun B XW, Yi G, Chen D, Zhou Y, Cheng J. .** Microminiaturized immunoassays using quantum dots as fluorescent label by laser confocal scanning fluorescence detection. *J Immunol Method* 249: 85-89, 2001.
145. **Takahashi M and Berk BC.** Mitogen-activated protein kinase (ERK1/2) activation by shear stress and adhesion in endothelial cells. Essential role for a herbimycin-sensitive kinase. *J Clin Invest* 98: 2623-2631, 1996.
146. **Tarbell JM and Pahakis MY.** Mechanotransduction and the glycocalyx. *J Intern Med* 259: 339-350, 2006.
147. **Tarbell JM, Weinbaum S, and Kamm RD.** Cellular fluid mechanics and mechanotransduction. *Ann Biomed Eng* 33: 1719-1723, 2005.
148. **Theret DP, Levesque MJ, Sato M, Nerem RM, and Wheeler LT.** The application of a homogeneous half-space model in the analysis of endothelial cell micropipette measurements. *J Biomech Eng* 110: 190-199, 1988.
149. **Thi MM, Tarbell JM, Weinbaum S, and Spray DC.** The role of the glycocalyx in reorganization of the actin cytoskeleton under fluid shear stress: a "bumper-car" model. *Proc Natl Acad Sci U S A* 101: 16483-16488, 2004.
150. **Thompson RE, Larson DR, and Webb WW.** Precise nanometer localization analysis for individual fluorescent probes. *Biophys J* 82: 2775-2783, 2002.
151. **Tkachenko E, Rhodes JM, and Simons M.** Syndecans: new kids on the signaling block. *Circ Res* 96: 488-500, 2005.
152. **Ueda A, Shimomura M, Ikeda M, Yamaguchi R, and Tanishita K.** Effect of glycocalyx on shear-dependent albumin uptake in endothelial cells. *Am J Physiol Heart Circ Physiol* 287: H2287-2294, 2004.
153. **van den Berg BM, Spaan JA, Rolf TM, and Vink H.** Atherogenic region and diet diminish glycocalyx dimension and increase intima-to-media ratios at murine carotid artery bifurcation. *Am J Physiol Heart Circ Physiol* 290: H915-920, 2006.
154. **van den Berg BM, Vink H, and Spaan JA.** The endothelial glycocalyx protects against myocardial edema. *Circ Res* 92: 592-594, 2003.

155. **van Haaren PM, VanBavel E, Vink H, and Spaan JA.** Localization of the permeability barrier to solutes in isolated arteries by confocal microscopy. *Am J Physiol Heart Circ Physiol* 285: H2848-2856, 2003.
156. **Vink H and Duling BR.** Capillary endothelial surface layer selectively reduces plasma solute distribution volume. *Am J Physiol Heart Circ Physiol* 278: H285-289, 2000.
157. **Vink H and Duling BR.** Identification of distinct luminal domains for macromolecules, erythrocytes, and leukocytes within mammalian capillaries. *Circ Res* 79: 581-589, 1996.
158. **Vink H, Spaan JAE, and Duling BR.** Mechanical properties of the endothelial surface layer. *FASEB J* 13, 1999.
159. **Watt I.** *The principles and practice of electron miroscopy*: Cambridge University Press, 2003.
160. **Webb WW, Barak LS, Tank DW, and Wu ES.** Molecular mobility on the cell surface. *Biochem Soc Symp*: 191-205, 1981.
161. **Weinbaum S, Tarbell JM, and Damiano ER.** The Structure and Function of the Endothelial Glycocalyx Layer. *Annu Rev Biomed Eng*, 2007.
162. **Weinbaum S, Zhang X, Han Y, Vink H, and Cowin SC.** Mechanotransduction and flow across the endothelial glycocalyx. *Proc Natl Acad Sci U S A* 100: 7988-7995, 2003.
163. **Wu M, Roberts, KW., Buckley, M.** Three-dimensional fluorescent particle tracking at micron-scale using a single camera. *Experiments in Fluids* 38: 461-465, 2005.
164. **Wu X, Liu H, Liu J, Haley KN, Treadway JA, Larson JP, Ge N, Peale F, and Bruchez MP.** Immunofluorescent labeling of cancer marker Her2 and other cellular targets with semiconductor quantum dots. *Nat Biotechnol* 21: 41-46, 2003.
165. **Yao Y, Rabodzey A, and Dewey CF.** Glycocalyx modulates the motility and proliferative response of vascular endothelium to fluid shear stress. *Am J Physiol Heart Circ Physiol*, 2007.
166. **Yoneda A and Couchman JR.** Regulation of cytoskeletal organization by syndecan transmembrane proteoglycans. *Matrix Biol* 22: 25-33, 2003.
167. **Zhang X, Adamson RH, Curry FR, and Weinbaum S.** A 1-D model to explore the effects of tissue loading and tissue concentration gradients in the revised Starling principle. *Am J Physiol Heart Circ Physiol* 291: H2950-2964, 2006.
168. **Zhao Y, Chien S, and Weinbaum S.** Dynamic contact forces on leukocyte microvilli and their penetration of the endothelial glycocalyx. *Biophys J* 80: 1124-1140, 2001.